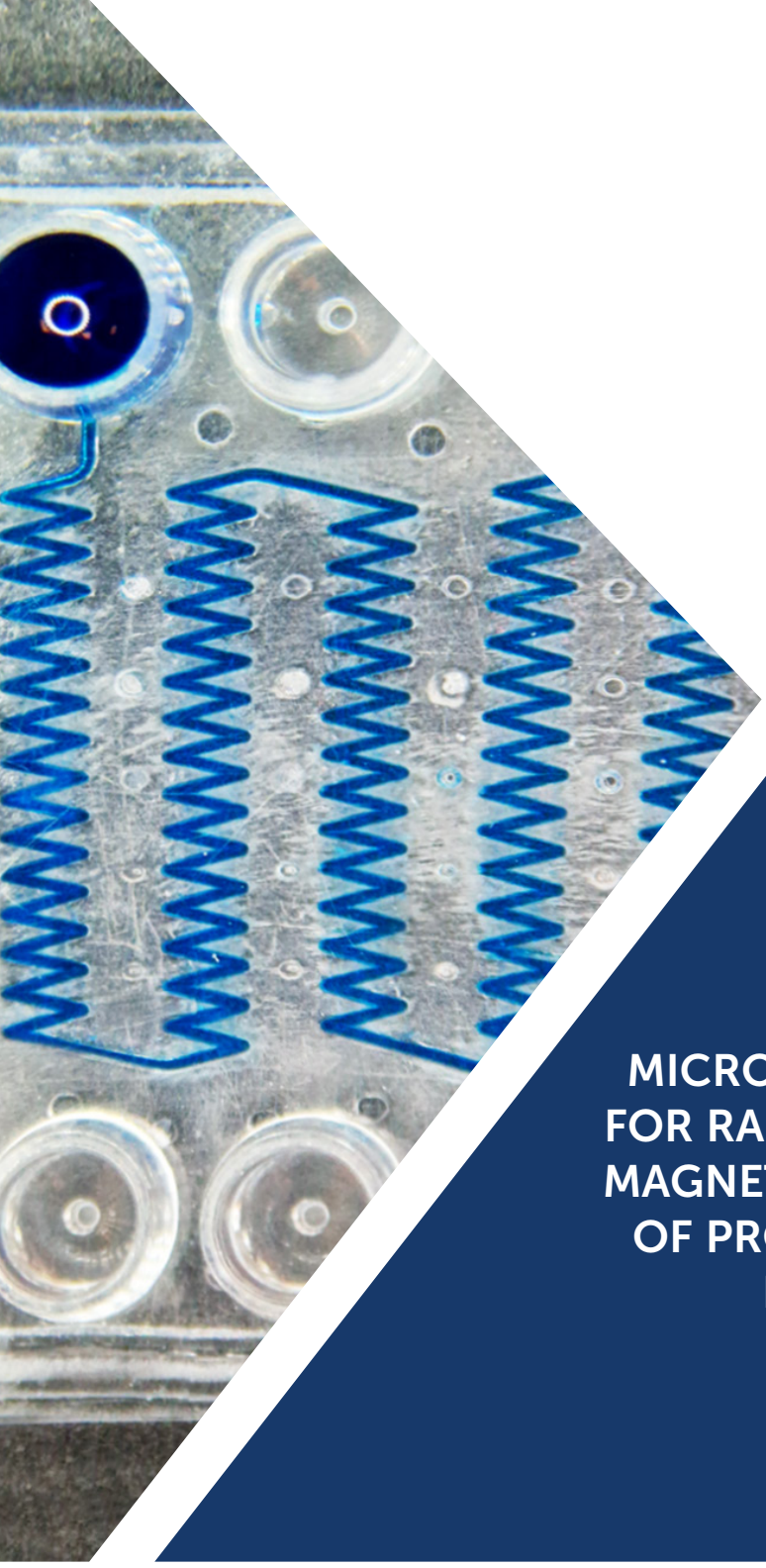

UNIVERSITY OF
LATVIA

Doctoral Thesis

Riga 2025

Janis Cipa

INTEGRATED MICROFLUIDIC DEVICE FOR RAPID MIXING AND MAGNETIC SEPARATION OF PROSTATE CANCER EXTRACELLULAR VESICLES

UNIVERSITY OF
LATVIA

FACULTY OF SCIENCE AND TECHNOLOGY

Janis Cipa

INTEGRATED MICROFLUIDIC DEVICE FOR RAPID MIXING AND MAGNETIC SEPARATION OF PROSTATE CANCER EXTRACELLULAR VESICLES

DOCTORAL THESIS

Submitted for the degree of Doctor of Engineering and Technology
Field of Materials Science
Subfield of Materials Physics

RIGA 2025

The doctoral thesis was carried out at the Institute of solid state physics, University of Latvia, from year 2021 to 2025.

The creation of this thesis was supported by Camart2 project No 1.1.1.4/17/I/002, European Regional Development Fund (ERDF), No 1.1.1.1/20/A/045 and Latvian Council of Science project VPP-EM-FOTONIKA-2022/1-0001.

Dissertation in the field of materials science, subfield of materials physics.

Supervisor: Dr. *phys*. **Roberts Rimsa**, Institute of Solid State Physics University of Latvia.

Reviewers:

Aivars Vembris, *Dr. phys.,* lead researcher, Institute of Solid State Phyiscs;
Guntars Kitenbergs, *Dr. phys.,* Associate professor, University of Latvia;
Linas Mazutis, *PhD* in Biological Chemistry, Professor, Vilnius University.

The thesis is available at the Library of the University of Latvia, Raina boulevard 19.

Chairman of the Doctoral Committee *Dr. habil. phys.* Uldis Rogulis
Secretary of the Doctoral Committee Sintija Silina

ISBN 978-9934-36-407-5
ISBN 978-9934-36-408-2 (PDF)

ABSTRACT

Prostate cancer is the second most common cancer in men and the fifth leading cause of cancer-related mortality globally. Its detection is complicated by a high rate of false positives and difficulty differentiating between benign and malignant tumours. These diagnostic challenges are compounded by a substantial increase in mortality if the disease progresses to a metastatic stage. In recent years extracellular vesicles (EVs) have emerged as a promising bio marker for non-invasive disease detection. To improve detection of prostate cancer, a microfluidics device for extracellular vesicle sample preparation was developed consisting of a mixing and magnetic separation module. Using passive zig-zag mixer a mixing index of 0.92 was achieved and validated through optical 2D analysis. Furthermore, the 3D mixing mechanism was investigated using confocal microscopy where complex local vortex formation was observed. Magnetic particle separation efficiency exceeded 98 % following the optimization of magnetic arrangements. The most effective setup utilized an array of N45 magnets configured in a North-South alignment. After integrating both modules on a microfluidics chip, the binding kinetics between EVs and anti-CD9 nanobodies were measured. Based on the binding kinetics, after 10 min the EV capture was saturated and comparable to standard laboratory assays, offering a faster alternative to antibody-based immunomagnetic protocols. Furthermore, this thesis reveals the binding kinetics of EVs to anti-CD9 nanobodies for the first time. This thesis demonstrates the potential of the microfluidic device to enhance clinical diagnostics by offering speed and reducing manual labour without compromising accuracy.

Statements to Defend

1. Off-stoichiometry thiol-ene polymer (OSTE), combined with cyclic olefin copolymer (COC), enables the fabrication of extracellular vesicle sample preparation devices using photolithography and without a thermal cure step.
2. Three-dimensional confocal microscopy of passive microfluidic mixers provides direct experimental evidence of Dean vortices and secondary flow structures at the microscale—phenomena previously unresolved by conventional two-dimensional optical microscopy.
3. Magnetic particles can be separated with over 98 % efficiency in a microfluidic device. Extracellular vesicles bound to nanobody-conjugated magnetic particles have asymptotic binding kinetics reaching saturation within 10 minutes in both the microfluidic device and standard method.

ANOTĀCIJA

Prostatas vēzis ir otrais visbiežāk diagnosticētais vēzis vīriešiem, taču tas ieņem piekto vietu ar vēzi saistīto mirstību pasaulē. Prostatas vēža noteikšana ir sarežģīta, jo pastāv augsts viltus pozitīvu rezultātu risks, kā arī ir grūtības atšķirt labdabīgu no ļaundabīga audzēja, kas, vēzim progresējot līdz metastātiskajai stadijai, var novest pie būtiska mirstības pieauguma. Pēdējos gados ārpusšūnu vezikulas (AV) ir kļuvušas par daudzsološu biomarķieri neinvazīvai slimību noteikšanai. Lai uzlabotu prostatas vēža noteikšanu, tika izstrādāta mikrofluidikas ierīce AV paraugu sagatavošanai, kas sastāv no maisīšanas un magnētiskās atdalīšanas moduļa. Izmantojot pasīvo zigzag veida maisītāju, tika iegūts maisīšanās indekss 0,92, kas tika noteikts ar 2D analīzi. 3D sajaukšanas mehānisms tika pētīts, izmantojot konfokālo mikroskopiju, kurā tika novērota sarežģīta lokāla virpuļu veidošanās. Veicot magnētu izkārtojuma optimizāciju, bija iespējams sasniegt magnētisko daļiņu atdalīšanas efektivitāti, kas bija augstāka nekā 98 %. Visefektīvākais izkārtojums bija N45 magnētu masīvs horizontālā Ziemeļu-Dienvidu novietojumā. Pēc moduļu integrācijas mikrofluidikas iekārtā tika mērīta AV un viena domēna anti-CD9 antivielas saistīšanās kinētika. Pamatojoties uz saistīšanās kinētiku, pēc 10 minūtēm saistīšanās sasniedza intensitātes piesātinājumu, kas bija salīdzināms ar standarta laboratorijas metodi, piedāvājot ātrāku alternatīvu citām uz antivielām balstītām saistīšanās metodēm. Turklāt, šajā disertācijā pirmo reizi ir parādīta AV saistīšanās kinētika ar viena domēna anti-CD9 antivielu. Disertācija parāda mikrofluidikas ierīces potenciālu attīstīt klīnisko diagnostiku, uzlabojot detektēšanas ātrumu, samazinot manuālo darbu un nezaudējot precizitāti.

Tēzes

- Ne-stehiometriskā tiola-ēna polimēru (OSTE) var izmantot kopā ar cikliskā olefīna kopolimēru (COC), lai izgatavotu ārpusšūnu vezikulu paraugu sagatavošanas ierīci, izmantojot fotolitogrāfiju, un izslēdzot termiskās cietināšanas posmu.
- Trīsdimensiju konfokālā mikroskopija pasīvajām mikrofluidikas maisīšanas ierīcēm parāda Dīna virpuļu un sekundārā plūsmas veidošanos, sniedzot tiešus eksperimentālus pierādījumus par mikroizmēra plūsmu, kas nav izšķirama tradicionālajā divdimensiju optiskajā mikroskopijā.
- Magnētiskās daļiņas var tikt atdalītas ar vairāk kā 98 % efektivitāti mikrofluidikas ierīcē. Ārpusšūnu vezikulām, kas ir saistītas ar viena domēna anti-CD9 antivielas konjugētām magnētiskajām daļiņām, saistīšanās kinētika ir asimptotiska un sasniedz piesātinājumu 10 minūšu laikā gan mikrofluidikas ierīcēs, gan standarta laboratorijas metodē.

TABLE OF CONTENTS

GLOSSARY

Abbreviations

AF4	Flow field-flow fractionation
ALD	Atomic Layer Deposition
AMI	Absolute mixing index
AR	Aspect ratio
ASR	The age-standardized rate
CAD	Computer-Aided Design
COC	Cyclic Olefin Copolymer
ctDNA	Circulating tumour deoxyribonucleic acid
DIW	Deionized water
DNA	Deoxyribonucleic acid
DPSS	Diode-pumped solid-state laser
DXF	Drawing Exchange Format
EVs	Extracellular vesicles
GDS2	Graphic Design System
HMDS	Hexamethyldisilazane
IPA	Isopropanol
LNCaP	Lymph node carcinoma of the prostate
MP	Magnetic particle
Nb	Nanobodies
OSTE	Off-stoichiometry thiol-ene
PDMS	Polydimethylsiloxane
PMMA	Polymethyl methacrylate
PPV	Positive predictive value
PSA	Prostate specific antigen
PTFE	Polytetrafluoroethylene
QPCR	Real-time polymerase chain reaction
RMI	Relative mixing index
RNA	Ribonucleic acid
STL	Stereolithography
TMA	Trimethylaluminum
UV	Ultraviolet
WB	Western blot (protein immune blot)

Characteristic quantity

χ	Mobility of the particle ($m^2/(Ns)$)
σ	Standard deviation of the pixel intensities
σ_0	Standard deviation of the pixel intensities in the unmixed case
μ_0	Permeability of free space (N/A^2)
$<I>$	Average pixel intensities in the cross section
A	Cross-sectional area (m^2)
B	Magnetic field strength (T)
D	Diameter (m)
De	Dean number
D_H	Hydraulic diameter (m)
F	Force (N)
I_{oi}	Local pixel intensity in the unmixed state
L	Characteristic length (m)
m	Magnetic moment ($m^2 \cdot A$)
M	Molar mass (g/mol)
N	Total number of pixels
P	Perimeter (m)
Q	Volumetric flow rate (m^3/s)
r	Radius (m)
r_C	Curvature radius (m)
r_M	Molecular radius (m)
Re	Reynolds number
t	Time (s)
T	Temperature (K)
u	Characteristic velocity (m/s)
V	Volume (m^3)
W	Mass flowrate (kg/s)
ν	Kinematic viscosity, (m^2/s)
ρ	Density (kg/m^3)
η	Dynamic viscosity ($kg/(m \cdot s)$)
π	Pi

Physical constants

k_b	Boltzmann constant ($Kg*m^2/(s^2*K)$
N_A	Avogadro's number (mol^{-1})

INTRODUCTION

The importance of developing new and improved medical devices cannot be overstated, particularly for diseases like cancer, where early detection is crucial for reducing cancer mortality. However, current detection methods often face limitations related to complexity, cost, accuracy, and practicality, making them less effective for routine use. These challenges are especially evident in the early stages of cancer, where subtle physiological changes make detection difficult with existing methods.

This dissertation addresses these challenges with a focus on prostate cancer. It begins with a literature review of the disease, current detection methods and microfluidics approach to detection. The experimental part addresses the whole device cycle from fabrication to bioreactor grown prostate cancer extracellular vesicles (EVs) that are tested in microfluids device and compared to standard laboratory methods.

The creation of a microfluidic device requires the combination of concepts from engineering, physics, and biology, forming the foundation of microfluidics a field that precisely manipulates small volumes of liquids, starting from picolitres in droplet microfluidics up to microliters for diagnostics and biosensing, to enhance functionality and process efficiency. This is mainly due to the unique physical phenomena that occur at a small scale, such as the increased importance of capillary forces, the predominance of laminar flow, and the drastic increase in surface-to-volume ratio. Additionally, the reduction in required reagent volumes lowers costs, and the simplification of complex biological processes is possible due to the smaller scale and reduced interactions.

EVs are central to this detection method, given that current approaches, such as prostate-specific antigen testing, suffer from high false-negative rates. EVs are small membrane-bound particles released by cells into the bloodstream, carrying various biomarkers that facilitate cell communication. The potential of EVs lies in their ubiquitous release by all cells, with the ability to differentiate between cancerous and normal cells, thereby offering a promising new marker for cancer detection.

By integrating the advantages of microfluidics with the potential of EVs as early cancer markers, this work aims to advance the development of a novel detection device that offers a meaningful improvement over the currently available methods.

Research aim

Further development of microfluidics devices made of thermoplastics and to investigate the microfluidics device applicability for prostate cancer detection via liquid biopsy using extracellular vesicles.

Research objectives

- Develop the fabrication process for a microfluidics device that is superior to PDMS fabrication process in terms of scalability and small molecule absorption.

- Create a quality control procedure for the fabrication process.
- Develop mixing and magnetic separation module as a sample preparation for downstream analysis.
- Quantify the mixing module using 2D and 3D visualization methods, to finding the optimal design.
- Quantify the performance of the magnetic separation module and optimize the design to acquire 95 % + capture efficacy.
- Evaluate the combined system of MP and EVs using bioreactor-grown EVs in microfluidic device and compare it to the standard procedure.

Scientific novelty

The scientific novelty is the progress made in the field of microfluidics for cancer detection, achieved by improving techniques for extracting EVs and integration of multiple microfluidic modules.

- **Fabrication Process**: This thesis introduces the fabrication of an OSTE-COC device using OSTE220, a method that, to the best of the author's knowledge, has not yet been applied in this context. This approach offers advantages over previous methods used in organs-on-chip [1] and EV separation [2] applications.
- **Flow Pattern Visualization**: Detailed 3D confocal images of the flow patterns, which are rarely found in scientific literature. These images contribute to the understanding of fluid dynamics, particularly in the areas of Dean vortices and secondary flow.
- **EV Capture Antibodies**: The EV capture antibodies utilised in this study, which demonstrate specific capture efficacy, are not commercially available, highlighting their scientific relevance.
- **Device Integration and Potential**: The final device shows promise for further development and potential clinical adoption due to its fabrication technique and the ability to integrate multiple modules.
- **Kinetic Profile of EV-MP Binding**: The kinetic profile of EV and magnetic particle (MP) binding using CD9 nanobodies, as characterised in this study, has not been previously reported, providing valuable information for similar systems.

Practical significance

Research in prostate cancer detection is considered to hold considerable potential for reducing mortality rates, as the likelihood of successful treatment is dramatically increased by early detection [3]. Given the relatively recent discovery of EVs as biomarkers secreted by all cell types, the development of EV-based assays is viewed as a pathway for comprehensive testing solutions [4]. Moreover, advancements in microfluidic devices within the diagnostics field could lead to substantial cost reductions and improved convenience, ultimately enhancing healthcare outcomes [5]. This research represents a step in transitioning microfluidic devices from laboratory settings to practical applications, by providing a fabrication protocol for small to medium-scale production, facilitating rapid prototyping and real-world testing. Lastly,

the fundamental insights gained from 3D flow visualisation and kinetic profiling contribute to the broader scientific understanding in this field.

Author's contribution

The author fabricated and characterised the microfluidic device. This involved designing the device, adapting the fabrication process from existing literature, optimising key parameters, and conducting quality control. The development of fabrication protocol for the microfluidic device was supported by Roberts Rimsa, Arnita Spule, Gunita Paidere, and Karlis Grindulis, who contributed through shared insights, tips, and collaborative efforts in similar processes.

The author independently conducted the 2D mixing experiments, while Feliks Rumnieks, who operated the confocal microscope, assisted in the 3D experiments.

The testing of the microfluidic device using biological samples was a collaborative effort with the Latvian biomedical research and study centre, specifically with Edgars Endzelins. The author provided fabricated microfluidics devices, developed flow control sequences, operated the microfluidics system and set up experiments from the microfluidics perspective. The final experimental setups and added controls were developed in cooperation with Edgars Endzelins.

Protein immunoblot (Western blot), qPCR, and iron content measurements were performed by Edgars Endzelins, while the data analysis was conducted by the author, with support from Edgars Endzelins.

List of publications

Publications included in this Thesis

1. J. Cipa et al., "OSTE DEVICE FOR MAGNETIC PARTICLE CAPTURE," MicroTAS 2022 – 26th International Conference on Miniaturized Systems for Chemistry and Life Sciences, pp. 919–920, Jan. 2022.
2. J. Cipa, E. Endzelins, A. Abols, N. Romanchikova, A. Line, G. W. Jenster, G. Mozolevskis, R. Rimsa. "Elucidating Extracellular Vesicle Isolation Kinetics via an Integrated Off-Stoichiometry Thiol-Ene and Cyclic Olefin Copolymer Microfluidic Device". Polymers 2024, 16, 3579. https://doi.org/10.3390/polym16243579.

Publications not included in this thesis or previous qualification work

1. B. Berzina et al., "Luminescence of AlN:Eu ceramics: Properties and mechanisms," *Opt Mater (Amst)*, vol. 127, p. 112217, May 2022, doi: 10.1016/j.optmat.2022.112217.
2. A. Antuzevics et al., "Thermal properties of paramagnetic radiation-induced defects in lithium orthosilicate containing breeder material," *Journal of Nuclear Materials*, vol. 565, p. 153713, Jul. 2022, doi: 10.1016/j.jnucmat.2022.153713.
3. R. Ruska et al., "Off-Stoichiometry Thiol-Ene Surface Functionalization: Example with Gold Nanoparticles" Materials 2024, 17(24), 6135; doi: 10.3390/ma17246135.

List of international conference presentations about thesis

1. Janis Cipa, Roberts Rimsa, Gatis Mozolevskis, "MICROFLUDIC MIXERS AND MAGNETIC PARTICLE CAPTURE CHAMBERS BASED ON OSTE POLYMER", *80th International Scientific Conference of the University of Latvia, Riga Latvia, 2022.*
2. Janis Cipa, Edgars Endzelins, Roberts Rimsa, Artis Galvanovskis, Arturs Abols, Aija Line and Gatis Mozolevskis, "OSTE DEVICE FOR MAGNETIC PARTICLE CAPTURE," *MicroTAS 2022 – 26th International Conference on Miniaturized Systems for Chemistry and Life Sciences, pp. 919–920, Jan. 2022.*
3. Janis Cipa, Roberts Rimsa, Gatis Mozolevskis, "Fabrication of passive microfluidics mixing device based on Off-stoichiometric thiol-ene and Cyclic olefin copolymer", *39th Scientific Conference of the Institute of Solid State Physics, University of Latvia, 28 february to 2 march, 2023.*
4. Janis Cipa, Felikss Rumnieks Roberts Rimsa, Aija Line, Gatis Mozolevskis "Gravity effects in zig-zag microfluidic mixers for light dye molecules?" *SMILS 2023, Stockholm, May 30-31, 2023.*
5. Janis Cipa, Edgars Endzelins, Roberts Rimsa, Arturs Abols, Aija Line and Gatis Mozolevskis, "Polydimethylsiloxane-free microfluidic technology for the rapid capture of extracellular vesicles from urine" *MicroTAS 2023, Katowice, Poland October 15-19, 2023.*
6. Janis Cipa, Edgars Endzelins, Roberts Rimsa, Arturs Abols, Aija Line and Gatis Mozolevskis. "Enhanced isolation of cancer-derived extracellular vesicles using PDMS-free microfluidic device" *40th Scientific Conference of the Institute of Solid State Physics, University of Latvia, March 5 -7, 2024.*

1. LITERATURE REVIEW

1.1. Cancer a complex disease

Cancer is a complex disease, that fundamentally is an alteration in multiple genes, that lead to dysregulation of normal cell growth and differentiation. In other words "Cancer is an abnormal growth of cells caused by multiple changes in gene expression leading to dysregulated balance of cell proliferation and cell death and ultimately evolving into a population of cells that can invade tissues and metastasize to distant sites, causing significant morbidity and, if untreated, death of the host." [3] Defining characteristics of cancer include its ability to invade locally, spread to regional lymph nodes, and eventually metastasise to various parts of the body. Clinically, "cancer" is an umbrella term used to describe hundreds of diseases with diverse observable characteristics (phenotypes). However, all cancers share fundamental similarities on molecular level, as they involve a common set of biochemical processes. These processes are driven by distinctive, though not identical, patterns of gene expression alterations. [6]

Risk factors for cancer include use of tobacco, alcohol, exposure to carcinogenic substances and ionising radiation. All these effects are accumulative over a lifetime further amplifying the age risk factor. Furthermore, aging decreases the effectiveness of cell repair mechanisms and the effectiveness of immune system. [7]

Cancer's prevalence in the human population cannot be understated, as it remains one of the leading causes of death worldwide. In 2020 alone, cancer accounted for nearly 10 million deaths, representing almost one in six deaths globally. [8] This staggering impact has driven an intense search for a cure and methods to reduce the societal burden of cancer, resulting in over 3 million research articles published in the last century. These efforts have led to significant advancements, including the development of new medicines [9], faster and more accessible diagnostics, improved screening techniques. [10] Among these innovations are therapies that assist the immune system [11], chemotherapy [12], and others [9].

Despite these advancements, cancer remains a leading cause of death. A persistent challenge across various treatments is their primarily localised effectiveness as metastatic cancers cause most cancer deaths. [13] This leads to 2 paths either the development of a treatment that works over the whole body without major side effects like in chemotherapy or faster cancer detection via low-cost and effective methods to detect cancer before metastasis. [7]

1.2. Prostate cancer

The difference between local and metastatic cancer is especially prominent for prostate cancer. The 5-year survivability if detected early and before cancer becomes metastatic is 99 % whiles the survival rate in case of metastatic cancer survivability

reduces drastically to 32 %. [14] The drastic difference has led to national programs for annual prostate testing for patients post 50 years of age in most developed countries.

Typical prostate cancer detection relies on initial PSA testing and biopsy confirmation. The issue lies in the high false positive result from PSA testing where a 6630 male trial suggests 30 % positive predictive value. [15] This value is concerning as positive predictive value is the number of cancers among all the positive tests, indicating the false positive case rate.

$$Positive\ predictive\ value = \frac{True\ postive}{True\ postive + False\ positve} \tag{1.2.1}$$

The challenge is further compounded by the difficulty in distinguishing between aggressive and indolent forms of prostate cancer. [16] This complexity is a key reason why prostate cancer is ranked as the 4th most common cancer overall and the 2nd most common among males, surpassed only by lung cancer [7]. Despite this, prostate cancer ranks 5th in terms of mortality. This ranking is largely based on PSA screening, typically combined with biopsy confirmation. However, as mentioned earlier, cancer detection and differentiation are highly complex processes, often resulting in low specificity and accuracy.

Furthermore, prostate cancer incidence rates (a metric used to measure cancer detection within a specific population as a distinct event) are highly variable worldwide. The age-standardized rate (ASR) was highest in Oceania (79.1 per 100,000 people) and North America (73.7), followed by Europe (62.1). Conversely, in Africa and Asia the incidence rates are lower than those in developed countries (26.6 and 11.5, respectively). [17] This data should be interpreted carefully as the country's development and healthcare accessibility is a core requirement for cancer screening, as well as age is the primary risk factor where prostate cancer becomes prevalent only after the age of 45. [18]

1.3. Early diagnostics

Early diagnostics is crucial not only in the case of prostate cancer but cancer in general, as local treatments are more effective and less taxing on the human body. This is due to the immense progress in cancer research, which has brought multiple methods to kill cancer cells, such as surgery, radiotherapy, and others. [3]

When assessing the effectiveness of a screening method, it is essential to consider the accuracy of the test (or its minimal error rate). Sensitivity measures the test's capability to accurately identify individuals with cancer within the cancer-affected population. [19]

$$Sensivity = \frac{True\ postive}{True\ positive + False\ negative} \tag{1.2.2}$$

In contrast, specificity measures the test's ability to accurately identify individuals who do not have cancer within the population that is cancer-free.

$$Specificity = \frac{True\ Negative}{True\ negative + False\ positive} \tag{1.2.3}$$

Perhaps the most vexing about screening for cancer is the paradox of cancer epidemiology: cancer in the aggregate over a lifetime is common, while at any one time one specific cancer is rare. That is, at any given time, cancer prevalence by specific type is low, and a single asymptomatic individual has a low risk of cancer. This is crucial to understanding the limitations of screening tests, since the positive predictive value (PPV) of a test is directly tied to cancer prevalence in the screened population. The lower the prevalence, the lower is the PPV. PPV has been very low among traditional tumour markers and has led to their failure as mass cancer screening tests [19]

The sensitivity and specificity show how well a test performed in a real-world scenario, which often leads to results that the test has failed as a detection method. Typical values for cancer detection are 70 to 80 % for sensitivity and 60 to 70 % for specificity. [19] This is a double-edged sword as there is a huge potential for improvement but also it shows that it is extremely challenging to develop a system with high sensitivity and specificity. Furthermore, due to lack of understanding of the cancer surrounding tumour growth dynamics and the timing of metastasis makes early detection challenging. [20]

A good example is PSA which tests for prostate cancer markers from liquid biopsy. PSA tests are simple and can be administered to large populations, but they have a high false-positive rate, or in other words, low specificity, with a positive predictive value of around 30 %. [19] This results in a considerable issue since testing for diseases can sometimes do more harm than good: Most men who have a PSA level above 4.0 ng/mL do not actually have clinical prostate cancer. While PSA screening might prevent one death in a 1'000, it leads to 110 men being diagnosed, and those who undergo treatment face the risk of serious health problems. Of falsely diagnosed group, 29 would develop erectile dysfunction, 18 urinary incontinences, two a serious cardiovascular event, and one deep venous thrombosis or pulmonary embolism. [21] The U.S. Preventive Services Task Force (USPSTF) thus concludes "that there is moderate certainty that the benefits of PSA-based screening for prostate cancer do not outweigh the harms," and discourages the routine use of this test. [21]

This limitation is one of the main reasons why liquid biopsies are primarily used as an initial screening tool rather than a definitive diagnostic method. The relatively low specificity of liquid biopsies has prompted the development of multiple strategies aimed at improving early cancer detection and differentiation between aggressive cancers and indolent tumours. These strategies include enhancing biopsy accuracy through imaging of biopsy cells [22], capturing and monitoring circulating tumour cells [23], and, more recently, analysing of EVs [24].

1.4. Extracellular vesicles (EVs)

EV field experienced rapid growth after 2013, primarily driven by the Nobel Prize award in Physiology or Medicine to James Rothman, Randy Schekman, and Thomas Südhof "for their discoveries of machinery regulating vesicle traffic, a major transport system in our cells" [4]. This recognition considerably boosted interest in EVs, drawing attention to their role in intercellular communication and disease processes leading to exponential growth in scientific publications (Figure 1.4.1.)

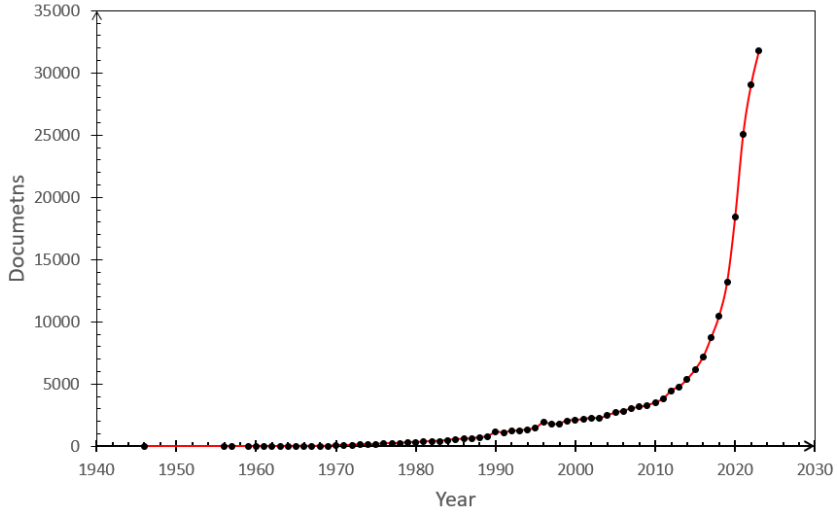

Figure 1.4.1. Published documents that include the words extracellular and vesicles, data collected from the Scopus database up to 2023.

Extracellular vesicles can be thought of as biological "messages" exchanged between cells. Cells package proteins, various types of RNA, and other molecules into lipid bilayer-bound vesicles and release them into the extracellular space, where they can be taken up by recipient cells. The specificity of this communication is mediated by surface markers on the vesicles – proteins embedded in the bilayer – that ensure only cells with compatible receptors receive the message. Once the EV is taken up, its contents are processed by the recipient cell's machinery, which can profoundly impact cellular behaviour, including processes such as growth, differentiation, and immune responses. [4]

A notable discovery in the field is that EVs released by cancer cells have distinct surface proteins and internal compositions compared to those from healthy cells [25]. If these differences can be detected with a high specificity and sensitivity, EVs could become a valuable marker for early disease detection. The concentration of EVs is proportional to the number of originating cells, meaning EV analysis could potentially distinguish between early-stage and advanced tumours. Furthermore, as EVs carry a variety of molecules – including RNA, DNA, and proteins – a comprehensive analysis of their contents could provide insights into disease states and even differentiate between aggressive and passive cancer types. [26]

One important advancement in related research field is the significant reduction in the cost of DNA sequencing, which has made disease screening and detection through liquid biopsies more feasible. By 2019, the cost of sequencing the human genome had dropped below $1,000, making high-throughput genomic screening a viable tool in both research and clinical settings. This development is particularly relevant for EV and single-cell analyses, as it allows for more detailed and accessible molecular profiling. [27]

The principles used for analysing circulating tumour DNA (ctDNA) in liquid biopsies provide a foundation for similar approaches in EV research. ctDNA, which is released into the bloodstream by tumour cells, has been used to monitor cancer dynamics without invasive biopsies. Although the exact mechanisms of ctDNA release are not fully understood, it is believed to result from a combination of active release by tumour cells, circulating tumour cells, and apoptotic bodies. [28] These methodologies, already proven in ctDNA analysis [29], can be adapted to EV research, accelerating the development of EV-based diagnostics.

Despite the surge in research, the implementation of EV-based diagnostics in clinical settings has been significantly hindered. One of the primary challenges lies in the lack of robust, efficient, and reproducible methods for isolating cancer-derived EVs. EVs exhibit a broad size range (from 30 nm to 2000 nm) and diverse molecular compositions, making them challenging to analyse using standard laboratory techniques. [30] These complexities must be addressed before EV-based diagnostics can reach their full potential.

Before EVs can be effectively analysed, they must first be separated from other components in biological samples, such as haemoglobin, antibodies, and cell debris. This can be achieved using either physical methods like ultracentrifugation or biological methods like immunomagnetic separation, which utilises antibodies to capture specific EVs. Refining these isolation techniques will be crucial for advancing EV-based diagnostics and realizing their potential for early disease detection, particularly in cancer. [30]

1.5. EV separation methods

Preprocessing liquid biopsy samples is a critical step in most biological tests as there is a need to extract only the molecules that the test can detect and to lower false negative possibility in the form of non-specific binding. In the case of EVs, this is particularly important as EVs are small and relatively fragile with factors like temperature, mechanical forces, and biological processes being the potential cause for EV rupture. If an EV is broken, its inner cargo containing meaningful biomarkers is released. For example, RNA, which is quickly broken down by ribonucleases found everywhere within the environment. Thus, it is imperative to keep EVs intact. Despite the EV fragility a lot of research has been dedicated to finding the best approach to EV separation, where the goal is high throughput and high yield.

Ultracentrifugation is considered the gold standard method for EV extraction, primarily due to its ability to isolate EVs based on differential sedimentation. In this process, particles in a biological sample are subjected to high centrifugal forces, which cause them to separate according to their size and density [31]. Despite its widespread use, ultracentrifugation has inherent limitations that impact the quality and yield of the extracted EVs. One such limitation is the co-sedimentation of smaller particles or contaminants that can accompany the EVs, leading to an impure sample and loss of yield. Furthermore, the application of high centrifugal forces – often exceeding 5000 g – induces shear stress on the vesicles, which can damage their structure. This mechanical stress results in the rupture or deformation of EVs, thus affecting their integrity and

functionality. As a result, the yield of biologically intact EVs is often suboptimal, making it imperative to explore alternative isolation methods that minimize these mechanical stresses and improve both the recovery rate and structural preservation of the vesicles [32].

Filtration is a separation process used to remove solid particles from liquids or gases by passing the mixture through a filter, which acts as a barrier that traps the particles while allowing the fluid to pass through. EV filtration can be problematic due to EV size distribution in the range 50 nm to 200 nm where the issue lies in the difficulty in separating EVs from microvesicles 100 nm – 1000 nm and apoptotic bodies 500 nm – 4 mm. [30], [33] This leads to difficulty of separating EVs from microvesicles and apoptotic bodies using just the pore size as there is a need for specific well controlled pores size which is difficult to fabricate. Furthermore, filtration processes can be prone to clogging, or require high pressures, thus leading to EVs breaking.

Coprecipitation is another method for EV separation with currently commercially available kits such as ExoQuick and Exo-Spin. The core principle of coprecipitation is to decrease EV hydration, thus reducing their solubility in the fluid, which causes them to precipitate (or solidify and separate out from the solution). This allows for easy and reproducible isolation using low centrifugal force, thus bypassing lengthy ultracentrifugation [34], [35] however, these kits are expensive for large scale use and lack EV-specificity thus they can only be used for non-specific EV separation. [30]

Size-Exclusion Chromatography is a bulk method that utilizes a gel with varied pore size. For size exclusion chromatography, a medium is filled with small beads which have pores, that span the entire particle. The pore size is precisely engineered to allow particles of specific size to pass through. As particles pass through the pores, they slow down compared to not passing through the pores. This leads to a time-based separation as larger particles which cannot enter pores reach the end quicker compared to smaller particles which are slowed down in the pores of the beads. Notably, in size-exclusion methods, there is no molecular interaction with the surface; separation relies solely on particle size. This approach has led to the development of commercially available kits, such as Sepharose (GE Healthcare) and qEV (iZon), tailored for various applications. While size exclusion can be adjusted based on specific needs by altering parameters like media type, pore size, flow rate, column dimensions, and packing, it still presents limitations, including lower resolution compared to other chromatography methods and challenges with processing sufficient sample volumes. [30]

Field Flow Fractionation is a separation technique that utilizes a force applied perpendicular to the flow. This force can be applied in multiple ways by using thermal gradient, electrical field and centrifugal force. There is also a relatively new method called asymmetric flow field-flow fractionation (AF4) which uses channels where one side of the channel has a permeable membrane. As the sample flows in the channel, a parabolic velocity profile is created due to the laminar flow. When the perpendicular force field is applied, analytes in the sample are driven toward the boundary. Brownian motion creates a counteracting motion such that smaller particles tend to reach an equilibrium position further away from the boundary. This type of separation spans a broad size range and could be applied to a wide variety of eluents [30]. AF4 has been demonstrated using microfluidics device for EVs separation with high throughput and continuous operation [2]. However, this method faces challenges

related to design complexity, sample recovery, and membrane clogging, which, combined with the relatively recent development of the AF4 method, have limited its widespread adoption.

Immunomagnetic separation is an affinity-based method that relies on the surface modification of either immovable surfaces or movable particles for the specific capture of EVs. These surfaces or particles are functionalised with antibodies that selectively bind to target EVs, enabling their isolation from complex biological samples. Affinity-based methods generally involve two key steps: the binding of EVs to protein-activated surfaces or particles, followed by the separation of the EV-bound particles from the rest of the sample. This approach facilitates the precise separation and enrichment of EV samples. [36] Although immunomagnetic methods are highly specific and effective, they are often associated with high costs and are typically limited to small sample volumes.

Both AF4 and immunomagnetic separation often face challenges such as high costs and difficulties in scaling. By integrating these approaches into microfluidic devices, many of these issues such as large sample requirements and high reagent costs can be mitigated. [37] Microfluidics enables precise handling of small volumes, potential automation and the ability to utilize higher surface to volume ratio. These advantages position microfluidic-based immunomagnetic separation and AF4 as promising alternatives, already outperforming ultracentrifugation [36], improving throughput [38] and enable single-cell analysis [39]. By utilising microfluidics with immunomagnetic separation, it has been shown that it possible to distinguish between cancer patients and healthy individuals within an hour using surface enhanced Raman spectroscopy in microfluidics device. [40]

1.6. Microfluidics

One of the first use of microfluidics dates to 1960s when Davids R. Deans developed microfluidics flow switching in capillary channels for gas chromatography. [41] The second major development happened in 1990 when microfluidics potential was recognised in the medical field, where the main drive was to reduce sample volume and enable small volume controls. [42]

Microfluidics development has diverged into three primary categories: organ-on-chip, droplet fluidics, and lab-on-chip systems. Organ-on-chip technology leverages fluid flow to induce mechanical forces, influencing cell behaviour and providing more accurate models of biological systems [43]. Droplet fluidics utilise immiscible mixtures, typically water and oil, to form discrete droplets. These droplets allow for the compartmentalisation of samples, enabling precise manipulation and control of individual sample units. [44] The lab-on-chip approach focuses on biological sample handling automatization while minimising reagent and sample volumes, thereby considerably reducing costs and improving testing efficiency. The small sample size also allows for integration of techniques that achieve higher resolution compared to traditional bulk methods. [45], [46]

From 2010 to 2018, the Theranos brought lab-on-a-chip technology into the public spotlight. The core concept behind Theranos technology was to revolutionize blood

testing by developing a device capable of performing a broad range of tests from a single drop of blood, significantly enhancing the testing experience. However, the technological challenges associated with accurately measuring such small sample volumes proved substantial [47]. Combined with the ambitious promise of a compact, universal blood-testing device, these challenges culminated in a major scandal and high-profile lawsuit [48]. This case had a negative impact on the lab on chip field, as the advertised capabilities, timelines, and scalability of the technology were not achievable at the claimed scale. As a result, subsequent research proposals in lab on chip faced heightened scepticism, as stakeholders grew more cautious about the feasibility of similar technological promises.

Nevertheless, the core principle behind Theranos' vision remains relevant, especially as circulating tumour DNA and EV research has advanced significantly by 2025. Although still in early stages, lab on chip technology using microfluidics devices has been used in small clinical trials with sample populations of up to 200 participants and has shown promising results, demonstrating the potential to differentiate between cancer patients and healthy individuals, albeit currently limited to specific cases. [40], [49], [50]

To address clinical needs for microfluidics devices, methods such as lithography, injection moulding, soft lithography and recently 3D printing have been used. Originally microfluidics devices were made using lithography and standard semiconductor processes. Starting from year 1998 polydimethylsiloxane (PDMS) was shown to be an excellent prototyping material for microfluidics devices. [51] This material offered relatively simple fabrication, biocompatibility, the possibility of bonding to itself and optical transparency which were ideal characteristics. Consequently, a new fabrication approach known as soft lithography was developed, leveraging PDMS's properties to enable versatile and accessible microfluidic device manufacturing.

1.6.1. Soft lithography

Soft lithography is characterized as a set of patterning techniques in which patterns are transferred onto a substrate using an elastomeric stamp. A typical case of soft lithography is show in Figure 1.6.1.

To create a useful microfluidics device, the material used for soft lithography must be:

- Easily removable from the master mould.
- Accurately preserve the texture of the original negative mould.
- Homogeneous and free from defects.
- Transparent to UV light.
- Have minimal surface roughness to reduce light scattering.

Due to these constraints, PDMS is typically employed for microfluidic applications. Its gas permeability is particularly advantageous for applications such as 'lungs on a chip,' which pioneered the practical implementation of organ-on-a-chip technology in the year 2010 [53]. In laboratory settings, PDMS is considered an ideal prototyping material due to its long shelf life, thermal curability, and acceptable adhesion properties. However, PDMS is known to absorb small hydrophobic molecules, which is problematic because most drugs and EVs are hydrophobic. This absorption can interfere with experiments, making PDMS less suitable for certain applications. [54] While surface modifications can reduce this issue, it complicates the fabrication process. Hydrophobic

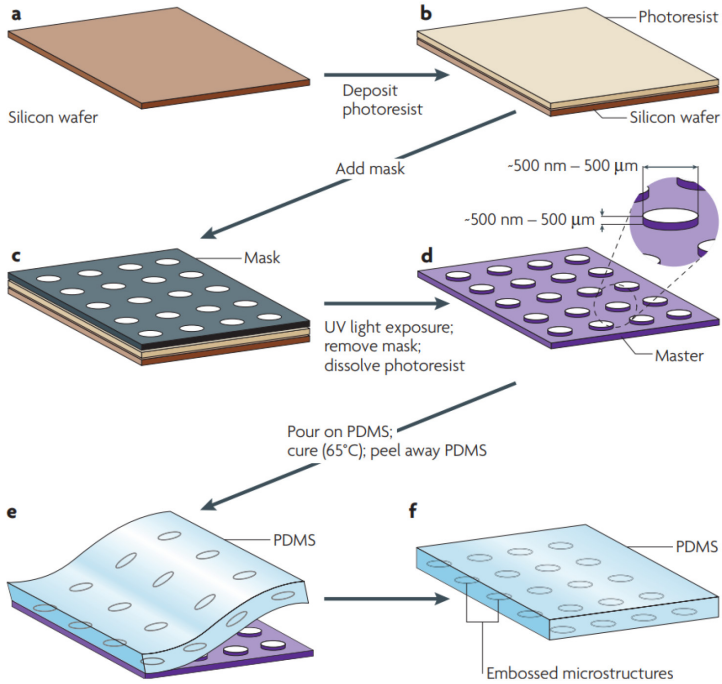

Figure 1.6.1. Soft lithography basics. [52] (reprinted with permission) a-b) negative photoresist is spin-coated on a silicon wafer. C) A mask is used to expose the desired design. d) negative photo resist is exposed with UV light and developed thus removing photoresist that is not cross-linked, forming master mould e) PDMS is poured on the master mould, thermally cured and peeled away. f) The resulting layer of PDMS has microstructures embossed on its surface.

molecule absorption, combined with PDMS incompatibility with standard plastics production and roll-to-roll technology, renders PDMS-based devices prohibitively expensive for large-scale production and unsuitable for large-scale drug or EV testing.

1.6.2. Microfluidics Materials

Glass

Glass has been a longstanding material in microfluidics field due to its excellent chemical resistance, optical transparency, and biocompatibility. Devices made from glass are typically fabricated using photolithography and wet etching, enabling the creation of precise and durable microstructures. However, the lithography fabrication process is both time-consuming and expensive, which limits its practicality for rapid prototyping and cost-effective production. Over the past decade, glass micro milling has emerged as a potential solution to reduce the time and costs associated with fabricating glass-based microfluidic devices. [55]

Despite this advancement, the widespread adoption of glass microfluidic devices has been limited, as suggested by publication data (Figure 1.6.2.1.). This limitation is likely

due to 2 factors the specialized skills required for glass milling and the significantly slower cutting speeds compared to materials like plastics or metals and the difficulty in achieving good quality, nontoxic bond for 2 glass pieces. [56] Although glass microfluidic devices offer a nearly ideal platform due to their superior properties, the challenges in fabrication development highlight the need for alternative methodologies or more cost-effective approaches that can simplify production and broaden accessibility.

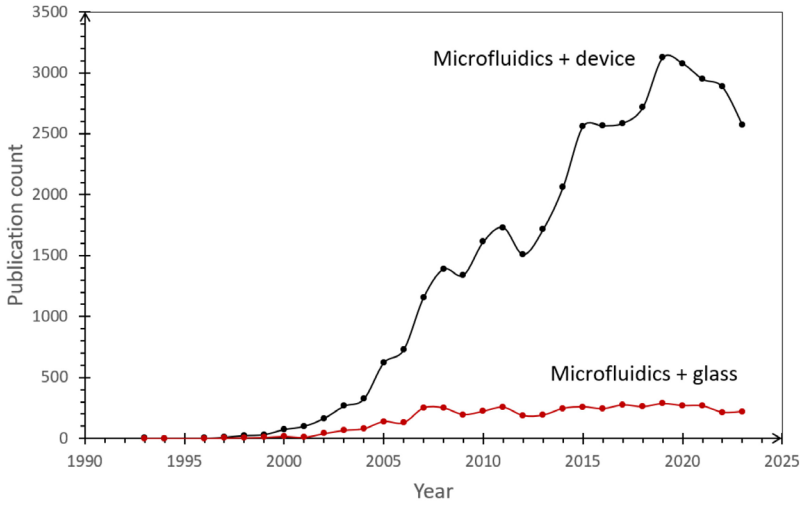

Figure 1.6.2.1. Publication indexed in Scopus data based with keywords: glass and microfluidic vs microfluidics and device. Data taken (10.09.2024).

Polymethyl methacrylate (PMMA)

Polymethyl methacrylate (PMMA) is a widely used thermoplastic in microfluidic prototyping, valued for its ease of machining, low cost, and excellent optical clarity. PMMA can be quickly and efficiently bonded using isopropanol in a simple curing chamber, making it ideal for rapid prototyping. However, despite these advantages, PMMA is often unsuitable for real-world applications due to its limited resistance to standard sterilisation processes. For instance, ethanol, a standard sterilisation agent, can dissolve PMMA, restricting its use in biomedical device applications.

Cyclic Olefin Copolymer (COC)

Cyclic Olefin Copolymer (COC) has emerged as a specialized thermoplastic with several advantages in microfluidics. It offers excellent optical clarity, high chemical resistance, and low hydrophobic particle absorption, making it ideal for a various biological and chemical applications. COC can be injection moulded, which facilitates scalable production of complex microfluidic devices.

A significant challenge in working with cyclic olefin copolymer (COC) lies in achieving reliable bonding, particularly in the fabrication of multilayer microfluidic devices. Unlike PDMS, which readily bonds to itself and other surfaces following plasma

treatment, COC requires specialized surface treatments or adhesives for effective bonding. Various research groups have explored solutions to this issue, employing techniques such as solvent vapor exposure or heated lamination, with relatively successful outcomes. [57] However, these additional steps introduce complexity to the fabrication process and can impact overall device integrity if not executed precisely.

The alternative of using adhesives is often avoided due to the risk of monomer leaching, which can compromise the device's biocompatibility and reliability. However, negative photoresists, such as off-stoichiometry thiol-ene (OSTE), present a promising alternative as an intermediate bonding layer between COC materials

Off-Stoichiometry Thiol-Ene (OSTE)

Off-stoichiometry thiol-ene (OSTE) is a newer material that is promising for microfluidics applications [58]. It combines the benefits of existing materials while offering unique advantages. OSTE polymers allow for adjustable mechanical properties and precise control over surface chemistry, which is beneficial for creating functional microfluidic devices as the forming polymer composition and concentration can be adjusted (Figure 1.6.2.2.)

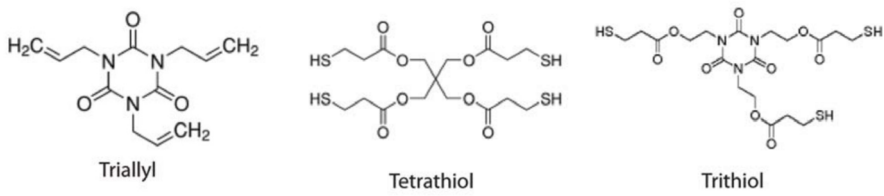

Figure 1.6.2.2. Monomers that are used in OSTE, in combination with photo initiator. [58]

OSTE has low shrinkage during curing and forms strong bonds with various substrates, making it a versatile material for both prototyping and potential large-scale production. Its compatibility with standard microfabrication techniques further enhances its appeal as an alternative to PDMS and other conventional materials, especially in applications requiring high biocompatibility and chemical resistance.

Due to these benefits, in the scope of this dissertation OSTE and COC will be used in a tandem device to utilise the excellent optical properties of COC and the ease of fabrication and biocompatibility of OSTE.

1.6.3. Emerging fabrication method

The shift from traditional materials such as PDMS to alternatives like OSTE has catalysed the development of new microfluidics fabrication techniques. This transition has been driven by the need for faster, more cost-effective, and versatile production methods. By integrating traditional injection moulding with soft lithography's rapid and flexible capabilities, techniques such as reaction injection moulding using click chemistry [58] and CNC milling of plastic substrates followed by bonding have emerged as viable alternatives [59], [60].

In addition to these methods, 3D printing has become increasingly valuable in microfluidics. It offers rapid production speeds and a broad range of material options, potentially replacing the expensive and time-consuming master mold production required in soft lithography. [61] Recent advancements in resin 3D printers, with sub-50μm pixel sizes emerging in the past three years, have brought 3D printing closer in resolution to traditional soft lithography processes [62]. This progress enables microfluidic development to move outside the confines of clean rooms, significantly reducing production costs and time. The ongoing development of biocompatible resins and high-resolution 3D printers holds promise for further advancements in microfluidics, allowing for single-step fabrication and increased design freedom compared to standard lithography. However, as of 2024, these methods are still in their nascent stages, with adoption remaining relatively slow. [63]

The advent of these new fabrication methods has enhanced the ability to create complex microfluidic devices with multiple integrated modules. By exploiting various physical phenomena, such as magnetic fields and locally induced vortices, and incorporating them into precisely engineered geometries, researchers can introduce new functionalities within microfluidic systems. This expanded design freedom is set to push the boundaries of what is achievable in microfluidic technology, offering new possibilities for applications and innovation in the field.

1.7. Magnetic capture

Magnetic capture is the basis of the immunomagnetic separation technique, as by use of magnetic field it is possible to separate bound analyte from the rest of the flow. The basic principle stems from Lorentz force law, which states that a charged particle moving in a magnetic field will experience force, that is related to magnetic field, particle charge, and particles velocity (1.7.1) [64]:

$$\vec{F} = q(\vec{E} + \vec{v}\, x\, \vec{B}) \tag{1.7.1}$$

- F – Lorentz force (N)
- q – Charge of the particle (C)
- E – Electric field intensity (V/m)
- v – Velocity of the particle (m/s)
- B – Magnetic flux density (T)

In case of immunomagnetic separation charge is difficult to determine as, magnetic particles do not have charge whiles proteins on the surface might have some charge that for the scope of this dissertation will not be considered. An equation to determine the attraction of a magnetic particle to a magnet, without considering the influence on the medium, can be described using Equation 1.7.2 [65], [66]:

$$\vec{F} = (\vec{m} \cdot \nabla)\vec{\mathrm{B}} \tag{1.7.2}$$

Where

- m – Magnetic moment (A^*m^2)
- ∇ – Gradient
- B – Magnetic flux density (T)

Based on Equation 1.7.2, it is observed that the magnetic particle core material is important as it contributes to the force; thus, while iron core particles can be used, improvements may be achieved with more advanced alloys, such as those found in neodymium magnets. Furthermore, the force is based on the gradient of the magnetic field thus a higher gradient is advantageous, even more so in case of a magnet array where there is not only a single gradient at the ends of the magnet but a strong gradient after each magnetic element. This could potentially lead to improved attractive force for a moving particle. Lastly $\vec{B}$ is the magnetic strength thus a stronger magnet improves the gradient and by using a stronger magnet there would be stronger magnetic force. While the distance to the magnet is a hidden variable in Equation 1.7.2 it is still present as it is responsible for the gradient strength and the fundamental force follows a quadratic relationship. [67]

To utilize magnetic force in microfluidics device a chamber for capture is required. Fortunately, previous research presents a study of flow characteristics in a chamber [68]. Figure 1.7. notes simulations of different chamber geometries showing the optimal design to ensure flow homogenously and reduced bubble generation.

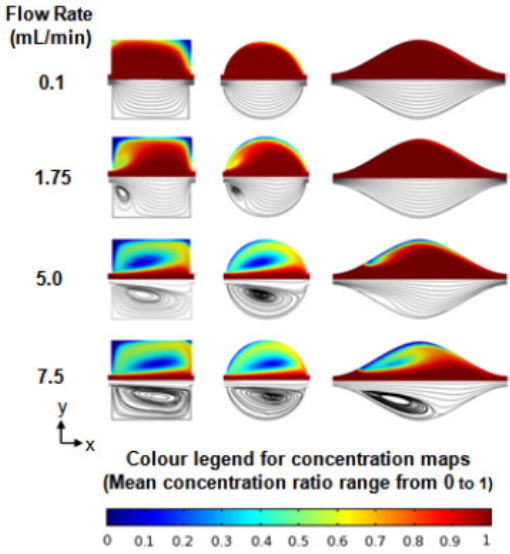

Figure 1.7. Simulation results of different chamber geometries showing concentration maps (top) and streamlines (bottom). [68].

Based on this design the optimal design concept can be drawn, a smooth circular chamber that has relatively small angle is optimal as flow is kept at the chamber sidewalls and the formation of new boundary layers is minimal, thus ensuring no bubble generation, optimal flow, and no dead zones. With the chamber design finalized, the magnet configuration is still in question, for which the dimensions of the chamber must be considered

1.7.1. Magnet types and different arrays

After defining the magnetic chamber geometry, magnetic setup or array must be chosen. Magnet arrays can be split into 2 categories: stable and unstable. While there are various configurations for both categories, a few are more commonly used. One of the most common stable configurations is magnets stacked in alternating polarity, which can be easily assembled and offer magnetic field distribution as shown in Figure 1.7.1.

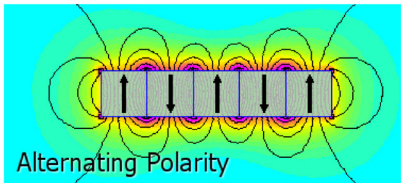

Figure 1.7.1. Schematic of magnets stacked in alternating polarity. [69]

This configuration is useful due to the ease of assembly and the combination of the magnetic strength of multiple smaller magnets. Yet in cases where stronger magnetic field is required or there is tight constraint on magnetic field direction the Halbach array can be used as indicated by Figure 1.7.2. Halbach array leverage magnetic field properties to direct magnetic force mostly in a single direction. This has two benefits increased magnetic strength on one side of the magnet potentiality doubling it while using the same magnets and reducing force on the other side. [70] Unfortunately, Halbach array comes with a major disadvantage: it is an unstable configuration, that does not naturally stay together as it is with alternating polarity. To address this, strong adhesives or mechanical fixation must be used, as the magnets not only need to be pushed together but also maintained in the correct orientation. While there are strategies to address this engineering challenge, the brittleness of both the magnets and adhesives makes the system prone to breaking. Combined with the increased magnetic strength, this can be a major hazard and a handling challenge.

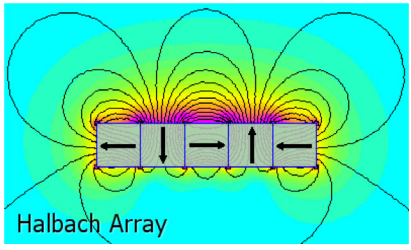

Figure 1.7.2. Schematic of Halbach array. [69]

Due to Halbach arrays enhanced magnetic field strength, they are commonly employed in advanced applications such as MRI machines, high-performance electric engines, maglev trains, and brushless DC motors. However, in more conventional devices, such as typical motors, magnetic sensors, and loudspeakers, alternating

polarity configurations are still preferred due to their lower fabrication complexity and the natural stability of the array [67]

For microfluidic applications, the choice of the array depends on the channel geometry, as the required magnetic field can have highly specific constraints and requirements of no magnetic field just next to the channel, for instance. While magnetic strength plays a key role, the flow delivering magnetic particles is equally important, as the magnetic attractive force is influenced by the particle speed. This shows the importance of mixing parameters as in a continuous device mixing and capture parameters should ideally be identical or only governed by passive function such as channel geometry.

1.8. Mixing in microfluidics

Before MP can be used for separation, they must first capture EVs, which can be done in 2 ways, either in flow capture by flowing the MPs and EVs in 2 liquids, which are subsequently mixed thus interaction can occur, or by fixing MPs to the surface and allowing the EVs to pass over them. An issue regarding two flows is that in microfluidics flow typically is laminar and mixing is difficult to achieve. To quantify how laminar the flow is, a dimensionless quantity known as Reynolds number (Re) can be used. Reynolds number is the value that represents the ratio between inertial and viscous forces. The inertial forces are represented by the product of the fluid's density (ρ), characteristic velocity (u), and characteristic length scale (L):

Inertial Forces $\propto \rho \cdot u \cdot L$

Viscous forces are the internal frictional forces within the fluid that arise due to its viscosity (μ). These forces resist the relative motion between fluid layers, leading to energy dissipation as heat. Viscous forces tend to dampen the motion of the fluid, smoothing out velocity gradients and slowing the fluid flow. In the context of the Reynolds number, the viscous forces are represented by the product of the fluid's viscosity (μ) and the characteristic length scale (L) divided by the characteristic velocity (u):

Viscous Forces $\propto \frac{\mu L}{u}$

As Reynolds number is the ratio of inertial and viscous forces it is defined by Equation 1.8.1, [71]:

$$Re = \frac{uL}{v} = \frac{\rho u L}{\eta} \tag{1.8.1}$$

Where

- ρ is the density of the fluid (kg/m^3)
- u is the characteristic velocity (m/s)
- L is a characteristic length (m)
- η is the dynamic viscosity of the fluid ($kg/(m \cdot s)$)
- ν is the kinematic viscosity of the fluid (m^2/s).

L the characteristic length, is defined as ratio between the volume of a body divided by its surface area, as such it can be used in different systems, including airplane wings, ship hulls, air ducts, or fluid pipes. To better describe a fluid pipe system Reynolds number of derivatives can be used such as [72]:

$$Re = \frac{uD_H}{v} = \frac{\rho u D_H}{\eta} = \frac{\rho Q D_H}{\eta A} = \frac{W D_H}{\eta A} \tag{1.8.2}$$

- D_H is the hydraulic diameter of the pipe (the inside diameter if the pipe is circular) (m),
- Q is the volumetric flow rate (m^3/s),
- A is the pipe's *cross-sectional* area ($A = \pi D^2/4$) (m^2),
- u is the mean velocity of the fluid (m/s),
- η is the dynamic viscosity of the fluid ($kg/(m \cdot s)$),
- v is the kinematic viscosity ($v = \mu/\rho$) (m^2/s),
- ρ is the density of the fluid (kg/m^3),
- W is the mass flow rate of the fluid (kg/s).

This definition is typically used for ducts and pipes which is exactly what is used in the scope of microfluidics. Furthermore, this equation is generally used for a circular pipe for which the hydraulic diameter is equal to the inside pipe diameter. However, microfluidics devices often have square channels due to fabrication techniques. In such a case a square or rectangular derivative for hydraulic diameter D_H can be used [73]:

$$D_H = \frac{4A}{P} \tag{1.8.3}$$

Where A is the cross-sectional area, and P is the wetted perimeter. The wetted perimeter for a channel is the total perimeter of all channel walls that are in contact with the flow.

By calculating the typical Reynolds number for a microfluidics system with a flow rate from 0.1 µl/min to 1000 µl/min and channel sizes from 10–1000 µm Reynolds numbers are in the range from 10 to 1000 thus flow is strictly laminar without any turbulence. Laminar flow is more predictable and can be easily managed, but in a case where there is a need to combine two liquids it is rather difficult. This is a problem as there are multiple occasions where there is a need to mix a sample and a reagent in sample preparation.

Consider mixing of water and rhodamine B, a red dye molecule that can be used for cell colouring, in a microfluidic device. First diffusion speed must be determined which can be calculated using Equation 1.8.4 [74]:

$$L = \sqrt{Dt} \tag{1.8.4}$$

Where L – characteristic diffusion length (m), D – diffusion coefficient (m^2/s), t – contact time (s).

To determine the diffusion speed of a dye molecule in water solution diffusion coefficient for the specific dye must be known. To calculate the diffusion coefficient the Einstein-Smoluchowski relation can be used: [75]

$$D = \chi k_b T \tag{1.8.5}$$

Where

D – diffusion coefficient (m^2/s)

χ – mobility of the particle ($m^2/(Ns)$)

k_b – Boltzmann constant ($kg \cdot m^2/(s^2 \cdot K)$)

T – absolute temperature (K)

Mobility of the particle is a complex term that can be substituted under low Reynolds conditions, which is the case for microfluidics results in Equation 1.8.6 [76]:

$$D = \frac{k_B T}{6\pi\eta r} \tag{1.8.6}$$

Where
D – diffusion coefficient (m^2/s)
k_B – Boltzmann constant ($kg \cdot m^2/(s^2 \cdot K)$)
T – absolute temperature (K)
η – dynamic viscosity ($kg/(m \cdot s)$)
r – particle radius (m)

Now all but the molecular radius is known. To acquire a theoretical molecular radius an estimate can be used based on molecular mass, Avogadro number and spherical molecular assumption:

1. **Molar volume**: The volume of one mole of a substance, Vm, is given by:

$$V_m = \frac{M}{\rho} \tag{1.8.7}$$

Where M is the molar mass and ρ is the density.

2. **Volume of single Molecule**: The volume V of a single molecule is:

$$V_{1m} = \frac{V_m}{N_A} = \frac{M}{N_A \rho} \tag{1.8.8}$$

Where N_A is Avogadro's number.

3. **Spherical Volume**: Assuming each atom or molecule is approximately spherical, the volume is also:

$$V = \frac{4}{3}\pi r^3 \tag{1.8.9}$$

4. **Equating Volumes**: Setting the two expressions for volume equal gives:

$$\frac{4}{3}\pi r^3 = \frac{M}{N_A \rho} \tag{1.8.10}$$

5. **Finally, solving for r gives an approximate molecular radius**:

$$r_M = \left(\frac{3M}{4\pi N_A \rho}\right)^{\frac{1}{3}} \tag{1.8.7}$$

Where
M – molecular mass (kg/mol)
N_A – Avogadro's number (mol^{-1})
ρ – Density of the fluid (kg/m^3)
r_M – molecular radius (m)

Considering the example of rhodamine B, the atomic radius can be calculated using Equation 1.8.7 resulting in a radius of 5.6 Å. Furthermore, by calculating the diffusion coefficient for rhodamine B using Equation 1.8.6 the resulting value of 3.8×10^{-10} m^2/s is obtained. Considering the imprecision introduced by the spherical assumption, the theoretical value is reasonably aligned with experimental results found in the literature $D = 4.3 \times 10^{-10}$ m^2/s. [77]

Finally, consider a scenario where aqueous solution of rhodamine B is mixed with water in a microfluids device with flow rate of 100 µl/min and channel size of 200 µm. To fully mix such a system it would take 55 seconds, but it would result in a length of 570 mm spanning 7.5 times across a typical microscopy size device (75.5 mm × 25.5 mm), thus making it an impractical solution

To address this issue, researchers have developed multiple designs that induce secondary flow and local vortices that act to break the boundary layer between 2 liquids thus drastically improving the diffusion speed. [78]

1.8.1. Active mixers

One way to improve diffusion is by stirring or agitating the fluid flow using some form of external energy supply. Active mixers typically use acoustic/ultrasonic, dielectrophoretic, electrokinetic time-pulse, pressure perturbation, electro-hydro-dynamic, magnetic or thermal techniques to enhance the mixing performance.

Acoustic/Ultrasonic Actuation

Acoustic actuation typically uses a piezoelectric actuator to induce acoustic waves in the flow stream. The acoustic waves frequency can vary from few a kHz to hundreds of MHz. Unfortunately, using acoustic waves come with a high energy consumption and subsequently high temperature increase for the flow. For example Yang et.at. used 60 kHz and 50 V excitation which mixed 2 liquids effectively but resulted in a 16 °C temperature increase. [79] Alternatively Lamb waves or radio waves can be used with varying success. [80], [81]. Overall, acoustic waves can be used to mix 2 liquids, but it often can result in rather high temperature increase, which can be unacceptable in case of biological samples.

Electrokinetic

An active liquid control can be realised using electroosmosis, where electrodes are placed on either side of the channel, and an alternating electric field is applied. The flow is created due to the accumulation of charges on the surface, which in turn attracts counter ions from the fluid forming an electric double layer near the surface. When an electric field is applied along the length of the channel, these counter-ions move, dragging the surrounding fluid with them due to viscous forces. This movement of fluid is called electroosmotic flow (EOF) (Figure 1.8.1.1).

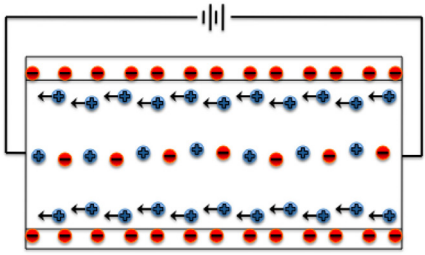

Figure 1.8.1.1. Schematic depiction of Electroosmotic flow through a small channel, showing charged ions and applied voltage.

Electroosmosis can be used for enhancing mixing within microfluidic systems if the potential is applied in a specific way to induce instability. This concept was demonstrated by Chia-Yen Lee et al., who investigated the effects of localized capacitance variations in generating zeta potential differentials along silica-based microchannel

surfaces. Numerical simulation data from their study depicted in Figure 1.8.1.2, shows the influence of applying a 300V longitudinal electric field alongside an 800V alternating voltage at 1/6 Hz across electrodes positioned perpendicular to the flow direction demonstrating mixing using electrokinetic force. [82]

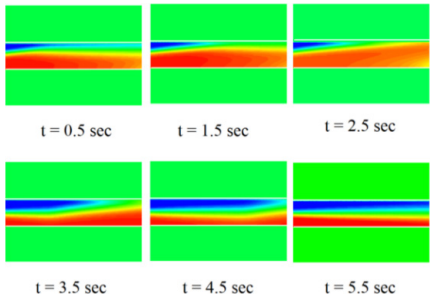

Figure 1.8.1.2. Numerical simulation data where 300V is applied in the longitudinal direction and a 1/6 Hz 800V alternating voltage is applied on electrodes perpendicular to the flow. [82] reprinted with permission.

Mixing using electrokinetic forces can be enhanced if the channel geometry is specifically designed to support such mechanisms. For instance, this was demonstrated by Wu et al., who maintained a uniform electric potential at the wall surface. This setup allowed the non-uniform distribution of the electric field near the conductor segment to generate localized vortices, which could be effectively utilized for mixing, as illustrated in Figure 1.8.1.3. [83]

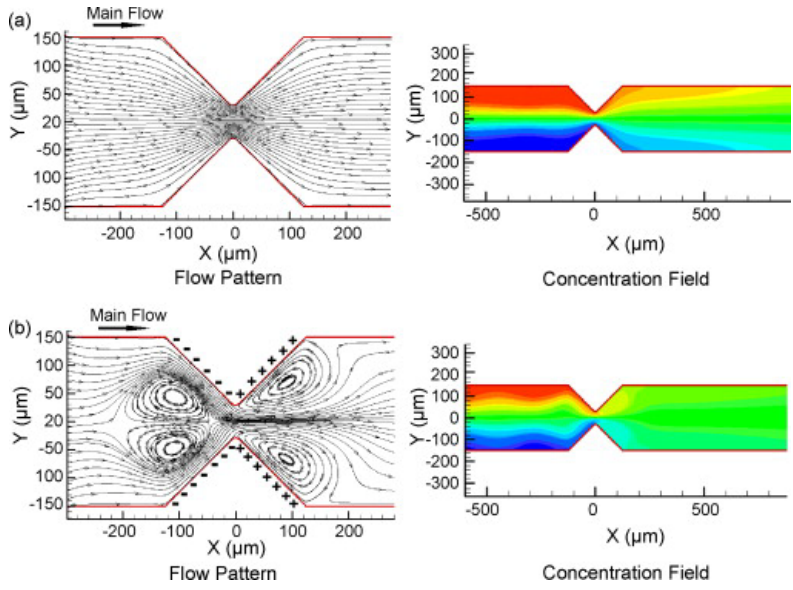

Figure 1.8.1.3. Numerical modelling of flow and concentration fields with (a) a pair of non-conducting hurdles and (b) a pair of conducting hurdles. [83]

While multiple electrokinetic actuation examples can be used for mixing and pumping of liquid, their downside is the potential influence on the sample due to the requirement of ions in the fluid and high voltage.

Thermal Actuation

Thermal Actuation works by locally heating a fluid to its critical phase change, thus bubble nucleation occurs and it acts as a piston to displace fluid away from itself. A relatively simple engineering solution is mixing using thermal bubbles, as only a small local heater is needed to achieve mixing. [84] (Figure 1.8.1.4.) Yet this simplicity is potentially outweighed by the fluid temperature increase near the thermal bubble with temperatures up to 100 °C which could irreversibly damage biological samples. [84]

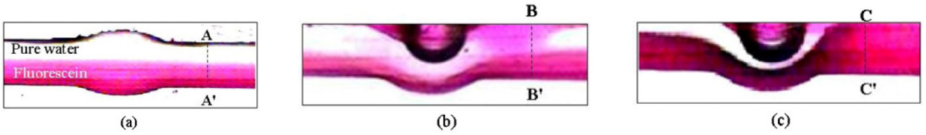

Figure 1.8.1.4. Mixing results of two heterogeneous liquids under the action of different disturbing times: (a) non-thermal bubble forming and (b) and (c) thermal bubble with diameters of 50 μm for 3 s and 5 s, respectively. [85]

Magneto-Hydrodynamic Flow

Magneto hydrodynamic flow is one of the more interesting solutions, leveraging the concept of turbulence on typical scale. As such microscopic magnetic particles are introduced into the fluid, and by applying a varied magnetic field, the tiny stirring bars are rotated, thus inducing local vortices and improving mixing. [86], [87] (Figure 1.8.1.5.)

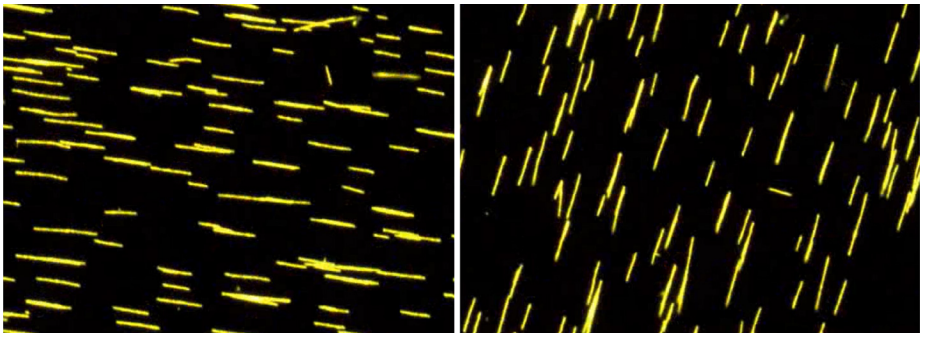

Figure 1.8.1.5. Microchain magnetic steering, snipet from a video. [87]

Pressure perturbation

Pressure perturbation is a method to induce chaotic advection and improve mixing without additional engineering complexity, such as electrodes, piezoelectric

components, or in fluid particles. This is achieved by pulsing side channels without adding additional fluid but by opening and closing valves on the side channels, thus creating a pressure perturbation and inducing chaotic advection. (Figure 1.8.1.6.) This process notably improves mixing, yet constant pressure change could be detrimental to biological samples such as cells or EVs.

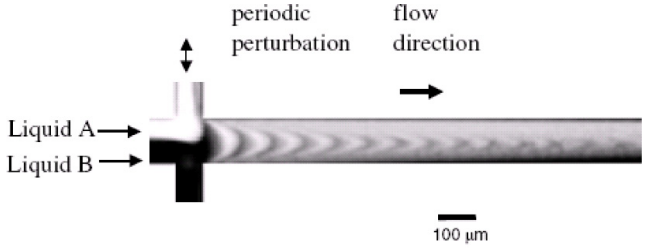

Figure 1.8.1.6. Model of a chaotic mixer with multiple side channels. (a) Experimental results of mixing in the device with one pair of side channels. The pressure perturbations induce lobe-like distortions of the interface and facilitate rapid mixing [88]

As previously noted, multiple active mixing methods exist that can achieve fast and effective mixing. However, active mixing methods come with a significant disadvantage: they require actuation or specific flow controls, which adds complexity through the inclusion of components such as valves, peristaltic pumps, or piezoelectric elements. These additional components must be accounted for during device operation and integrated within the channel system. This integration can often be impractical or unfeasible, especially in biological systems, where interactions with various materials may induce toxicity, and rapid pressure changes could compromise the stability of cells and EVs. Such limitations highlight the challenges of employing active mixing in microfluidic systems designed for sensitive biological applications.

1.8.2. Passive mixers

Passive micromixers offer solutions to many of the challenges posed by active micromixers, making them a viable alternative. Passive mixers take advantage of specifically engineered geometries to induce local vortices. These local effects can be described with Dean vortices and secondary flow. The core idea is to reduce liquid boundary layer thus improving diffusion as the contact area is increased. This can be done in a variety of ways and is separated multiple categories.

Lamination

The concept of lamination stems from the inertial effects present in microfluidic channel. When a fluid in a laminar state is forced in a sharp turn, the inertial forces push the denser fluid against the wall thus increasing the contact area between 2 fluids. Tofteberg et al. [89] showed that by using microchannel with 90° angles it is possible to

double the contact angle between recombining fluids. Using this method, it is possible to add multiple sequential segments to achieve high mixing efficiency.

This concept was further developed for different geometries, for example a T shape channels. Using numerical simulations Roudgar et al. [90] showed that sharp-angle passive mixers can induce local vortices at Re > 100 thus leading to improved mixing. A notable example illustrating the challenges in obtaining high-quality mixing data is provided by Ait Monheb et al. [91], who attempted to compare numerical modelling results with experimental data. Their findings revealed the formation of vortices and demonstrated that cross-shaped channels exhibited improved mass transfer at lower Reynolds numbers compared to T-shaped channels.

Chaotic advection

Previous examples have demonstrated that lamination can be useful for mixing, but the introduction of vortices can enhance this process. This phenomenon is often referred to as chaotic advection, which describes the chaotic behaviour observed even in laminar flow regimes due to inertial effects at low Reynolds numbers. Chaotic advection can be induced through sharp geometries or by combining two fluid paths, leading to increased mixing efficiency. Designs based on chaotic advection typically target microfluidic flows with Reynolds numbers between 1 and 100, where the inertial effects are strong enough to disrupt the regular flow pattern and enhance mass transfer.

Li et al. [92] proposed a Planar Asymmetric convergent-divergent micromixer containing dislocation sub channels (Figure 1.8.2.1.) which was a modification of the micromixer proposed by Ansari and Kim [93]. The experimental data and simulation results indicated that for Reynolds numbers between 1 and 100, the sub-channel dislocation structures enhanced mixing performance. This improvement was due to the combined effects of unbalanced inertial collisions, multidirectional vortices, and collision-induced flow within the mixing cavities between adjacent two-looped structures. [37]

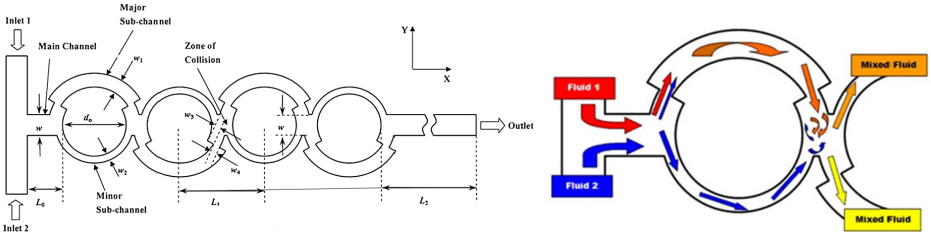

Figure 1.8.2.1. Schematic illustrations of planar asymmetric convergent-divergent micromixer with dislocation sub-channels. [92]

Continuing the convergent-divergent channel concept and simplifying the design a sinusoidal geometry was developed by Alzal et al. (Figure 1.8.2.2). Sinusoidal geometry was tested for Reynolds number from 10 to 70 and it showed that mixing was improved due to secondary flow which was present in the sub-channel. Furthermore, mixing was further enhanced by vortices forming at the converging points in the channels. This led to a higher than 90 % mixing using 8 sinusoidal segments. [94]

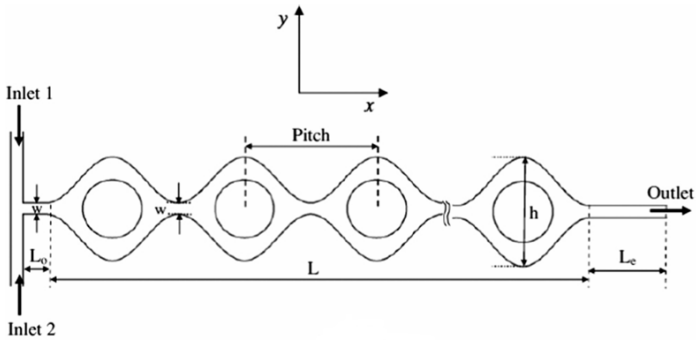

Figure 1.8.2.2. Schematic illustration of a sinusoidal convergent-divergent micromixer. [94].

Further development and simplification of the design yielded a zig-zag geometry. [95] (Figure 1.8.2.3.) Sinusoidal zig-zag mixer showed interesting properties as the mixing efficiency dropped at Re under 10 as mixing was dominated by diffusion, whiles for Re greater than 20 mixing was enhance due to Dean vortices at the corners of the channel. [95]

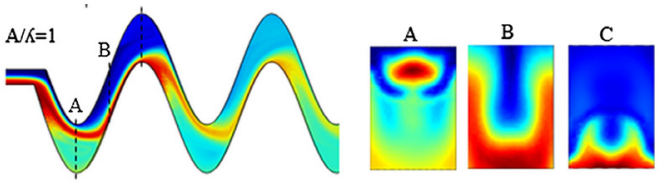

Figure 1.8.2.3. Numerical simulation illustrating the concentration distribution of methylene blue in a sinusoidal zig-zag micromixer at Re = 50. [95]

While some research groups have focused on developing simpler designs to improve integration and reduce fabrication complexity, others have pursued the opposite approach, aiming to achieve maximum performance within the smallest possible space. These efforts often involve more intricate designs and advanced fabrication techniques to optimize fluid dynamics and enhance functionality, despite the added complexity in fabrication and integration. Both strategies highlight the diverse approaches within the field of microfluidics, each addressing different priorities depending on the specific application requirements.

3D structures

In research done by Lin et al. a 3D zig zag mixer was developed as seen in Figure 1.8.2.4. [96] The mixer was developed for high flow rates ranging from 0.6 to 4 ml/min and had a lower pressure drop compared to similar-sized mixers. Unfortunately, the mixer fabrication required precise micro-fabrication techniques, as the channels were just 50 μm in diameter, making scaling both challenging and expensive. Nevertheless, they achieved nearly perfect mixing of 0.99 at 50000 μm length placing it in the mid-range compared to other devices, primarily due to the relatively long channel length.

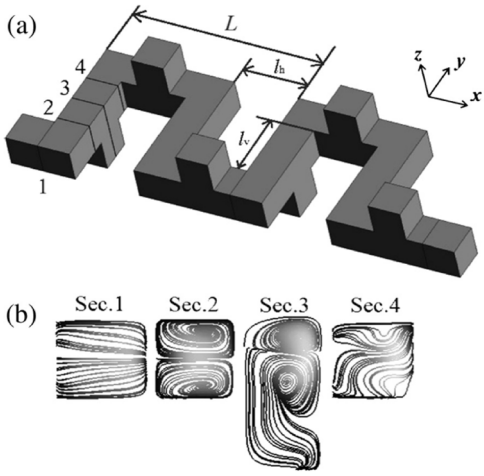

Figure 1.8.2.4. "(a) Schematic of the micromixer flow path. The parameter L denotes the span of each element along x axis, and l is the length of each straight section. The subscript h is the horizontal section (section along x axis), and v is the vertical section (section along y axis). (b) Streamlines from the CFD simulation at four cross-sections (Re = 64)." [96]

Yang et al. presented a 3-spiral micromixer. (Figure 1.8.2.5.) This micromixer was developed to enhance Dean vortices and their propagation, thus potentially improving the mixing. The presented results indicated a moderate success with a micromixer length of 2340 μm and a perfect mixing index of 0.99.

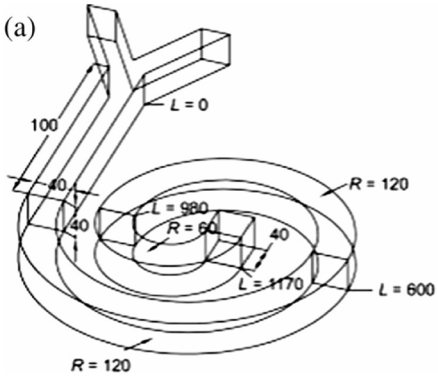

Figure 1.8.2.5. Schematic of a spiral micromixer with a spiral trending upwards. [97]

Due to the fabrication complexity of 3D structures, there has been a lot of research in embedding barriers in the microchannel, as it could potentially improve mixing compared to chaotic advection mixers and make the design a lot simpler to fabricate.

Embedded barriers

One of the most popular mixing designs is the herringbone structure. It relies on a microfluidics channel with barriers placed under the flow, thus as the fluid passes over them it is moved upwards creating vortices and improving mixing. (Figure 1.8.2.6.) This designs success lies in good mixing performance, modularity and relatively simple fabrication, thus combining multiple useful qualities. The performance of optimized channels has a mixing efficiency of 0.83–0.95 with a channel length of 3–5 mm respectively. [98], [99]

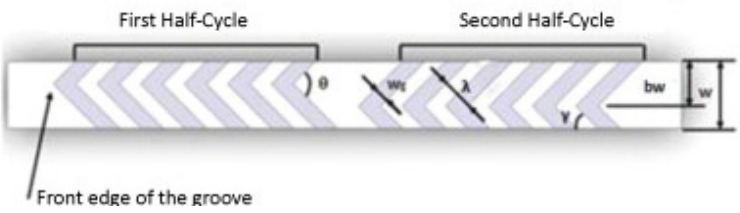

Figure 1.8.2.6. Herringbone structure schematic. [99]

As discussed, there are multiple different designs and strategies of how to achieve mixing in microfluidics devices where the choice is not trivial and is highly dependent on the required use case. In case there is need for a small size mixer or optional pumping function is required, most likely an active mixer should be chosen. Alternatively, if fabrication and integration complexity is paramount for example in case of single-use devices a passive mixer is most likely needed. Lastly if a mixer that is both highly efficient and does not need complex assembly is necessary, a type of 3D structure mixer should be used.

1.9. Evaluation of mixing efficiency

In the previous section mixing efficiency was mentioned multiple times. At the same time, on the surface, the mixing concept is self-explanatory, yet the intricacy of precise and comparable value is somewhat elusive. The main question is how to guarantee precise definition so that every research, regardless of the setup or dye used can mathematically calculate a value that can be directly correlated to other groups. To address this issue multiple mixing index definitions have been developed. [100], [101], [102], [103]

The core idea behind the mixing index is to establish an optical system with minimal measurement variability. Typically, a reference point at the end of the channel is chosen, and images of an empty channel and one containing only the dye solvent (usually water) are captured while locking image parameters. The next step involves flowing the dye solution into one inlet and the solute into the other, allowing for mixing along the device. By comparing images of the empty channel or solvent-filled channel to those with the dye at the endpoint, the extent of mixing can be quantified. The base equation to mathematically evaluate the difference between unmixed and mixed state can be written as Equation 1.9.1 and is called mixing index [104]:

$$\sigma = \sqrt{\frac{1}{N}\sum_{i=1}^{N}(I_i - < I >)^2} \tag{1.9.1}$$

Where

σ – standard deviation of the pixel intensities

I_i – local pixel intensity

$<I>$ or I_{mixed} – average pixel intensities in the cross-section.

N – total number of pixels

Using the above equation mixing index is computed using pixel intensities across a cross-section of grayscale image. "Although a measure of simple standard deviation yields information regarding the spread of data about the mean intensity, it is not a direct measure of the extent of mixing because the index possesses a dimension of intensity. Hence, comparison of mixing extent among different studies is not possible using this index." [105]

One way to address this issue is to render mixing index dimensionless by comparing the standard deviation to the mean intensity. [106] This ratio is called the absolute mixing index (AMI) which can be calculated using Equation 1.9.2:

$$AMI = \frac{\sigma}{<I>} = \frac{\sqrt{\frac{1}{N}\sum_{i=1}^{N}(I_i - <I>)^2}}{<I>} \tag{1.9.2}$$

Equation 1.9.2 yields a scale of 0 to 1 where 1 is an unmixed state while 0 is a fully mixed state. In this case a fluorescence microscopy is ideal as lack of fluorescence is a lot easier to achieve than a truly black visible dye. The issue with Equation 1.9.2 is that while a correct value can be acquired it will not be comparable to a similar system with different lighting or different dyes. This is due to the problem of taking images and doing quantification analysis as light spectra, angle, and surface reflection can influence the mixing index. This means each measurement series must have a reference point identical to all previous tests to get the same result. This additional step means that images must be artificially scaled, and additional runs must be performed.

To address the extended preparation and scaling of data post measurement, relative mixing index (RMI) can be used. [107], [108] By comparing the relative intensity, it is possible to remove an additional step as data can be directly compared. This ratio can be calculated using Equation 1.9.3.

$$RMI = \frac{\sigma}{\sigma_0} = \frac{\sqrt{\frac{1}{N}\sum_{i=1}^{N}(I_i - <I>)^2}}{\sqrt{\frac{1}{N}\sum_{i=1}^{N}(I_{oi} - <I>)^2}} \tag{1.9.3}$$

Where

σ_0 – standard deviation of the pixel intensities in the unmixed case

I_{oi} – local pixel intensity in the unmixed state

It is important to note that the RMI definition is inverse of mixing, thus a 1 – RMI is a more intuitive representation. In this case of 1 – RMI, 0 is unmixed state, and 1 is homogeneously mixed state.

Nevertheless, when measuring mixing using a 2D setup, such as with an optical or fluorescence microscope, the actual mixing profile can be misleading. This is because only the top layer of the fluid is typically observed, making it difficult to accurately

assess contributions from the bottom layers, which are affected by the Beer–Lambert law. This limitation is particularly significant if secondary flow is present; while the top layer may appear fully mixed, the fluid underneath may be slipping or show incomplete mixing. Thus, a 2D image might suggest full mixing, even though the entire volume is not uniformly mixed. This discrepancy underscores the importance of employing 3D analysis techniques for a comprehensive evaluation of mixing efficiency in microfluidic systems.

1.10. 2D and 3D flow characterization

It is often sufficient to acquire a mixing index of two fluids to determine the mixing state of a system. However, in certain cases, understanding the underlying processes involved in the mixing becomes crucial. This deeper understanding is typically achieved through visualization of the fluid or the particles within it. Over the years, various methods have been developed, most of which focus on 2D systems. A comprehensive review has been done by D. Sinton in 2004. [109] where methods such as laser doppler velocimetry [110], particle streak velocimetry [111], Particle image velocimetry (PIV) [112], Micro-PIV [113], Fluorescence [114], [115], photobleaching [116], photochromic reaction [117], phosphorescence [118], caged fluorescence[119] and infrared heating [120] has been explained in detail.

Post 2004 3D flow analysis became more common and available with ever-increasing computing power and improved software. Numerical methods such as Computational Fluid Dynamics (CFD) started to develop quickly and became part of the experiment providing and providing a theoretical baseline that could be compared to the experimental results. Furthermore, with advances in camera technology combined with improved automatic processing, 3D particle tracking has become possible. This has been largely done via PIV where specific polystyrene beads are introduced in the fluid flow and their travel across a fixed time period is measured using an optical or fluorescence camera with a high frame rate. (Figure 1.10.1.)

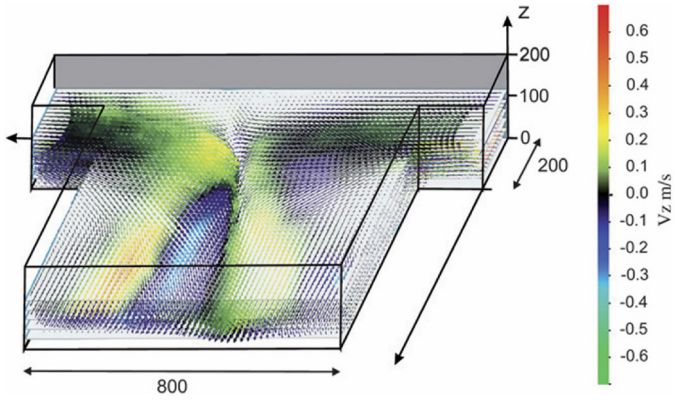

Figure 1.10.1. Three-dimensional reconstruction of the flow field in a T-joint mixer using a stereoscopic micro-PIVat Re = 120. The in-plane velocity distribution is presented as vectors. The z-component of the velocity is represented color-coded. [121] reprinted with permission.

Work done by C. Cierpka and his group has been a progressively advancing PIV and μPIV systems by summarising international PIV challenge results [122] where new and promising approaches to PIV are being discovered. Furthermore, C. Cierpka has been involved in development of astigmatism particle tracking velocimetry, a method that can be effectively used for 3D flow velocimetry due to its simplicity and the ability to deliver precise results. [123]

Even though particle tracking has become a core technology in the microfluidics community its adoption is rather slow, thus less computationally difficult methods such as optical or fluorescence imaging still are present. One such method is confocal microscopy which can acquire an image comprised of multiple layers typically sacked in z direction. This method is often combined with fluorescent dyes, such as Rhodamine B, which emit light upon excitation by a laser. The emitted fluorescence is used to generate a pixel-by-pixel scan of the flow, minimizing overlap and enabling precise measurements. This allows for fine detail and few μm resolution. Notably this method only works due to laminar flow as even though chaotic advection is present it is stable in time as local vortices formation is influence by geometry and starting conditions.

The main downside of fluorescence microscopy is the inability to acquire precise flow vectors, as its possible to do with PIV. Thus, the use case is typically to determine the flow profile and understand the mixing in 3D. An excellent example is Arjun P. publication [124] where confocal and conventional microscopy are used to show the effects of dean vortices in a 2D planar micromixer.

This leads to a fundamental challenge that all visualization methods aim to address: acquiring precise information about fluid flow to understand and optimize processes such as mixing, Dean vortices, chaotic advection, and secondary flow. The goal is to advance knowledge of how to efficiently mix two fluids in a laminar flow setting. This is critical for numerous applications, as nearly every biological assay requires the combination of fluids for detection, separation from clinical samples, or reagent preparation for further analysis. Beyond biological contexts, similar principles apply to mixing oxidizers with fuel for chemical reactions [118] (Figure 1.10.2.).

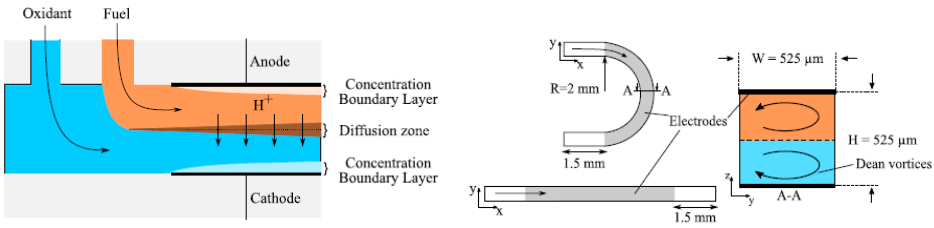

Figure 1.10.2. Influence of dean vortices on a fuel oxidiser cell. [125]

Understanding 2D and 3D flow patterns and tailoring them for specific applications such as the extraction of EVs related to prostate cancer from biological samples holds potential for considerable advancements in cancer diagnostics. This could lead to substantial improvements in early detection methods. In this context, the scope of this dissertation includes the development of a microfluidic device specifically designed for EV separation, facilitating downstream analyses and supporting advancements in early cancer diagnostics.

2. METHODS

2.1. Device design

Device design commenced with abstract concepts tailored to enhance microfluidic functions, such as a passive mixing device featuring multiple zigzag patterns. This concept was subsequently transformed into a digital model using SolidWorks, a 3D CAD software a Computer-Aided Design (CAD) software. Basic geometric operations were executed to assemble the complex shapes required for the designs. The software was not only used for the initial modelling but also for revision based on fabrication constraints and design optimization, resulting in a microfluidics device with similar features as shown in Figure 2.1.1.

Once the 3D model was finalised, it was converted into appropriate file formats tailored for various fabrication technologies. For 3D printing applications, the models were exported in the Stereolithography (STL) format. STL is favoured due to its compatibility with most 3D printers and describes only the surface geometry of a three-dimensional object without any representation of colour, texture, or other common CAD model attributes.

For 2D fabrication processes, such as laser cutting and lithography such as laser writing, the models were converted to drawing exchange format (DXF) files. Although this format strips away the 3D features, it was necessary to facilitate the use of laser cutters and other 2D manufacturing methods. For lithography design development K-Layout was used as it the offers' ability to export files as graphic design system (GDS2) format as well as its ability to manage complex 2D structures which are common for mask fabrication.

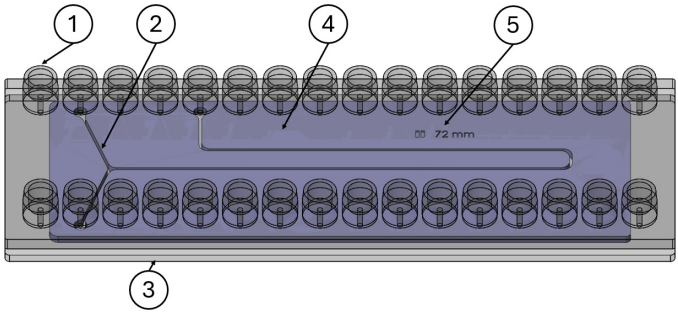

Figure 2.1.1. Microfluidics device made of COC microscopy slide with mini luer connectors (1), 200 µm × 200 µm channel (2), COC microscopy slide (3), OSTE layer (4), and a reference marker (5).

2.2. 3D printing

In this research, double negative moulds were fabricated using 3D printing, with the Zortrax Inkspire printer, featuring a 50 μm pixel size and 50 μm layer height. The resin used was ivory-white, with a Young's modulus of 2 GPa and a shrinkage rate of 4 %. To enhance mould surface quality, moulds were printed directly on the build plate in a planar configuration. This method was chosen to achieve the flattest surface possible, which is a crucial parameter for further bonding procedures. When printing is conducted at an angle, a stair-like pattern is often created on the mould's surface, which can considerably affect the adhesion between injected resin and device substrate reducing the probability of creating an airtight seal.

Furthermore, although surface roughness is minimised through planar printing, a cup-like structure inevitably forms on the mould, potentially leading to bubble formation. These bubbles impair the layer printing process by creating voids. These voids prevent resin from being deposited, hindering polymerisation and resulting in the formation of holes. (Figure 2.2.1.)

Figure 2.2.1. Printed mould without air escape holes, circles indicated defects.

To counter this effect, additional air vents can be incorporated into the design. While crucial for printing, these vents leave open hole in the mould. Thus, post-printing air vents must be sealed with non-leaching materials. The leaching of monomers can present a major issue, as they are present in 3D printer resin and most glues. Leaching monomers are an issue as they inhibit polymer curing, such as PDMS. If leaching monomers are not removed, curable polymers like PDMS will fail to fully cure, even when exposed to curing conditions for considerably longer than the typical curing time. In such cases, the polymer will remain in a permanently tacky or sticky state. This means that polymers surface is not well-defined and cannot be used. To address this, a solution has been implemented: a post-curing thermal bake for at least 48 hours at 60 °C, which effectively removes the leaching monomers.

While 3D printing offers unparalleled flexibility and customisation in prototype development, the shift towards traditional injection moulding could provide the scalability and cost-efficiency required to transition a prototype into a marketable.

2.3. Microfabrication

For mask fabrication a standard lithography process was used. The initial design was made in Solidworks, after which it was converted into GDS2 file via the K-layout software.

2.3.1. Sample pretreatment

To proceed with the fabrication a glass substrate was prepared. A 76 × 25 mm glass slide was mechanically cleaned using 100 % Polyester napkins soaked in acetone after which this step was repeated with 100 % Polyester napkins soaked in isopropanol (IPA). Post-mechanical cleaning glass slides were placed in an ultrasonic bath in a Glass Staining Jar with:

1. Acetone at power 70 % and frequency 37 kHz for 15 min.
2. DIW at power 70 % and frequency 37 kHz for 2 min.
3. Detergent at power 70 % and frequency 37 kHz for 25 min.
4. DIW at power 70 % and frequency 37 kHz for 15 min.
5. IPA at power 70 % and frequency 37 kHz for 15 min.

2.3.2. Physical vapor deposition

After ultrasonication samples were blow-dried using N_2. After this process glass slides were visually inspected for defects and residue spots. Next cleaned slides were prepared for thermal evaporation. To improve adhesion and remove organic residue, glass slides were treated with O_2 plasma for 300s at 800W at 1000 sccm O_2, in a GHz frequency plasma asher. Post plasma treatment slides were ready for thermal evaporation where 3 nm of Cr was deposited at a rate of 0.03–0.06 nm, and 200 nm of Al was deposited at a rate of 0.3 nm/s in pressure not higher than 2×10^{-5} mBar. (Edwards – Auto 306)

2.3.3. Spin coating

Post thermal evaporation the glass slides with 3 nm Cr and 200 nm Al were primed using hexamethyldisilizane (HMDS) to improve resist surface adhesion and to remove surface moisture. (YES-310TAE). Post surface treatment AZ1518 was spin coated on the substrate using 500 RPM for 5 s with an acceleration of 500 RPM/s and 4000 RPM for 30 s with an acceleration of 1750 RPM/s. The initial 500 RPM step is used to better spread the resist as due to the asymmetry of the glass slides as even layer acquisition is difficult. To evaporate the residual solvent a soft bake at 100 °C for 180 s was performed after spin coating.

2.3.4. Direct laser writing

AZ1518 (MicroChemicals) is a positive photoresist, meaning that upon exposure to UV light, it becomes soluble in the developer solution. This solubility allows for a selective dissolution of the exposed regions, enabling the creation of precise patterns

on the resist layer. The patterning process was performed using direct laser writing (Heidelberg μPG 101, 375 nm wavelength), with an exposure dose of 97.4 mJ. [126]

2.3.5. Development

The samples were developed in AZ726 developer for 50 seconds at 20 °C. During this process, the exposed regions of the photoresist, which had become soluble due to UV exposure, were selectively dissolved by the developer. To halt the development process and prevent overdevelopment, the glass slides were immediately immersed in deionised water (DIW) to remove any remaining developer. The slides were then dried using nitrogen (N_2) to remove DIW and any leftover residue. Following the development, the samples underwent a hard bake at 130 °C for 5 minutes. This post-exposure bake further stabilised the photoresist, making it more resistant to subsequent processing steps. As a result, the photoresist becomes highly resistant to the developer, allowing for the continuation of etching processes.

2.3.6. Etching

The aluminum layer was etched using AZ 726 at 60 °C for a duration of 45 to 90 seconds. The etching time was increased to 180s when instead of HMDS surface layer Ti Prime was used. After etching, the samples were rinsed in DIW to remove any residual etchant. The undeveloped AZ1518 photoresist was then dissolved by immersing the samples in an acetone bath for 10 minutes, avoiding ultrasonication to prevent potential damage to the patterns. Following this, the samples were cleaned in isopropanol for 10 minutes and subsequently dried using N_2.

2.3.7. Atomic layer deposition (ALD)

An Al_2O_3 layer was deposited on the metallised side of the sample using an Atomic Layer Deposition (ALD) process. Trimethylaluminum (TMA) and H_2O were employed as precursors, with the deposition carried out over 500 cycles at a chamber temperature of 150 °C. This process resulted in the formation of a 50 nm thick Al_2O_3 layer.

2.4. Measurement methods

To evaluate device performance multiple methods were used, including optical absorption, confocal fluorescence, Western Blot and quantitative polymerase chain reaction (QPCR).

2.4.1. Mixing efficiency

To evaluate the mixing performance of different microfluidic devices, a custom mixing system was developed. This setup included a syringe pump to maintain consistent and precise flow control. Connections between the syringe pump, microfluidic device, and waste container were facilitated using 800 μm PTFE tubing

(Darwin Microfluidics). Mixing was quantified using Rhodamine B (≥ 95 %, Sigma-Aldrich) dissolved in deionized water (DIW) at a concentration of 1 mM, and DIW. At the end of the mixing module, an optical microscope (Nikon, Eclipse LV150N) equipped with an integrated camera (DS-Fi3, CMOS 2880 × 2048 pixels) was used for image acquisition. A desktop computer was then used to capture and analyse the results, as shown in Figure 2.4.1.1.

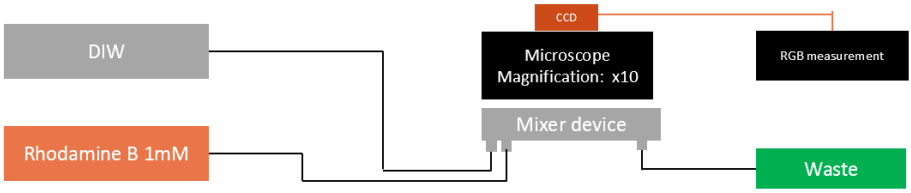

Figure 2.4.1.1. Schematic of mixing measurements.

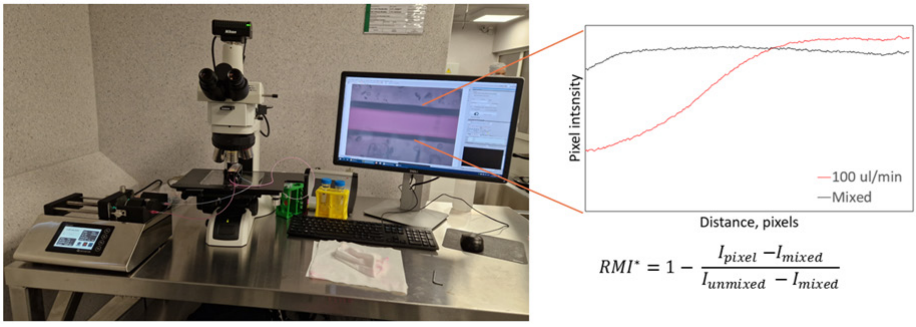

Figure 2.4.1.2. Photograph of mixing setup on the left and mixing data example on the right, where x axis is the channel width. all Values are integrated across channel length, and mixing value are taken at a constant flow rate whereas mixed value is after flow has stopped for 5 minutes.

To evaluate different designs, aqueous solution of rhodamine B and DIW were injected at the start of the mixing device at a specific flow rate. The optical measurement was taken at the end of the device at specific flow rate after steady state flow had been achieved. The background reference was channel with DIW, and fully mixed state was acquired by stopping the flow post mixing value acquisition and wating for 5 minutes thus fully diffusing the rhodamine B in DIW. The pixel values were averaged horizontally across the channel and measured over the entire channel width (indicated as distance in pixels, vertically), as shown in Figure 2.4.1.2. The mixing efficiency was quantified using the relative mixing index, a method previously reported by Ali Hashmi and Jei Xu in 2014 [105] and detailed in Section 1.9 of the literature review.

Each device channel was tested at varying flow rates, with images captured while the flow was continuous. The initial unmixed state (I_{unmixed}) was taken as 0, using an empty channel filled with DIW as the reference. The value $\langle I \rangle$ was obtained after 5 minutes of diffusion inside the channel in the absence of flow. This allowed for

an evaluation of the relative mixing index, which was used to compare different device designs and flow parameters.

Different design and flow parameters were quantified using a correlation matrix, which quantifies the strength and direction of a linear relationship between two numeric variables. This task was done using R software (readxl, ggplot2, tidyverse, ltm,Hmisc, corrplot) where Hmisc package was used to generate correlation matrix and corrplot was used to visualise it. To determine p values cor.mtest function was used with a confidence interval of 95 %.

2.4.2. Confocal microscopy

Flow visualisation was conducted using a confocal laser scanning microscope (Leica TCS SP8). Fluorescence imaging was performed with DIW and rhodamine B as fluorescent dye. Excitation of the rhodamine B was achieved with a 561 nm diode-pumped solid-state (DPSS) laser, and emission was detected in the 570–600 nm range. Imaging performed using a 10x objective lens with a numerical aperture (n.a.) of 0.30. Z-stacks were acquired with a 5 µm step size to capture the three-dimensional structure of the flow within the microfluidic channels. This technique was chosen due to its capability to provide high-resolution images and detailed insights into the flow dynamics and mixing processes. The experimental setup, including the flow conditions and microfluidic device, is illustrated in Figure 2.4.2.

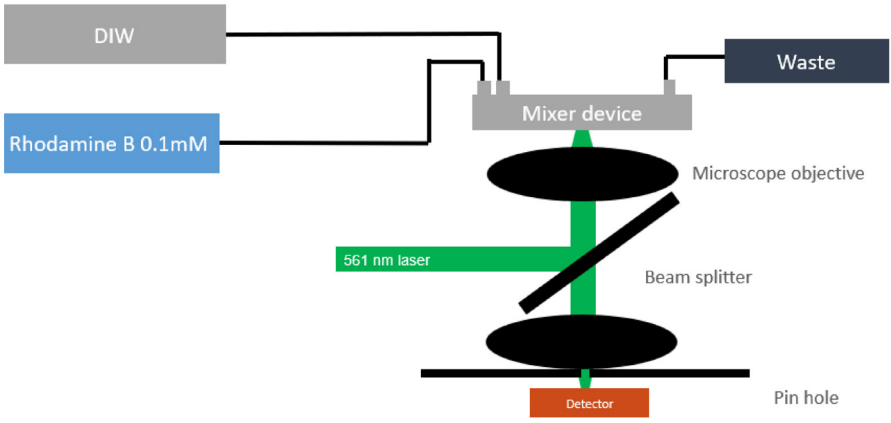

Figure 2.4.2. Schematic of confocal microscope

2.4.3. MP quantification

Iron concentration was determined by absorbance measurement of dissolved magnetic particles. MPs were subjected to experimental conditions, and outflow was captured before and after removing the magnet. Thus, all MPs were captured, and analysis could be carried out.

All conditions were performed in triplicate to improve measurement accuracy. A 50 µL aliquot of each sample was pipetted into individual tubes. The samples were

then dissolved by adding 100 µL of freshly prepared aqua regia (12 ml 35 % HCl and 3 ml of 65 % HNO_3) in a fume hood, followed by heating at 60 °C for 15 minutes using a thermoblock. Post-heating the reactions were quenched by adding 350 µL of Milli-Q water.

Subsequently, 50 µL of the dissolved sample was transferred to a 96-well plate. A freshly prepared solution of 0.25 M Tiron (4,5-Dihydroxy-1,3-benzenedisulfonic acid disodium salt monohydrate; MW = 332.22 g/mol) was mixed with 4 M KOH (1.4 mL Tiron with 7 mL KOH) and 60 µL of Tiron/KOH mixture was added to each well using a multi-channel pipette. Following this, 100 µL of 0.2 M sodium phosphate buffer (pH 9.7) was added to each well and mixed thoroughly by pipetting. The absorbance of each well was measured at 480 nm using a plate reader.

To quantify each sample's magnetic content, a calibration curve with known iron quantities is created in parallel on the same 96 well plate and used as a calibration curve.

2.4.4. Western blot

Western blot analysis was employed to separate and detect specific proteins, such as CD9 and CD63, from biological samples based on their molecular weight and charge. The fundamental concept underlying this technique is that the charge of a protein is proportional to its mass, enabling separation in an electrical field. Furthermore, to use western blot the analyte or EVs must be combined with an antibody, thus providing the method's specificity. This is often done in 2 steps: first, to capture the specific antibody, in our case CD9, and extract it from the rest of the sample. And second, to detect an analyte or EV with a specific antibody marked with a luminescent tag. The western blotting happens in 4 step process (Figure 2.4.4.1):

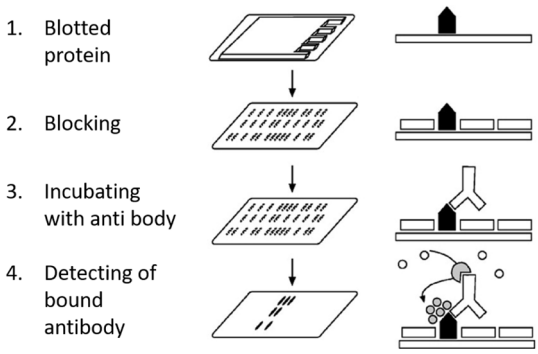

Figure 2.4.4.1. Western blot schematic. [127]

For experiments in this research the western blot was performed using 10 µL of lysate in a 7-step process:

1) Laemmli was loaded per each lane of a 10 % SDS-PAGE gel.
2) Electrical separation was carried out at 150V.

3) Proteins were transferred onto 0.45 µm nitrocellulose membranes, which were subsequently blocked using 10 % (w/v) fat-free milk for 1 hour at room temperature.
4) The membranes were then incubated with primary antibody overnight at +4 °C with agitation and washed 4 times with TBS+Tween-20.
5) The incubation with secondary antibody was done for 1 h at room temperature with agitation, followed by washing as mentioned previously.
6) Detection of immunoreactive bands was carried out using the Amersham™ ECL Select™ Western Blotting Detection Reagent kit (GE HealthCare) and pictures were taken using a Nikon d610 dSLR body (Nikon) with Sigma 35 mm f/1.4 DG HSM Art lens (Sigma).
7) To acquire numerical band-integrated density values, ImageJ software was used.

When necessary, the membrane was stripped in a buffer containing 1.5 % glycine, 0.1 % SDS, 1 % Tween-20, pH 2.2, blocked again, and re-probed with a different set of antibodies as used previously.

Using the method described above the expected result is shows in Figure 2.4.4.2, where a generic CD9 capture, and detection is displayed where the left image shows luminescence that is caused by HRP, and the right image is an inverted image with added ladder.

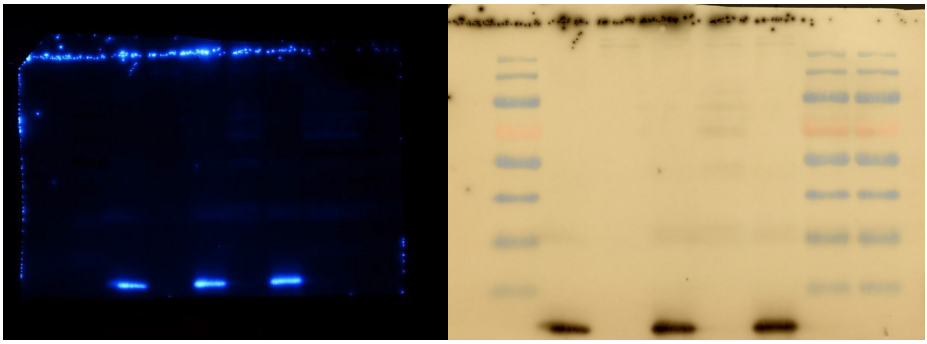

Figure 2.4.4.2. Generic western blot result, left image observed by a camera and right image that has been inverted.

While WB analysis is typically not used for quantitative analysis it can still be quantitative by correct and consistent data analysis, as well as by placing all samples on a single membrane. This is due to differences based on light emission positions etc. and protein inherent inconsistency. Thus, a single membrane must be used for a quantitative approach, which limits the sample count to 14 including controls. This is a major limitation for high data count and multiple condition comparison. This issue can be addressed by using an identical control on each membrane, but this is still subject to inherent biological differences even for the same sample. An alternative method to detect protein count and perform quantitative analysis is Quantitative Polymerase Chain Reaction (qPCR).

2.4.5. Quantitative Polymerase Chain Reaction (qPCR)

qPCR is a powerful technique for quantifying the expression levels of specific genes, enabling the detection and quantification of DNA sequences in real-time through the amplification of target sequences. Before proceeding with qPCR, RNA must be extracted from the sample. In the scope if this thesis, post-capture MPs with surface-bound EVs were treated with QIAzol lysis solution to disrupt the lipid bilayer membrane and release the RNA.

Given that qPCR is a quantitative method, the reference marker UniSp6 was employed for normalisation. Further sample preparation involved RNA extraction using the miRNeasy Micro Kit (Qiagen). The extracted RNA was then reverse transcribed into complementary DNA (cDNA) using the miRCURY LNA RT Kit (Qiagen). Following the completion of sample preparation, qPCR was performed.

Each PCR cycle begins with the denaturation of the double-stranded DNA in the target region, referred to as the amplicon. During the annealing step, primers bind to their complementary sequences flanking the region of interest on each DNA strand. This is followed by the extension step, where the polymerase enzyme synthesises new DNA strands by extending from the primers. The SYBR Green dye, which specifically binds to double-stranded DNA, emits a fluorescent signal that is directly proportional to the amount of DNA present, allowing for real-time quantification (Figure 2.4.5.1).

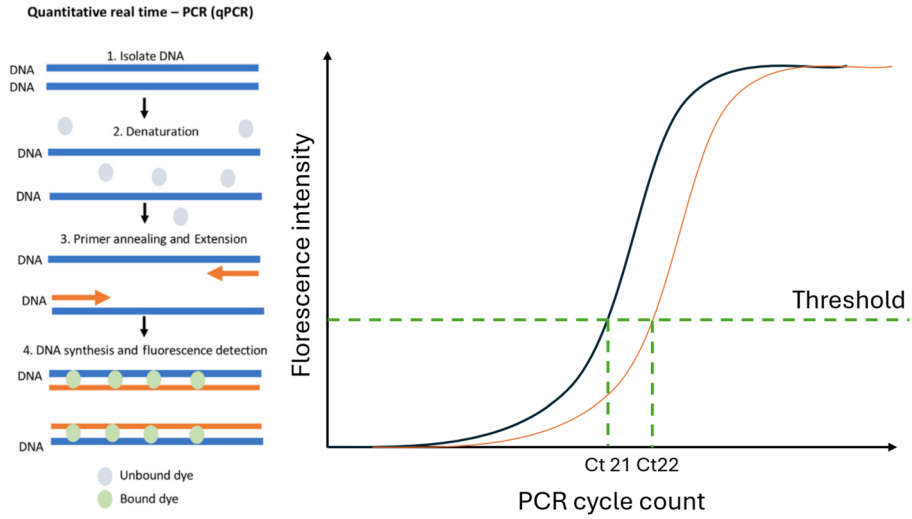

Figure 2.4.5.1. Schematic of qPCR, and example of qPCR data. [128]

To evaluate the data, a threshold value is established by selecting a point within the middle of the S-curve, which represents the cycle at which the fluorescence signal surpasses the background level. This threshold cycle (Ct) is then used to determine the relative protein count, as each qPCR cycle results in a doubling of the target DNA, reflecting an exponential increase in the protein count.

Subsequently, the expression levels of MiR-375 were normalised in two steps: first, against the reference marker UniSp6, and then against the total amount of captured MPs, which was quantified based on their iron content. This dual normalisation ensures that the data accurately reflects the relative abundance of MiR-375 in relation to the reference marker and the number of MPs.

3. FABRICATION

The first thing required for a microfluidic device is the device itself. This can be accomplished in numerous ways, each with its own benefits and disadvantages as detailed in the literature review section. In scope of this dissertation all devices were fabricated using reaction injection moulding. A method similar to injection moulding but the material solidification is accomplished via UV irradiation that drives the subsequent polymerisation. This reaction is exothermic thus heat is an additional factor influencing the polymerisation process.

3.1. OSTE 322 reaction injection moulding

Reaction injection moulding requires a precisely fabricated mold, which in this case was produced using a 3D printer with ivory-white resin. A key limitation of this method is resolution, which is constrained not only by the printer's pixel size but also by mechanical factors such as vibrations and layer-to-layer positioning accuracy. In herein described printer layer positioning could vary up to 200 µm, as seen in Figure 3.1.1.

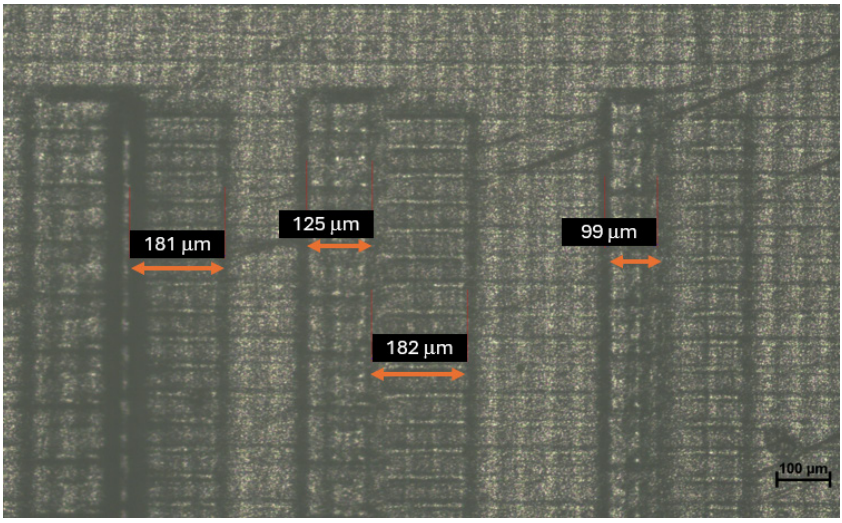

Figure 3.1.1. A test piece for a 3D resin printer showing layer-to-layer alignment error.

The printer's precision defined the minimal achievable channel size of around 300 µm. A notable observation is that the precision for trenches is less accurate compared to protrusions. This occurs because if a layer misaligns, a trench may get partially covered or closed, whereas a protruding feature can only build up if a previous layer exists underneath it, thereby improving resolution. This principle was used to enhance the mould design, where all channels were structured sequentially. This

approach improved the mould in two ways: it reduced the formation of air bubbles during filling and ensured the design was hill-based. (See Figure 3.1.2.).

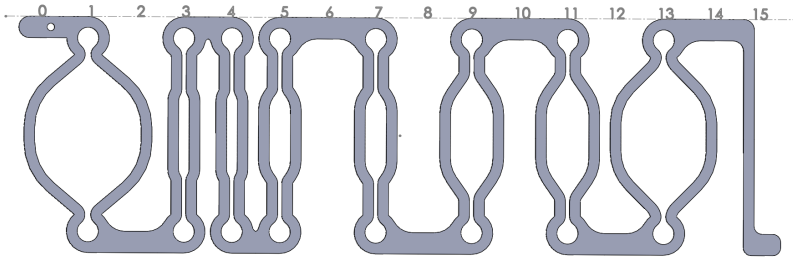

Figure 3.1.2. Magnetic capture design, the dark line indicates the OSTE flow lines.

An additional issue encountered during the printing process was bubble formation, caused by the "cup" effect when the mold was printed on a flat plane to reduce surface roughness. To address this, 50 µm and 3 mm holes were introduced inside the mould to allow air to exit and enter, preventing the formation of a vacuum. Moreover, the sequential design ensured that a hole in the centre did not carry over to subsequent moulds. This solution is depicted in Figure 3.1.3.

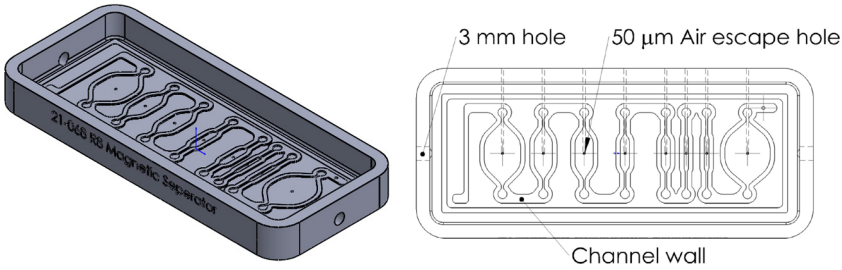

Figure 3.1.3. Magnetic capture design mould with added air escape holes for bubble reduction. Isometric on the left and top view on the right.

After printing the mould, it was cleaned using isopropanol and subsequently cured with UV light (810 s). Post UV-cure mould was thermally treated at 60 °C for 48 h to remove leaching monomers.

After thermal treatment, the mould was filled with a 2-component silicone (SORTA-Clear™) and degassed until all bubbles were removed. Sorta clear silicon was chosen as (SYLGARD™ 184) had higher affinity to OSTE thus a lower cure dose could be used and subsequently a stronger adhesion between OSTE and COC slide could be achieved. Post-degassing mould was placed in an aluminum jig to ensure flat surface and allow for mould compression. The mould was capped with a PET film to ensure low surface roughness, easy application and easy disassembly. Post capping the mould, a PMMA plate was placed on top and tightened with 6 M4 screws as shown in Figure 3.1.4.

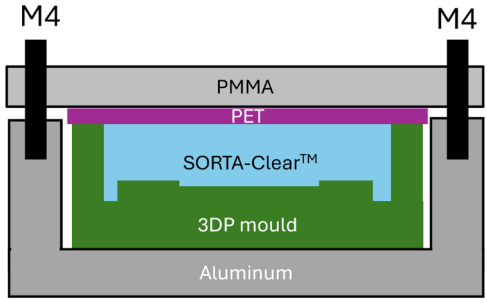

Figure 3.1.4. Side view schematic of jig for silicon mould fabrication. (not in scale)

Post-compression mould was thermally cured for 3 h at 60 °C. After thermal cure mould was disassembled and the silicon was removed from the mould using isopropanol to aid removal. After which, the silicone mould was N_2 blow-dried.

Magnetic capture device fabrication starts with mixing OSTE322 A and B components at a 1 : 1.09 ratio. Mixing was facilitated using a planetary mixer (Mixer ARE 250, Thinky Corporation) by mixing at 750 RPM for 300 s in the mixing regime and, 750 RPM 300 s in the defoaming regime. Mixing was followed by vacuum desiccation to remove bubbles formed due to mixing and pouring of liquids.

While mixing, OSTE glass slides were prepared as outlined in Section 2.3.1. with the final step of surface O_2 plasma treatment (300 s at 800 W and 1000 sccm O_2) (GIGAbatch 360M, PVA TePla AG)

After plasma treatment, the glass slide was fitted in the silicon mould (SORTA-ClearTM) and placed in an aluminium jig. An additional PMMA plate was placed between the mold and the aluminum jig to function as a UV absorber. This addition was necessary because aluminum reflects UV light, which affects the curing dose of the OSTE polymer. The COC slide was capped with a 2 mm thick glass plate which was held by 3D printed resin (Zortrax, Tough Clear) clamps and tightened with 6 M4 screws. After tightening, the jig was ready for injection of mixed OSTE 322 polymer as indicated in Figure 3.1.5.

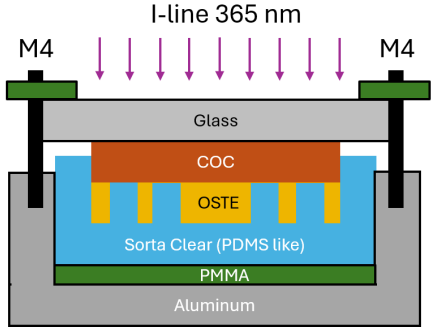

Figure 3.1.5. Side view schematic of jig for OSTE322 injection moulding. (not in scale)

OSTE injection was performed using a pressure system (OB1 MK3+, Elveflow) using a 1.5 ml Eppendorf tube at a pressure of 600 mBar (Eppendorf). Although running at maximum pressure would minimize device production time, 600 mBar was selected as the optimal setting because higher pressures led to leakage of the OSTE material via the PDMS-COC compression areas

After OSTE injection, the device was exposed with UV light with a dose of 850 mJ/cm^2, using an ND33 filter to reduce the exposure rate. Following UV curing, the glass slide containing the structured OSTE was carefully peeled away from the silicon mould. The other side of the device consisted of a COC slide with 32 mini-Luer ports (Microfluidic Chip Shop), which had been treated with O_2 plasma for 120 seconds at 700 W in an 800 sccm O_2 atmosphere. Subsequently, the two halves of the device were manually aligned and brought into contact. The assembled device was then pressed together and subjected to an overnight cure at 65 °C for approximately 18 hours. The finished device can be seen in Figure 3.1.6.

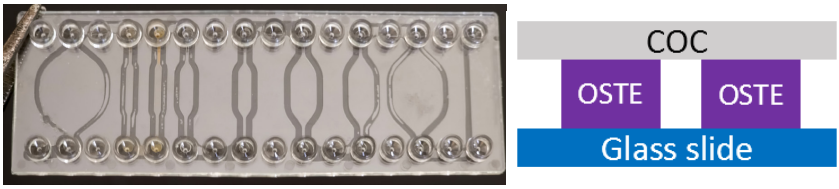

Figure 3.1.6. Finished OSTE 322 device on the left and the side view of the device on the right.

Using the described procedure, a batch of 5 devices was fabricated, yielding a total of 40 channels. Of these, only a single channel failed, resulting in a success rate of 97.5 %. This high success rate indicates that the fabrication process is robust and well-optimized, making it suitable for small-scale production.

3.2. OSTE 220 reaction injection moulding

An issue arises when applying OSTE 322 fabrication method to micromixers. The maximum resolution achievable is in region of few hundred microns thus sharp corners are impossible. Furthermore, due to the moulding process it is impossible to create obstacles inside the channel which could aid mixing. Due to these constraints, an alternative fabrication method was developed based on the OSTE 220 example.

The silicone moulding process is similar to one detailed in Section 3.1, but QSil 216 (CHT) was chosen as the moulding material. QSil 216, a PDMS-like substance, combines the advantageous properties of both SYLGARD184 and Sorta Clear. Sorta Clear is preferred over SYLGARD184 due to its reduced stickiness to OSTE, which aids in demoulding. However, it tends to partially cure during bubble removal, complicating handling. QSil 216 on the other hand maintaining the non-stick quality of Sorta Clear but cures similarly to SYLGARD184. This dual advantage allows for easier handling and results in more consistent high-quality moulds.

The steps in creating OSTE 220 device are similar to process for OSTE 322 detailed above yet there are key differences specifically in the curing procedure of OSTE 220. While OSTE 322 contains a reagent that has epoxy groups, leading the material to fully polymerize via an additional heating step, OSTE 220 does not contain a reagent with epoxy groups, thus can be cured in a single step via UV light.

The process starts with the fabrication of Cr-Al mask as detailed in Section 2.3 where a 3 nm Cr layer and a 200 nm Al layer are thermally deposited on a glass substrate and the design is etched. After mask had been fabricated OSTE 220 A and B components were mixed in a ratio of 1 : 1.86 using a planetary mixer at 750 RPM for 300 s in mixing regime and, 750 RPM 300 s in the defoaming regime. After mixing OSTE was vacuum desiccated for 5 minutes.

For OSTE devices COC slide is used instead of glass as it offers better adhesion to OSTE channel side walls. The surface treatment is similar (300 s at 700 W and 1000 sccm O_2, GIGAbatch 360M, PVA TePla AG). Post-surface treatment COC slide, mask, and mould is stacked and clamped together using 6 M4 screws as shown in Figure 3.2.1.

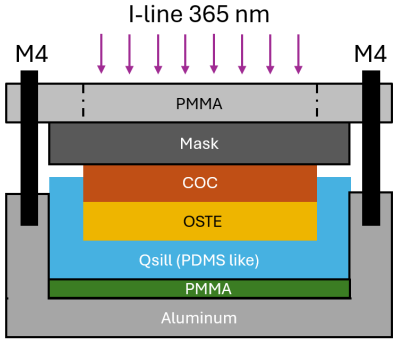

Figure 3.2.1. OSTE 220 jigs side view schematic (not in scale), where dash dot lines respresent a cut, and mask is not covered by PMMA plate.

For OSTE 220 processing, the PMMA spacer between the mold and the aluminum jig is crucial. This spacer prevents UV light reflected from the aluminum jig from curing the polymer in unintended areas. Since the design is defined by a UV mask that blocks light, any unintended exposure can compromise the process by curing areas that should remain uncured. This issue is particularly significant for OSTE 220 due to its lower UV exposure dose requirements, which are an order of magnitude less than those for OSTE 322.

Additionally, a notable requirement is the increased requirement for precise tightening. This was done using a torque wrench at 0.3N force. For sub-0.3 Nm torque adjustment, a procedure was developed: all six screws were initially tightened to 0.3 N, then each screw was adjusted by a specified angle to fine-tune the tightening. Specifically, a full rotation back was used for the screws along the long axis of the device, while a quarter rotation was applied to the four middle screws, as shown in Figure 3.2.3.

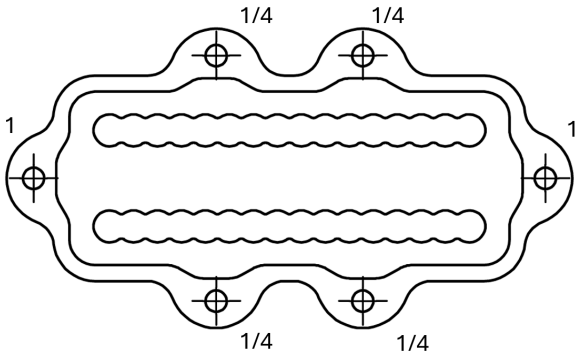

Figure 3.2.3. Aluminum jig, and the respective screw untightening, noted as a value of full rotation.

The filling of OSTE 220 (Mercene Labs, Ostemer) was done at 800 mBar using a 1.5 ml tube (Eppendorf) and Elveflow pressure system. Post filling, the stack was exposed with collimated UV light (MA/BA6 Gen4, Suss Microtec) using ND33 and I-line filter to reduce the exposure rate to 6 mW/cm^{2}s with the final dose of 50 mJ/cm^2. The post exposure device was carefully removed from the mould.

After exposure, the device was developed in acetone in an ultrasonic bath (Elmasonic P, 80 kHz, 50 %), for 75 seconds, where the reaction was subsequently stopped by isopropanol and N_2 blow-dried. Post-development bake was performed at 60 °C for 3 min to reduce mechanical stress and allow for better layer bonding. Before bonding the top part of the device, the COC slide was treated with O_2 plasma (700 sccm O_2, 700 W, 3 min)

Finally, both layers were aligned, clamped together in a jig, and exposed with 4000 mJ/cm^2 dose. Subsequently, the device was cooled down for a few minutes resulting in a hermetically sealed device, with a burst point exceeding 400 µl/min as seen in Figure 3.2.4.

Figure 3.2.4. Finished device on the left and the side view of the device on the right.

4. RESULTS AND DISCUSSION

4.1. Mixer evaluation with optical microscopy

To evaluate the mixing performance of the fabricated OSTE-COC device, the angle between turns was varied from 14 to 22.5 degrees. For all channel the mixing region was 72 mm long and had 12 sharp corners after 2 fluids were connected, with only the connection angle being varied as seen in Figure 4.1.1. This ensured that devices were as similar as possible and objective results could be obtained. To evaluate the influence of the channel size, 2 different width channels were tested 200 µm and 300 µm.

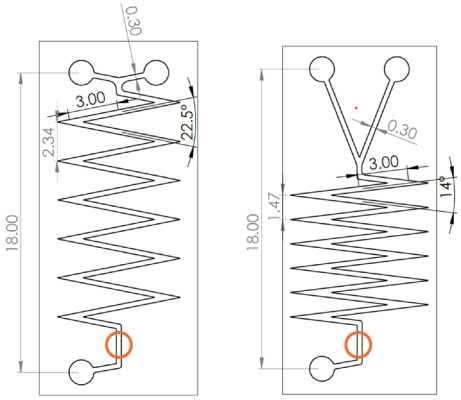

Figure 4.1.1. Device geometry, 2 extreme designs: 22.5 degrees and 14 degrees. The orange circle indicates the mixing index measurement spot.

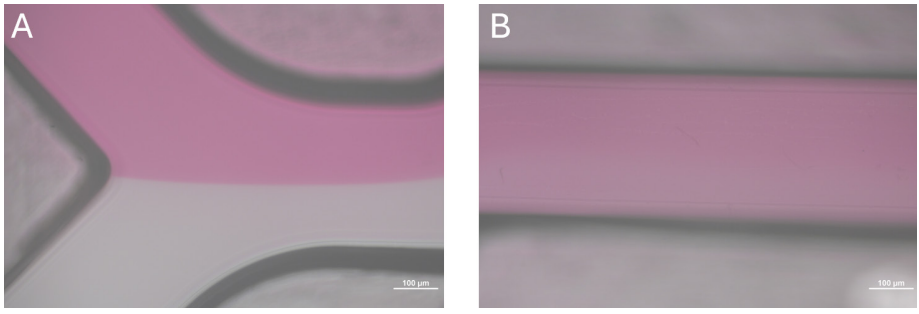

Figure 4.1.2. LM46 microfldics device with zig zag angle of 19.6 degrees. Testing was done with rhodamineB and DIW with a flow rate of 200 µl/min, at the start of the channel (A) and at the end (B).

Mixer evaluation was done with optical microscope (Nikon, Eclipse LV150N) with an integrated camera (DS-Fi3, CMOS 2880 × 2048 pixels) and a desktop computer

as detailed in Section 2.4.1. Figure 4.1.2 shows a typical optical image at the start of the channel (A) and at the end of the channel (B).

Images like Figure 4.1.2 were acquired for 18 different channels spanning 3 devices acquiring a total data set of 57 values. Post image acquisition RMI was calcuated by ploting the values from end of the channel image as displayed in Figure 4.1.3 following protocol outlined in Section 2.4.1.

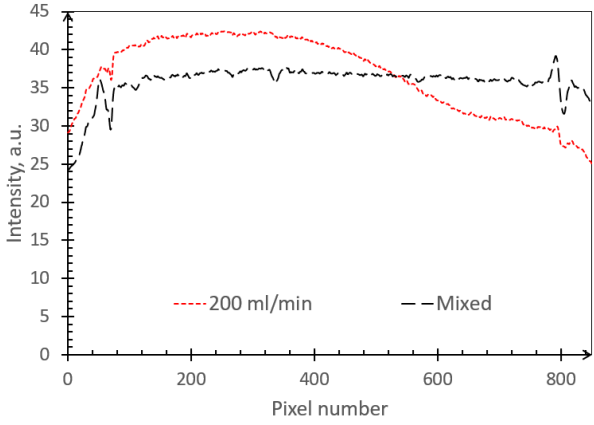

Figure 4.1.3. Example of LM46 SC 5 mixing performance where RMI is 0.87. The pixel number represents the unscaled channel width, while the channel with DIW was used as a subtracted background

Using the acquired mixing index value the repeatbility of the experiment was assesed Figure 4.1.4.

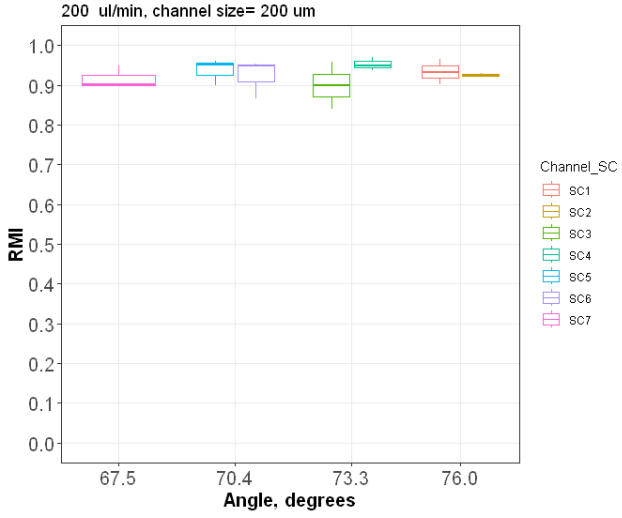

Figure 4.1.4. RMI with respect to device angle with a channel width of 200 μm.

Figure 4.1.4. illustrates that varying angles have minimal impact on the device's mixing performance. Additionally, the box and whisker plots reveal a small standard deviation across all three devices, indicating reliable fabrication and consistent experimental procedures. To further evaluate device compatibility, the RMI was plotted without considering the angle, as depicted in Figure 4.1.5. The overlapping distributions in this data confirm that the devices exhibit repeatable and reliable performance. This overlap underscores consistent mixing properties, which affirms the reproducibility of the devices across comparable experimental conditions.

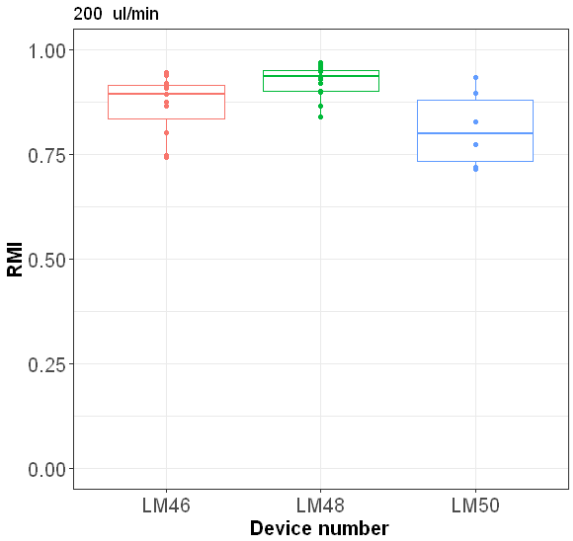

Figure 4.1.5. RMI with respect to different devices data including all angles at 200 µl/min.

To perform statistical analysis R software with packages: (readxl, ggplot2, tidyverse, ltm, Hmisc, corrplot) were used. Hmisc package was used to generate a correlation matrix and corrplot was used to visualize it. To determine p values cor.mtest function was used in confidence interval 95 %. For the calculation of numerical values, a custom script was written, which included performing an ANOVA test to examine linear relationships using the Pearson correlation coefficient. The Pearson correlation coefficient quantifies the strength and direction of the linear relationship between two variables. It ranges from –1 to 1, where a value of 1 indicates a perfect positive correlation, –1 denotes a perfect negative correlation, and 0 signifies no correlation. The associated p-value was used to assess the statistical significance of the relationships. The analysis was performed to compare the following variables: flow rate, channel size, angle, and the RMI, as shown in Figure 4.1.6.

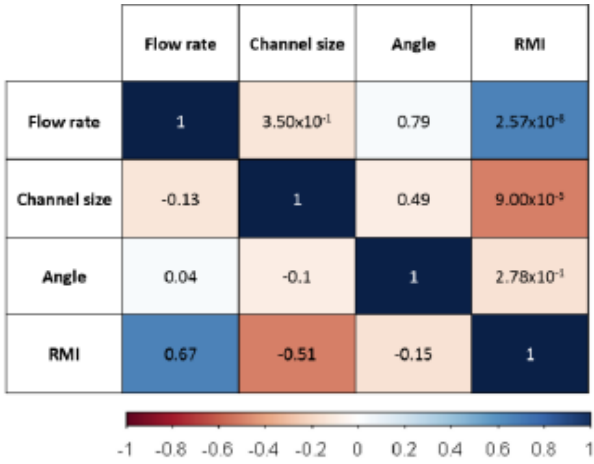

Figure 4.1.6. The correlation matrix of relative mixing index for mixing devices, calculated by Pearson correlation coefficient, where above middle diagonal represents p-value of the correlation coefficient.

The correlation matrix (Figure 4.1.6.) demonstrates a strong relationship between increased flow rate and improved mixing efficiency (r = 0.67) that is significant ($p = 2.57 \times 10^{-8}$), indicating that higher speeds in a passive micromixer led to better mixing. Additionally, reducing the channel size from 300 μm to 200 μm resulted in a statistically significant ($p = 9 \times 10^{-5}$) improvement in the relative mixing index (r = –0.51), likely due to enhanced local chaotic flow, including Dean vortices and secondary flow generated at the mixer's sharp bends. [129] Interestingly, no significant impact was observed for bend angle from 22.5 to 14 degrees (r = 0.04, p = 0.278), with the analysis performed at a 95 % confidence interval, which aligns with findings from Cosentino et al. [130]

For optimal mixing, it is recommended to maximise efficiency by reducing the channel size to 200 × 200 μm and increasing the flow rate. Further reductions in channel dimensions would lead to higher pressure drops in the device and an increased risk of clogging due to the accumulation of cell debris during the separation process. Nevertheless, these results stem from the assumption that 2D optical microscopy can be used to fully determine mixing process for a microfluids device. The issue with this assumption is that channels have depth and non-ideally straight walls due to the fabrication process, this leads to potential 3D effects which are missed.

4.2. Mixer evaluation using confocal microscopy.

Optical microscopy is a good and relatively simple way to determine mixing index, yet it is possible to miss fine details due to the inability to capture flow profile deeper in the channel. To address this uncertainty confocal fluorescence microscopy was employed. First to compare both methods an identical test was performed, by using

300 µm wide and 200 µm high OSTE COC device, and measuring the same location as indicated by Figure 4.2.1.

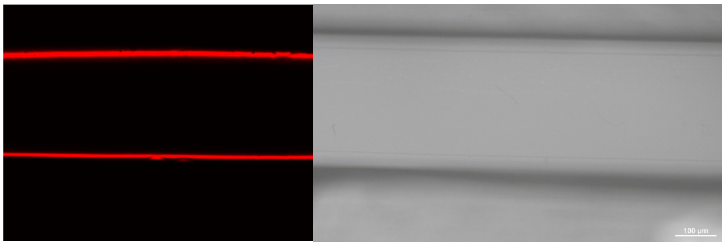

Figure 4.2.1. DIW inside microfluidics channel, (Device LM46, angle = 19.6 degrees). Confocal microscopy image on the left and optical microscopy image on the right.

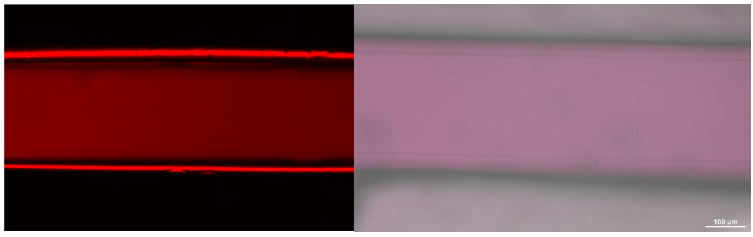

Figure 4.2.2. Fully mixed DIW and rhodamine B inside the microfluidics channel 5 minutes after the flow has been stopped (Device LM46, angle = 19.6 degrees). Confocal microscopy image on the left and optical microscopy image on the right.

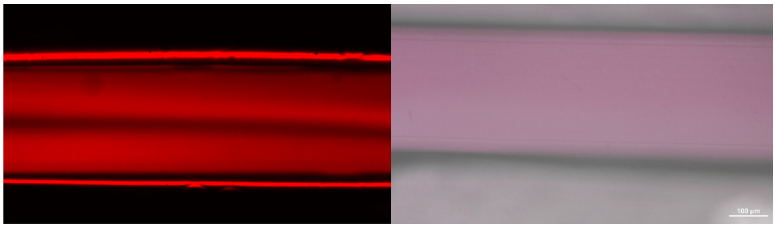

Figure 4.2.3. DIW and rhodamine B inside microfluidics channel with a flow of 200 µl/min (Device LM46, angle = 19.6 degrees). Confocal microscopy image on the left and optical microscopy image on the right.

By comparing the relative mixing index confocal fluorescence microscopy yields RMI = 0.81 while the optical method yields RMI = 0.87. This indicates that both methods produce similar results (Figure 4.2.1.–4.2.3.). The confocal microscopy focus was at the channel's top, where optical microscopy received most of the signal. This was an experimental issue as it is rather difficult to precisely determine the channel

dimensions and focus just at the top of the flow. This is partly the reason a different result is observed.

Having established similarity of both methods the 3D flow profile could be evaluated. This was done by scanning the z axis with a 5 µm step using confocal fluorescence microscope (Leica TCS SP8).

4.3. Initial 3D observation

By 3D scanning with a 5 µm layer step using a 561 nm DPSS laser, thus exciting rhodamine B at the same measurement spot (Figure 4.3.1.) and detecting the emissions in the range of 570–600 nm it was possible to acquire a 3D flow image. (Figure 4.3.2.). Acquiring an image under continuous flow conditions is feasible because the flow remains in a laminar state, meaning its characteristics are consistent over time. This stability allows for prolonged measurements, lasting several minutes, without significant smearing or motion blur. The microfluidic flow analysis was focused on the sharp bend within the mixing unit, where the fluid dynamics, such as vortices and flow separation, were observed.

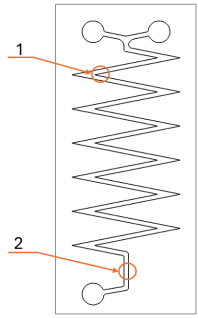

Figure 4.3.1. 3D scan measurement locations.

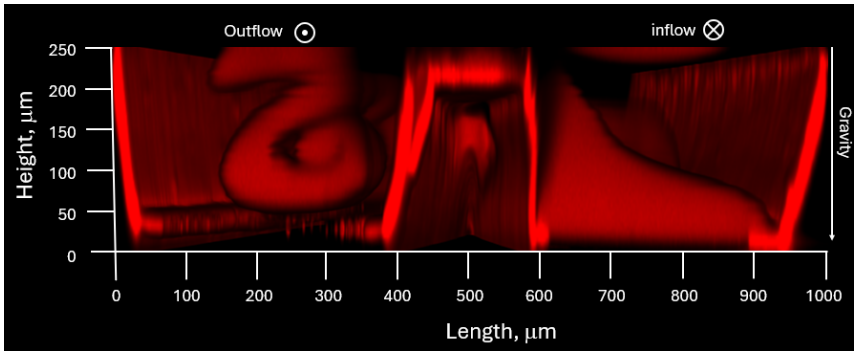

Figure 4.3.2. Confocal microscope image of rhodamine B and DIW mixing at the first sharp bend (Figure 4.3.1 location 1).

The sharp bend in the microfluidic device is known to generate local vortices, likely due to mechanisms similar to those observed in convergent-divergent flows. In this setup, DIW and Rhodamine B traverse paths of varying lengths, which compels the fluids to move across one another, inducing vortices and enhancing mixing, as detailed in Section 1.8.2. A study by M. Khosravi Parsa et al. demonstrated comparable results through numerical simulations of sinusoidal channels, reinforcing the concept of improved mixing through structured geometries. [95] To evaluate the differences between 3D and 2D analysis mixing index and the flow pattern at the end of the device was compared as seen in Figure 4.3.3.

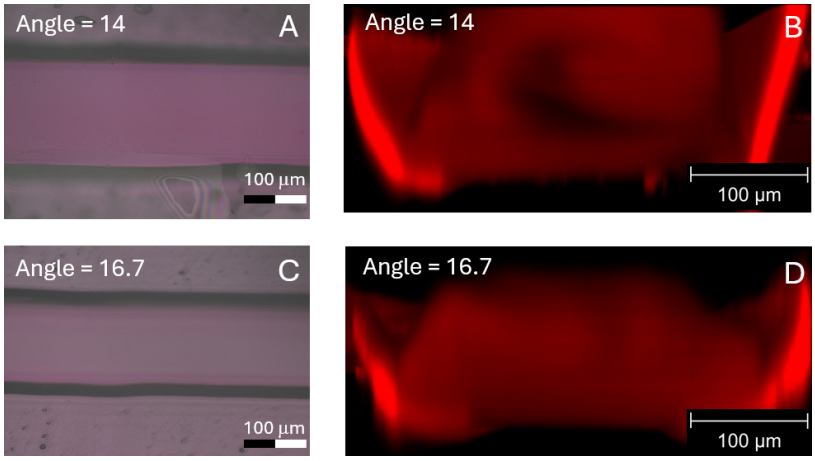

Figure 4.3.3. Comparison of 2 microfluidic devices mixing performance of DIW and rhodamine B with zig-zag angle of 14 and 16.7 degrees. A, C – using optical microscopy and C, D – confocal microscopy. measurement location as indicated by Figure 4.3.1. location 2.

It was observed that optical microscopy can lose detail, making it difficult to observe vortex effects within the channel (Figure 4.3.3). This limitation arises from light absorption properties inherent in reflective microscopy, where light must penetrate the sample, scatter, and then return to the detector. According to the Beer-Lambert law [131]

$$I = I_0 exp^{-ax} \tag{4.3.1}$$

Where I is the light intensity, a -absorption coefficient, x – length. The intensity of light diminishes exponentially as it travels through the medium. By setting $I = I_0/exp$ and solving for x penetration depth, at which light intensity decreases to 37 % of its initial value, can be determined:

$$x = \frac{1}{a} \tag{4.3.2}$$

The absorption coefficient α of Rhodamine B is documented at 106,000 cm^{-1}[125], allowing the calculation of a penetration depth of 94 µm. Given that the reflective microscope setup requires light to traverse to and from the sample, a factor of 2 is

introduced to account for this intensity loss, resulting in an effective depth of 47 μm. Comparing the mixing intensity within the first 47 μm of the channel depth to that of the entire channel reveals a notable difference, as shown in Figure 4.3.4.

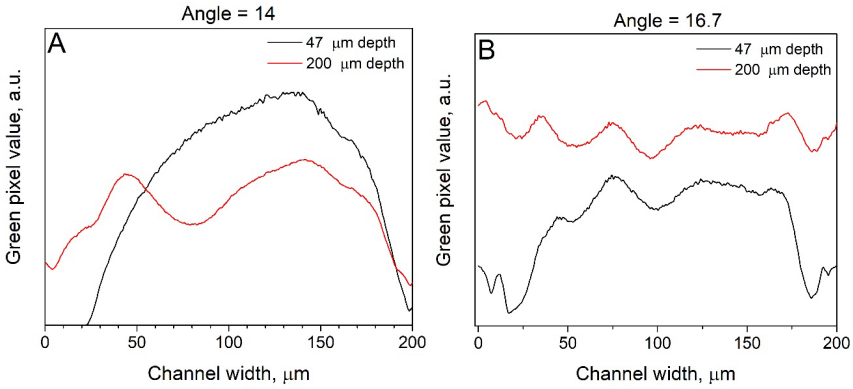

Figure 4.3.4. Integrated pixel intensity for confocal image Figure 4.3.3. B and D from top 47 μm and the whole channel.

Figure 4.3.4 illustrates the integrated pixel intensity for confocal images shown in Figure 4.3.3 B and D, comparing the top 47 μm to the entire channel depth. Firstly, considering Figure 4.3.4A and Figure 4.3.5 angle 14 data it can be observed that the integrated values for the 47 μm depth align closely with the values obtained from optical microscopy with an intensity increase in the middle validating that top layer has a considerable influence on the result. However, when comparing the results over the full channel depth, Figure 4.3.4A and 4.3.5 differ considerably, further validating that optical microscopy can lose important detail.

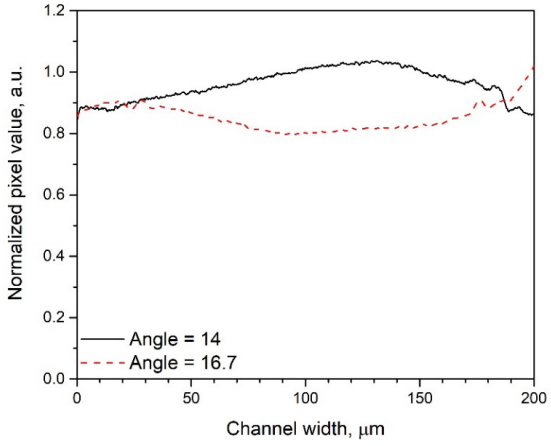

Figure 4.3.5. Normalized pixel values from optical microscopy, for devices with zig zag angle of 14 and 16.7 degrees (A and C Figure 4.3.3.).

Secondly in the analysis of Figure 4.3.4B and the angle 16.7 data from Figure 4.3.5, a notable similarity is observed between the 47 μm depth values and the whole channel depth. This consistency suggests that homogeneous mixing has occurred, as indicated in the confocal image.

A key observation lies in the relative mixing index, where angle 14 device had an RMI of 0.95 while angle 16.7 device had RMI of 0.85. 2D RMI comparison to 3D optical confocal visualization leads to a contradictory statement, highlighting the disparity between 2D optical microscopy and 3D imaging results. This further emphasizes that optical microscopy may only capture surface-level flow and can overlook deeper 3D effects present in the channel. Therefore, it is crucial to account for these 3D effects when evaluating mixing, particularly in cases involving complex flow dynamics. Given these findings, it's crucial to incorporate 3D imaging techniques such as particle tracking or confocal microscopy for accurate mixing evaluation, especially in cases with intricate flow dynamics.

4.4. Fundamental analysis of the flow pattern

Confocal microscopy provided a detailed insight into the complex flow pattern when a sharp corner was introduced into the design. To that end, a simple system consisting of straight channel and a bend was created to analyse flow patterns using fluorescence 3D confocal microscopy. This device was fabricated using the same procedure with OSTE 220 as detail previously. The design of this device is shown in Figure 4.4.1.

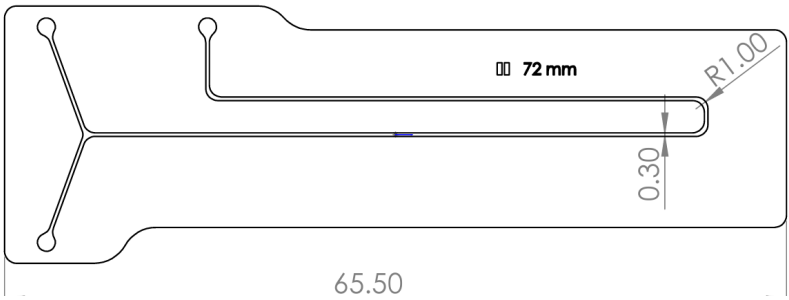

Figure 4.4.1. Single channel device drawing.

The measurements were carried out in the same way as before, by infusion of rhodamine B and DIW in the microfluidics channel. The infusion was set at 100 μl/min and the flow was observed in the locations noted by orange doted circle in the following Figures.

Out of initial observations by combining both flows at 140 degrees fluids do not intercept and mixing happens only due to diffusion which is a rather slow process. As per Figure 4.4.2, it can be seen that after 50 mm there is no noticeable mass transfer from rhodamine B to DIW. At the start of the first bend the flow follows a typical laminar flow pattern with rhodamine B at the outer side and DIW at the inner side

as seen in Figure 4.4.3. By comparing the confocal image to the optical microscopy image, there are few differences as optical microscopy image suggests a better mixing performance after the first bend.

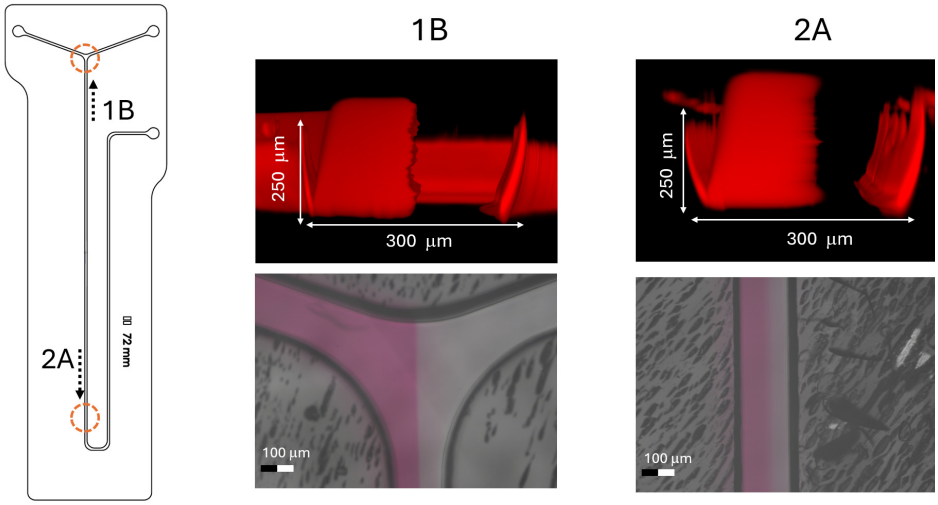

Figure 4.4.2. Mixing of rhodamine B and DIW in a simple channel. Where top images are confocal microscopy (0.1 mM) and bottom optical microscopy images (1 mM). Measurements for confocal microscopy are a side view scanned from the top and the direction of view is indicated by the dotted arrow. Numbers indicate measurement locations at different device locations.

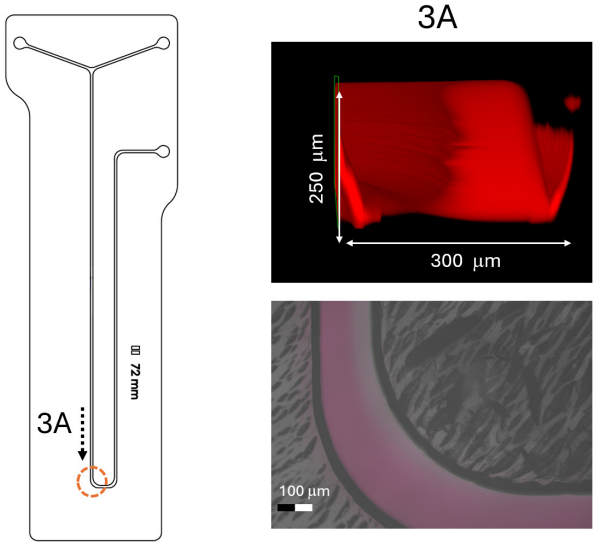

Figure 4.4.3. Confocal and optical microscopy image at the first bend of the channel where confocal image view direction is from the inlet indicated by A and doted arrow.

The process can be better understood by looking at Figure 5.4.4 where after the first bend (Figure 5.4.4 3B) there is a flow pattern change. This change shows that the flow becomes U-shaped. Furthermore, further down the channel (Figure 5.4.4 4B) local vortex is observed at the bottom of the flow pattern. By comparing the confocal image to optical microscopy, it can be understood that by moving rhodamine B to the top of the channel optical image would appear more mixed compared to the reality where the flow has not mixed, rather just changed its pattern.

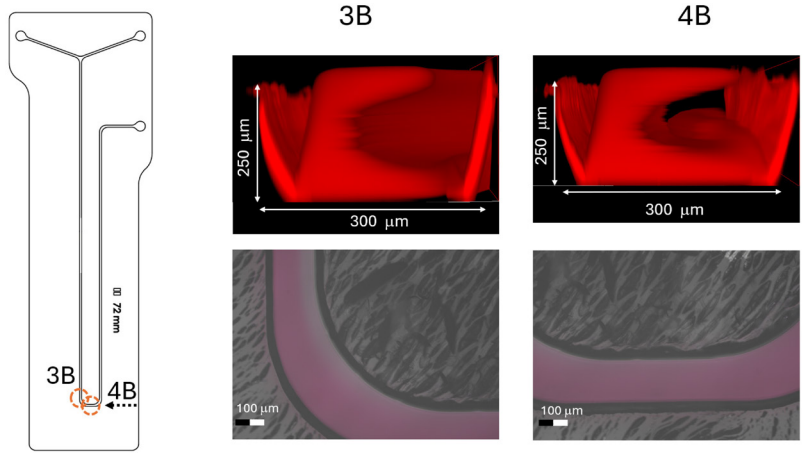

Figure 5.4.4. Confocal and optical microscopy image after 1st bend looking from the outlet side indicated by B and dotted arrow.

This observation is even more intensive after the second bend as the pattern is further disturbed and the small vortices have increased in size (Figure 5.4.5.) whiles the optical image seems close to fully mixed.

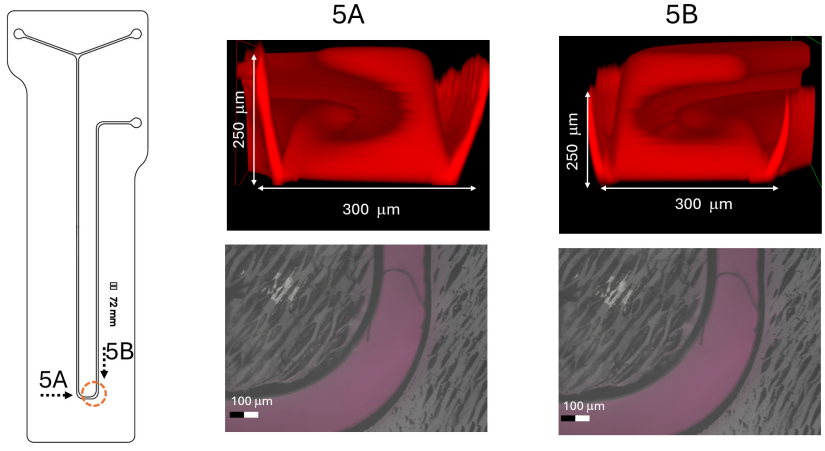

Figure 5.4.5. Confocal and optical microscopy image at 2nd bend looking from inlet 5A and outlet 5B indicated by the dotted arrow.

As flow progresses in the straight channel after the bend flow pattern changes back to U shape. (Figure 5.4.6.) This is an interesting observation as for laminar flow it is assumed that such movements would be unlikely unless gravity would be taken into account. Nevertheless, the diffusion of the bulk of the fluid is rather slow and does not considerably contribute to the overall mixing performance.

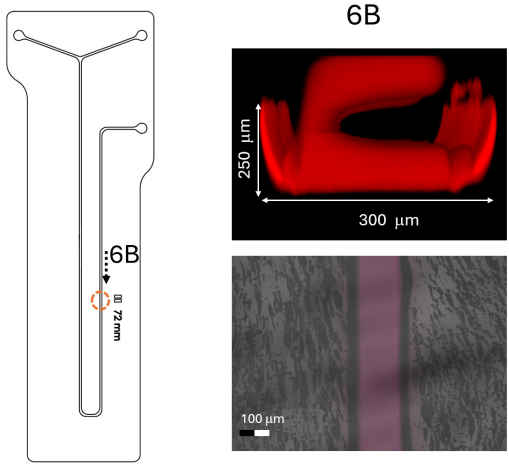

Figure 5.4.6. Confocal and optical microscopy image at the 72 mm mark of the microfluidics device.

A similar observation to the first and second bend can be observed at the third bend as just at the beginning of the turn flow pattern is the same (Figure 5.4.7 7B) and after the bend (Figure 5.4.7 8B) a small vortex has formed at the bottom of the flow. Meanwhile, only a small difference in the optical microscopy images can be observed.

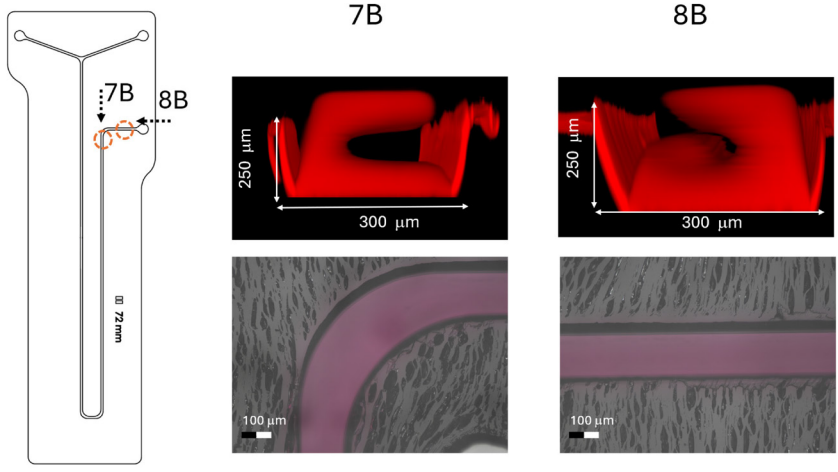

Figure 5.4.7. Confocal and optical microscopy images at the 3rd bend looking from outlet 7B and near the outlet looking from outlet 8B indicated by the dotted arrow.

During the experiments, distinct secondary flow patterns, specifically Dean vortices, were observed within the curved microchannels of the OSTE-COC device. These patterns became evident as the fluid traversed through bends in the microchannels. Given the low Reynolds numbers involved in these experiments, ranging from 10 to 100, the observed phenomena are noteworthy, as they illustrate the nuanced behaviour of fluid flow in microfluidic environments under conditions where inertial and viscous forces are comparable.

The fundamental process occurring can be partly explained by Dean vortices and secondary flow dynamics. Dean vortices arise due to the interaction between inertial forces and viscous forces in a curved flow path, such as the bends present in microfluidic channels. This phenomenon can also appear in low Reynolds numbers (10–100) when inertial forces of the fluid are comparable to the viscous forces. Conservation of mass and momentum can be used to better explain the phenomena as the bends of a device induce flow velocity changes, causing the fluid at the outer edge of the bend to flow faster than the fluid on the inner edge. This difference in velocity leads to the formation of Dean vortices, which alter the flow pattern and enhance fluid mixing. The Dean vortices formation probability can be estimated using Dean number:

$$De = Re\sqrt{\frac{d}{2r_c}} \tag{4.4.1}$$

For the experimental single channel device channel systems (Figure 4.4.1.) Dean number is 5.8 which is a rather low value and typically could display only very mild vortices formation, yet partly formed vortices can be observed in Figure 4.4.5. This process is interesting as the nearly formed vortices collapse rather quickly just after a few mm (Figure 4.4.6.).

By comparing single channel device channel systems to micromixers that were described in Section 4.2 and 4.3, Dean number was 33,3. This value is high enough for the formation of some perturbations but cannot fully explain the vortex scale that is observed in Figure 4.4.3. to explain this discrepancy flow changes due to walls could be considered.

There are two key fabrication considerations for OSTE devices. First, the polymerization reaction may result in small holes in the channel surface layer, potentially altering flow patterns. Interestingly, such effects have been used intentionally in other studies where etched channel wall patterns enhanced mixing [132]. Second, high-aspect-ratio structures during OSTE fabrication can lead to over-etching at the base material, creating angled walls that are wider at the top potentially changing the flow pattern.

By considering the influence from device walls and Dean vortices the observed flow pattern likely emerges from the combination of the 2 as either mechanism alone could not produce such results. Nevertheless, this improves the overall understanding of the mixing module thus, it should be considered in case of further optimization.

4.5. Magnetic particle separation

Having established the efficacy of dye-based methods for evaluating the mixing dynamics within microfluidic channels, we now turn our focus to the subsequent phase of our research—magnetic capture and device optimisation. Ideally EVs would

be separated from whole blood. Unfortunately, separating EVs from whole blood is an immensely difficult task due to EV concentration, and potential clogging of the device by red and white blood cells.

In the scope of this thesis whole blood analysis will not be tackled, but a relevant viscosity buffer solution spiked with EVs will be used as an approximation. This section will detail the design optimisation of magnetic separation module and the exploration of magnetic configurations.

4.5.1. Device geometry optimisation

Before introducing EVs into the system, MP capture was tested using 1 µm iron core MP (Dynabeads™) suspended in a buffer solution. The testing was conducted using COC/OSTE322/COC devices, described in Section 3.1.

The experimental setup included the following components: MP in buffer solution, tubing, a pressure system (Elveflow OB1 MK3+), a sample tube, and a microfluidic device with a single N52 magnet. The magnet was positioned directly beneath the microfluidic device, resulting in a magnetic field distance of 1 mm to 1.4 mm from the MPs, given that the device substrate height is 1 mm. To control the flow, 150 µm diameter tubing was employed, as 800 µm tubing exhibited flow rates exceeding 400 µl/min at 5 mBar, which proved to be impractical.

Prior to the experiment, the MP-buffer solution was inverted to resuspend the particles and ensure uniformity, as the MPs tended to sediment within 10 minutes. Subsequently, the resuspended MPs in buffer solution were flowed through the OSTE322 devices.

The optimal design was determined by testing the captured MPs inside different aspect ratio channels, as indicated in Figure 4.5.1.1. The aspect ratio of the device is defined between the height and width of the widest device section using a constant device height of 400 µm. The quantification of MPs was determined by comparing the MPs that were outflown post-capture and MPs that were captured in the device. This was done by dissolving MPs in *Aqua regia* (35 % HCl and 65 % HNO_3 at volume ratio 4 : 1) after which the solution was quantified by optical absorption, as described in Section 2.4.3.

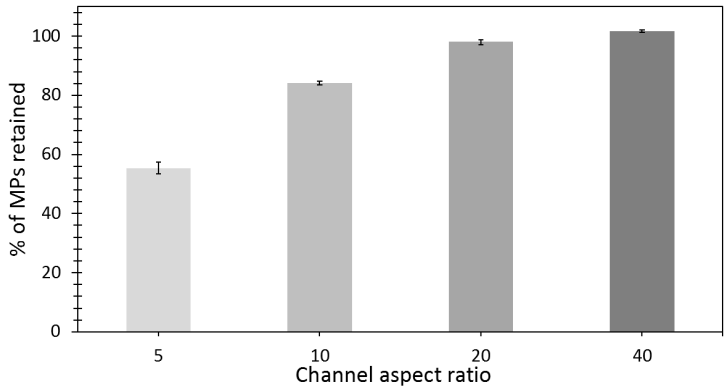

Figure 4.5.1.1. MPs retention based on channel aspect ratio, measured by the quantity of iron particles before and after passing through the device.

The experiment demonstrates that a larger aspect ratio results in higher MP capture efficiency. This correlation can be attributed to the increased surface area available for MP capture in devices with larger aspect ratios. In contrast, smaller channels are less effective at retaining MPs because the particles tend to form multiple layers within the channel, which effectively reduces the channel's cross-sectional area. This reduction in channel size increases the flow rate, making it less likely for MPs to be captured by the magnet.

To address this issue, larger channels could be made, but smaller channels are preferred due to intrinsic need for miniaturization. Additionally faster flow rates are preferred. This was a noticeable problem as indicated by Figure 4.5.1.2 which shows that by increasing flow rate capture rate noticeably decreases, where nearly 100 % retention is observed at 100 µl/min, but just 55 % retention at 400 µl/min. The capture rate at 400 µl/min is important as higher speeds mean shorter processing times, which are important for clinical applications.

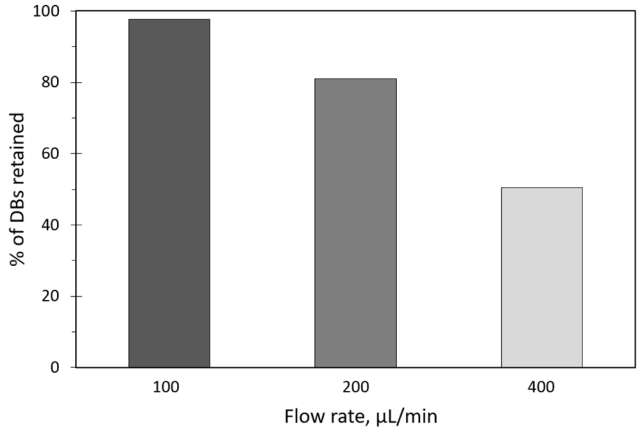

Figure 4.5.1.2. MP retention with respect to flow rate for AR20 channel using single N52 magnet under the device.

4.5.2. Magnet configuration optimisation

Even relatively large channels (AR20) demonstrated suboptimal performance, and further increasing the channel aspect ratio was not feasible due to the mechanical limitations of the COC materials. Beyond an aspect ratio of 20, the channels exhibited noticeable deflection, necessitating additional supporting structures. To address this issue, various magnetic configurations were tested to enhance the magnetic field strength and improve MP capture. Four distinct configurations were evaluated for this purpose, as illustrated in Figure 4.5.2.1.

The comparison was conducted against the original system, which utilised a single N52 magnet (Figure 4.5.2.1a). Three additional setups were tested to evaluate improvements in MP capture efficiency. These included: (1) two N52 magnets placed above and below the channel (Figure 4.5.2.1b.), and (2) a stack of 18 N45 magnets

arranged in two configurations: opposing polarity, where the north and south poles are stacked laterally (Figure 4.5.2.1c), and a Halbach array configuration (Figure 4.5.2.1d).

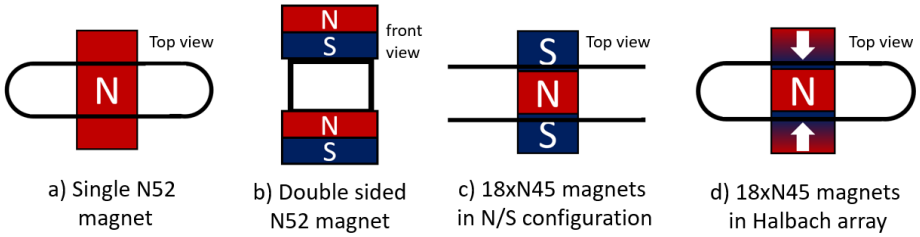

Figure 4.5.2.1. Different magnetic configurations for the magnetic arrays under the channel. [133]

The magnetic configurations were tested with channels of aspect ratios (AR) 5 and 10. MPs in buffer solution were introduced into the microfluidic device using a pressure system, set to a flow rate of 200 µl/min. After the initial flow, the outflow was collected. Subsequently, the magnet was removed, and the captured MPs were eluted into a 1.5 ml tube (Eppendorf). The quantitative analysis of the MPs was performed by dissolving MPs and measuring optical absorption, as detailed in Section 2.4.3. The results for the different configurations are presented in Figure 4.5.2.2.

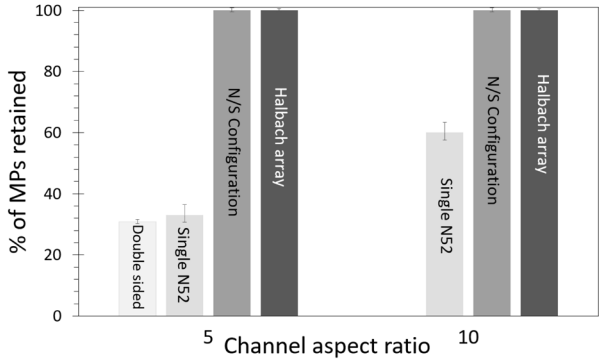

Figure 4.5.2.2. MP retention based on different magnetic configurations.

The results suggest that by using 18 N48 magnets impressive retention improvement is observed. This is due to the definition of magnet N rating as, it is a product of magnetisation hysteresis cycle where the number is acquired by first magnetizing the magnet using an electromagnet, and after turning it off the residual magnetic strength is the N rating. [134] This leads to possibility to increase the magnetic field using multiple small magnets if they are arranged correctly to amplify their fields strength rather than to diminish it.

In particular, the Halbach array configuration, which directs the magnetic field upwards, demonstrated superior performance by capturing over 95 % of MPs in the AR5 setup, compared to 90 % in the N/S configuration. This configuration efficiently redirects the magnetic field from the bottom to the top side, thereby increasing the magnetic field strength on one side while the N/S configuration maintains identical field strengths at both top and bottom, resulting in a weaker magnetic effect per side.

These considerations ultimately led to the choice of the N/S configuration for devices with an aspect ratio of 10 and above. This configuration effectively captures over 95 % of MPs and maintains stability in the magnetic field arrangement. However, in scenarios requiring a more intensified magnetic field – such as devices with smaller capture chambers or when minimizing field strength beneath the magnet to avoid interference with sensitive analytical processes – the Halbach array presents a viable alternative. Despite its advantages, implementing the Halbach array involves addressing fabrication challenges, necessitating careful optimization of the assembly process to ensure structural integrity and functional efficacy in practical applications.

Figure 4.5.2.3 presents an optical image of the MP capture process during active flow. In the AR 10 configuration, 70 μg of MPs were captured, with only 26 % of the capture chamber area utilized. This design demonstrates optimal performance for microfluidic applications, as it effectively captures over 98 % of MPs while accommodating relatively large sample volumes for this scale. Additionally, the design provides a considerable margin for error, including tolerance for flow fluctuations and potential disruptions caused by bubbles.

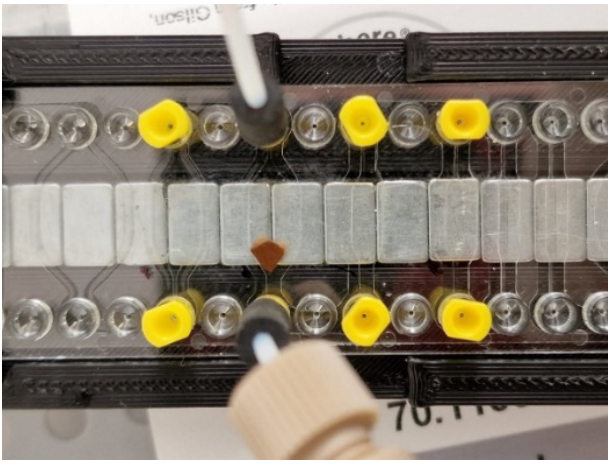

Figure 4.5.2.3. Example of MPs capture.

4.6. Particle separation using biological sample

With the optimal magnetic configuration and channel dimensions established, it was essential to test the system using a biologically relevant sample. A key challenge in EV analysis is the instability of EVs in standard environmental conditions. The stability of EVs can be influenced by multiple factors, including biophysical properties, environmental conditions (such as temperature and pH), and the presence of degrading enzymes. In biological contexts, enzymes and other cellular components can degrade EVs. Similarly, EV degradation can also occur in experimental settings due to improper handling or storage conditions. To evaluate the stability of EVs under mechanical stress and quantify degradation in controlled laboratory settings, an experimental procedure was devised.

4.6.1. Shear Stress Effects on EV Integrity at Different Flow Rates

To investigate the impact of shear stress on EV stability, a flow rate sweep was conducted using fluid flow as a shear stress inducer, effectively simulating the dynamic conditions encountered by EVs within vascular systems. To assess how increasing flow rates (100 to 500 µl/min) influence EV survivability due to increased shear stress EVs produced by PC3 and lymph node carcinoma of the prostate (LNCaP) cell lines in a bioreactor, (Latvian Biomedical research and study centre) were used.

Sample preparation starts with the conjugation of commercially available 1 µm MPs (Dynabeads™ MyOne™ Carboxylic Acid, ThermoFisher) with anti-CD63 antibodies to create MPs with surface proteins for specific EVs. These MPs and EVs were mixed using a standard laboratory protocol involving an overnight incubation in a rotating mixer (10 RPM, +4 °C), achieving near 100 % capture efficiency. To ensure the purity of the experimental setup, each device channel was cleaned with 1 mL of 3 % H_2O_2, 1 mL of 70 % ethanol, and 4 mL of PBS. The channels were then sealed with PBS buffer overnight.

The testing of different flow rates was carried out in an identical setup as described in Section 4.5.2, in short a tube with recently (< 1 min) inverted sample was connected to pressure system, and the microfluidics device using 150 µm PTFE tubing, to ensure flow rate 100–500 µl/min. After the capture magnet was removed and EVs bound to MP were eluded in a DNA low-bind Eppendorf 1.5 ml container. The EVs were then subsequently washed, lysed, and frozen in preparation for analysis.

qPCR analysis was performed using the miRNEasy micro kit, adhering to the protocol outlined in Section 2.4.5. The qPCR values were recorded at the 2.5 billion replication mark, corresponding to 26 to 32 cycles, by assessing the integrity of Mi375 protein—a marker present in all LNCaP EVs. The analysis utilised UniSp6 protein as a reference to normalise the results and reduce technical variability.

A challenge for EV analyses is that EVs degrade in temperatures above –80 °C, and the binding rate is temperature-dependant. Thus, experiments need to be carried out quickly and additional controls must be used. To address this, degradation was quantified using qPCR to compare the levels of the Mi375 protein in EVs before and after the experiment.

As demonstrated in Figure 4.6.1.1, a decrease in signal intensity of about 20 % was observed over a 5-hour period even with the sample stored at +4 °C between all experimental conditions. The instability of EVs at +4 °C holds particular significance for their potential applications in fields such as cosmetics, where they could be used in anti-ageing or skin barrier repair products.

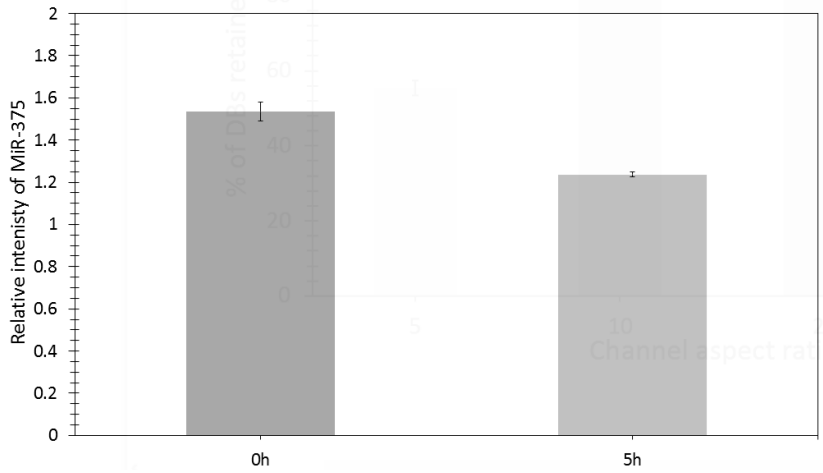

Figure 4.6.1.1. qPCR signal comparison between control EVs not subjected to the microfluidics device and those that were, measured at the start of the experiment (0 h) and after 5 hours (5 h).

Due to degradation for the rest of the data set, a linear correction was introduced to account for a 20 % intensity drop, assuming a linear relationship between survivability and qPCR signal intensity. This correction was uniformly applied across the dataset to mitigate the distortive effects of sample degradation or loss, ensuring that the qPCR results more accurately reflect the actual concentration of intact EVs under tested conditions.

Figure 4.6.2.1 illustrates the EV survivability as a function of flow rate. The graph indicates that at a flow rate of 400 μl/min, there is negligible damage to the EVs. While there appears to be a slight decrease in EV survivability at 500 μl/min, the data does not conclusively show a significant decline. This uncertainty is due experimental setup where each condition corresponds to a single biological sample and the error bars represent technical replicates which are samples that were separated post lysis and analysed separately on qPCR device.

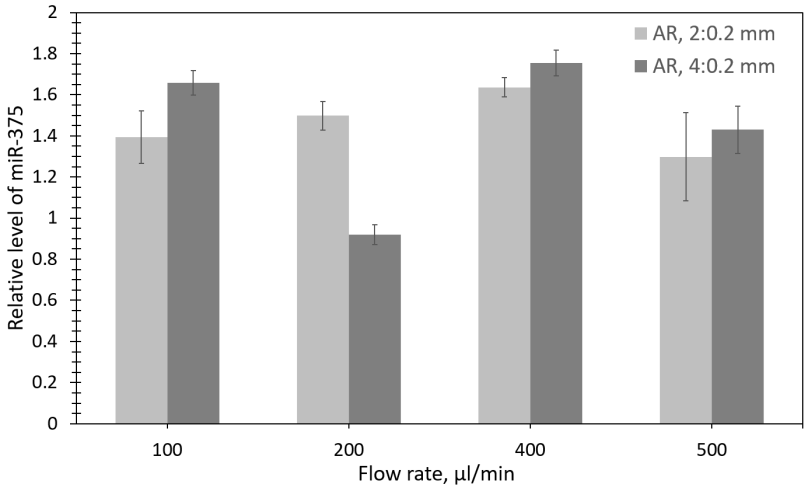

Figure 4.6.2.1. qPCR of Mi375 protein extracted from captured EVs based on flow rate, and channel width.

Due to sample handling the qPCR value at 300 µl/min was omitted from the results as it showed abnormally high mir-375 relative intensity at 2.8 which was removed on basis of experimental protocol mistakes.

A key advantage of the qPCR method is its ability to provide a quantitative analysis of captured intact EVs. Given that miR-375 is an RNA molecule, its stability outside of EVs is compromised due to the pervasive presence of ribonucleases. Therefore, the signal intensity obtained from qPCR serves as a direct measure of undamaged EVs, making it a reliable indicator of EV integrity.

Subsequently, two conclusions can be drawn:

1. There is negligible loss of EV integrity Up to 400 µl/min (t = 1.11, Re = 19.1), and further devices can be optimized based on this assumption.
2. There is a potential decrease in EV survivability at shear stress value of 1.4 Pa at the channel walls (Table 4.6.1.1), noting a potential limitation for maximum speed at which a device can operate.

Table 4.6.1.1. Numerical conversion of flow rate.

Magnetic separation device (300 × 400 µm)		
Flow rate, µl/min	**Wall shear stress, *t* (Pa)**	**Reynolds number, *Re***
100	0.28	4.8
200	0.56	9.5
300	0.83	14.3
400	1.11	19.1
500	1.39	23.8

These findings provide a foundation for further device development and integration with other modules. Understanding that EVs might lose integrity due to wall shear stress is crucial in guiding future designs. Additionally, the magnetic capture module has demonstrated a high capture efficiency, indicating its readiness for integration with other components in subsequent experiments.

4.7. Integration of modules

Having established the efficacy of dye-based methods for evaluating the mixing dynamics within microfluidic channels, it was concluded that while these methods provided valuable insights, they also revealed limitations in fully capturing the mixing process, especially when considering EVs, which considerably differ from dye molecules. By combining 2D experiments and 3D analysis, a comprehensive understanding of the fluid dynamics involved was developed. This broad knowledge, coupled with the consideration that biological system interaction times can range from minutes to days, necessitated a design optimization.

4.7.1. Integration of mixing and magnetic separation module

To integrate microfluidics systems and facilitate the use of biological samples, channel length was increased from 74 mm to 800 mm and the number of bends were increase from 12 to 510, to considerably enhance the interaction probability. Additionally, changes were made in device fabrication: the 1000 μm COC slide was replaced with a 140 μm thick COC film due to its flexibility, improving bonding yield. This modification was crucial for increasing device yield, as achieving less than 100 % functionality through the device was no longer acceptable. Previously, with the test design, having seven channels on a single slide meant that the overall design remained functional even if 2 out of 7 channels failed. However, with the new design, the channel spanned the entire slide length, meaning that any major defect would compromise the entire device, substantially raising fabrication requirements. This led to number of fabrication changes from Section 3.2.

Initially, the Qsil mold was designed with built-in pillars to support the structure and prevent height variations. However, since the 140 μm film used in the process is less rigid than a 1 mm thick COC slide, additional pillars had to be incorporated into the design. This introduced a challenge where alignment tolerance had to be reduced to 500 μm. Mold shrinkage, combined with the need to support the entire device, resulted in a cumulative error. This was further amplified due to the need for low alignment tolerance leading to a considerable error were misaligned pillars ended up within the channel locations.

To address the shrinkage issue, a pillar array was printed, and the location of each pillar was measured using a microscope (Nikon, Eclipse LV150N). It was determined that applying a 0.67 % shrinkage correction factor to the pillar array design effectively eliminated the overlap between pillars and channels, resolving the alignment problem.

Additionally, the flexibility of the COC film allowed it to conform more effectively to minor surface imperfections compared to rigid slides. This improved bonding quality enabled further optimization resulting in a determination of a precise dose of 107.5 mJ and a development time of 75s at 80kHz and 50 % power (Elmasonic P).

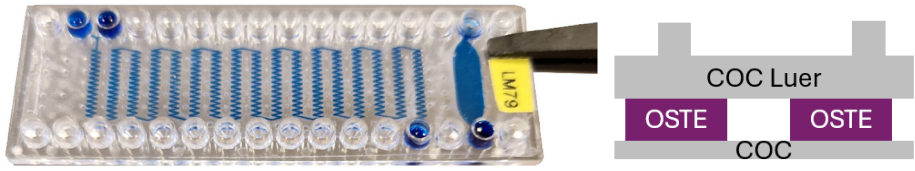

Figure 4.7.1.1. Finished device on the left and side view schematic on the right (not in scale).

The Final device channel geometry was 200 µm × 200 µm with a total channel length of 800 mm. The integrated magnetic capture module had a width of 4 mm, height of 200 µm and length of 18 mm.

While considerable changes were made to the mixing module, the magnetic capture module was only adjusted to be integrated into the same chip. This integration is notable as it increased the magnetic field in the microfluidics channel by decreasing the distance from the magnet to the channel by 860 µm. This change is potentially beneficial as a higher magnetic field previously resulted in improved capture efficiency.

4.7.2. Device quality control

To increase production scale and create device suitable for biological sample analysis additional quality control had to be introduced. As biological samples will have to use different devices to ensure sterility, all fabricated devices must be as similar as possible. Thus, height measurements were performed across the whole device to evaluate the device quality.

Initially this was done using an optical microscope, as the focus height can be used to precisely measure the distance between COC film, and COC luer slide, thus giving the height of OSTE. While useful, this measurement was impractical as it was time-consuming and finding the correct was focus difficult. Even more so the precision is around 20 µm due to the imprecise of the dials and difficulty finding the focus. As such a digital micrometre was utilised. This was done using an optical rail as a base to provide, a flat surface, and a luer-slide as a 0-reference point. (Figure 4.7.2.1.)

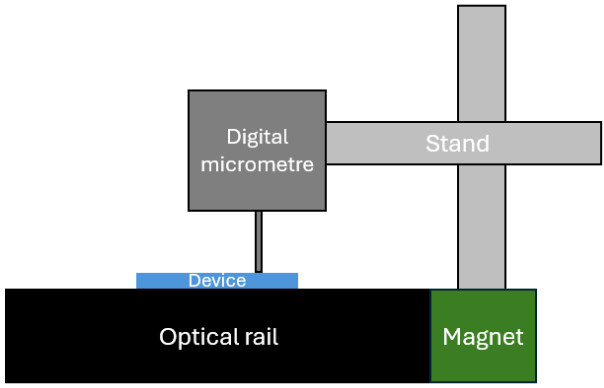

Figure 4.7.2.1. Schematic of micrometer measurements.

It was possible to acquire high data, such as the distance from the luer slide, using micrometre. After subtracting the standard 140 µm film thickness, it was possible to acquire the thickness of OSTE channels and by positioning it at different point across the whole device thus an hight map was acquired. (Figure 4.7.2.2.)

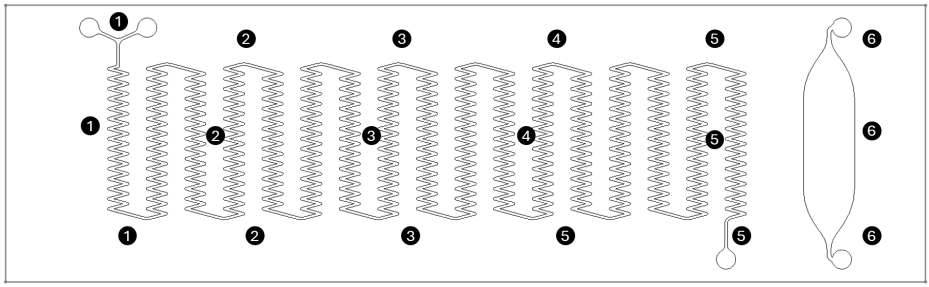

Figure 4.7.2.2. Measurement points on the device. The number indicates the columns that were measured.

To determine the precision and correlation of the results from the digital micrometre and optical microscope, the height map of 4 devices were compared as-shown in Figure 4.7.2.3 and Figure 4.7.2.4.

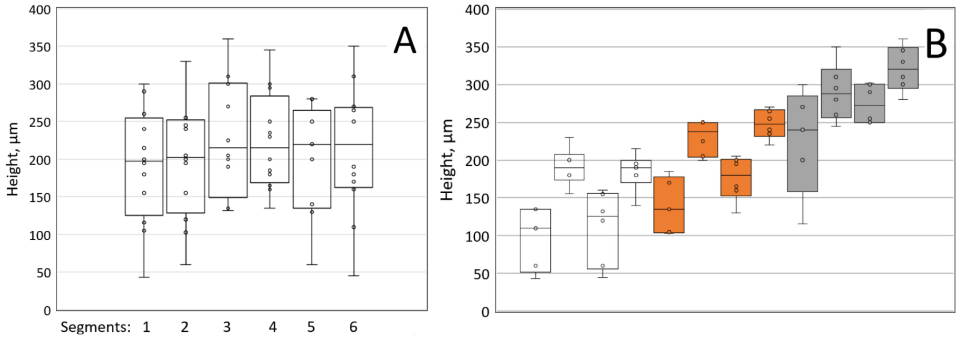

Figure 4.7.2.3. Optical microscope height measurements of columns, left where each box and whiskers graph represent a different segment of 4 devices (A). And right where each box represents a different device and each colour represents different segments, white – top, orange, middle, grey – bottom, (B) as noted in Figure 4.7.2.2

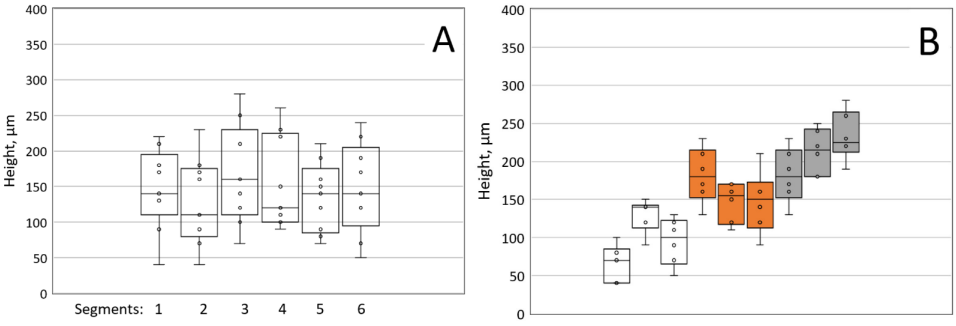

Figure 4.7.2.4. Digital micrometre height measurements of columns, left where each box and whiskers graph represent a different segment of 4 devices (A). And right where each box represents a different device and each colour represents different segments, white – top, orange, middle, grey – bottom, (B) as noted in Figure 4.7.2.2.

A higher variability in optical measurements was observed, attributed to difficulties in achieving focus at specific locations. Both methods yielded similar results, indicating that either method can effectively represent the device height. Consequently, for further evaluation, only the digital micrometre method was used

To fully address the quality of the device standard deviation across the device and a batch of devices was used. This allowed to quantify channel quality in a single number which was useful for further experiments. When combined with visual inspections to identify issues such as misalignment, this method was deemed sufficient for quality control.

4.8. Flow rate influence on EVs in mixing module

The integration of the mixing and capture modules marks a notable stepping stone towards a lab-on-chip device, as these two modules form the foundation of sample preparation. To that end, a comparison between traditional and microfluidic approaches was necessary. This comparison was performed by conducting a flow rate sweep under conditions relevant to sample viscosity. Experimentally, LNCaP bioreactor EVs were utilized in the microfluidic device, employing 1 µm diameter iron core MPs conjugated with Anti-CD9 Nb nanobody for EV capture. Following mixing of MP-bound EVs, capture was executed either on-chip or in a tube, with subsequent washing performed either on-chip or off-chip.

For on-chip capture, MPs were washed with a buffer solution at 200 µl/min and then collected in a new container. Off-chip capture followed standard procedures where MPs with EVs were captured and collected in a container, then subsequently captured using a bench-top magnet. This was followed by triple washing and re-capture steps, after which the sample was collected. Post-collection, the EV and MP solution

was lysed, and Western blot analysis was performed. Figure 4.8.1 illustrates the relative intensity of the CD63 bands, reflecting the EV capture efficiency across both on-chip and off-chip workflows.

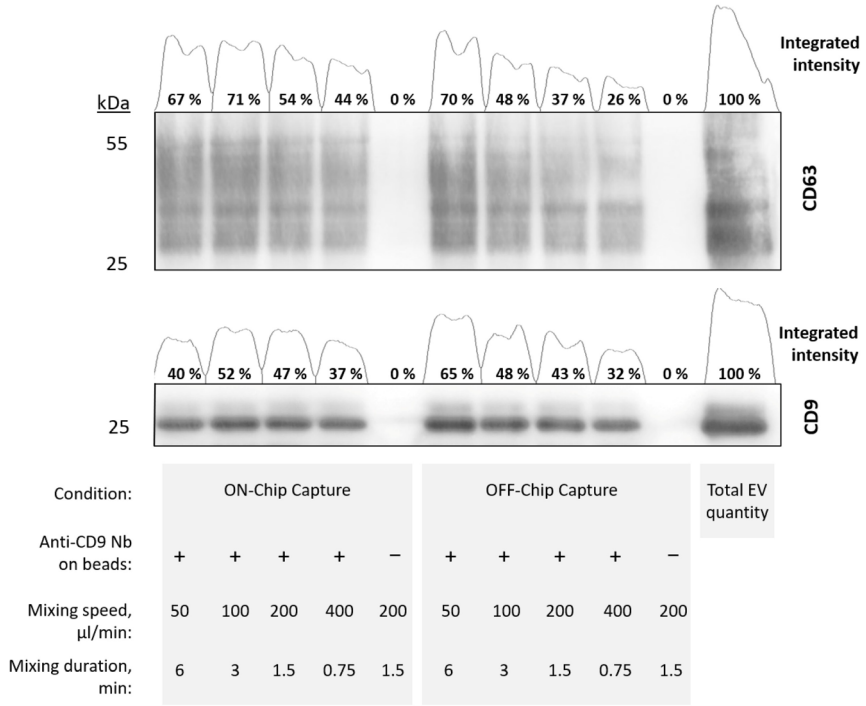

Figure 4.8.1. EV survivability based on flow rate and capture type, for integrated system. The top image is Western blot, where darker band indicates higher intensity, which is represented by the integrated value above.

A key parameter in Western blot analysis is that it is a relative method, where comparisons should be made within a single gel. This approach is recommended because experimental conditions and data capture can introduce various errors that are difficult to accurately quantify. If multiple gels are necessary due to the number of samples, an identical control must be included on each gel to allow for correlation and corrections across the datasets. In this experiment, a single gel was used, and a pure EV solution with a concentration ($3x10^9$ LNCaP bioreactor EVs per 150 µL) was employed.

For the experiment Anti-CD9 nanobodies (Nb) was the protein used to interact with CD9 protein on the EVs, thus linking them together (EV capture). A control condition, denoted as (–), involved MPs without CD9-conjugated surface proteins, preventing specific EV binding and isolating nonspecific interactions. Conversely, the experimental condition denoted as (+) used MPs with conjugated CD9 nanobodies,

allowing both specific and nonspecific EV capture. This setup enabled the assessment of binding specificity by comparing results between the (+) and (–) conditions. This assessment is relevant as EV surface is lined with different proteins that each can interact in different ways, for example by interact with the surface of MPs. As such, it is critical to evaluate nonspecific binding. The western blot results show that for this experiment nonspecific binding is less than 0.5 %, as all 3 nonspecific binding tests were lower than 0.5 % of EV control intensity.

The Western blot results from Figure 4.8.1 reveal that at 50 µl/min in standard laboratory setups, the intensity accounts for 70 % and 65 % of the total EV count for CD63 and CD9, respectively. This surpasses the microfluidics setup, which shows 67 % and 40 % for CD63 and CD9, respectively. This discrepancy could be attributed to differences in setup configurations. In the microfluidics setup, capture occurs on-chip, ensuring that all non-captured EVs pass through magnetically bound MPs and are subsequently discarded. In contrast, the standard assay allows for post-mixing interactions within the container, potentially extending incubation time and enhancing signal intensity. Consequently, while the microfluidics setup provides a more precise indication of real interaction time, its signal intensity is compromised due to shorter incubation periods. This is further supported by the data dispersion seen in Table 4.8.1 which shows the standard deviation of the western blot results, where ON-chip capture provides a more consistent result compared to OFF-chip capture

Table 4.8.1. Standard deviation of the western blot data for EV capture utilizing ON-chip and OFF-chip capture.

Marker	**σ, on-chip capture**	**σ, OFF-chip capture**
CD9	12.4	18.8
CD63	6.8	13.7

The western blot intensity at 45 seconds shows a potential decline in intensity which could be either attributed to measurement error or start of loss of integrity for EVs. This can be supported by the fact that shear stress at 400 µl/min in this microfluidics set up is 5 Pa whiles previously (Figure 4.8.1) the maximum shear stress was 4.2 Pa at 500 µl/min (Table 4.8.2). while the Reynolds number is identical at 33.3. This points to a likely loss of integrity for EVs at this shear stress as 2 distinct experiments with different detection methods follow a similar trend. Nevertheless, it is not a solid proof as western blot error bars are not fully defined and additional experiments with multiple repeats (3+) would be required to validate this theory.

From theoretical point EV collapse is a difficult problem due to nature of EVs, small lipid bilayer particles, which can only be mechanically assessed using atomic force microscopy. The fundamental model of small cell collapse is mostly experimentally determined and there is a lack of good experimental proof. Determining EV collapse value is especially difficult due the broad size distribution (50–1000 nm) where for our experiments EVs are in range of 50 µm to 300 µm.

Table 4.8.2. Flow rate shear stress and Reynolds number.

Mixing device (200 × 200 μm)		
Flow rate μl/min	**Wall shear stress (Pa)**	**Reynolds number**
50	0,63	1,48
100	1,25	8,33
200	2,50	16,67
400	5,00	33,33

Nevertheless, for this research, EV collapse was recognized as a challenge related to speed and design optimization but was not the primary focus. The key objective was to enhance binding efficacy. To minimize potential EV destruction caused by wall shear stress, the flow rate was adjusted to induce stresses below 2.5–5 Pa. This adjustment ensured the structural integrity of EVs during experiments, allowing for reliable binding efficacy studies while mitigating the effects of shear-induced damage.

To facilitate enhance binding efficiency and better understand the binding process, recirculation through the mixer was introduced, thereby increasing interaction within the mixing module. This adjustment aims to improve binding efficiency and provide a clearer understanding of the interaction dynamics.

4.9. Integrated device analysis with EV sample

The proof-of-principle device performance was assessed by analysing the binding kinetics of EVs and MPs. For this task MP conjugation with CD9 nanobodies was done by Edgars Endzelins, following the protocol outlined in paper by Cipa et al. [135].

4.9.1. Prof-of-principle device constraints analysis

The initial consideration for the device includes previous experimental observation that 45 % of CD9-positive EVs were captured in a single run. Thus, recirculation of the liquid was deemed required to improve the binding efficiency.

To create a recirculation step, the maximum flow rate must be considered not only in terms of shear stress but also potential air creep due to a high difference in pressure induced by the syringe pump which if left unchecked could compromise the precision of 150 μl infusion and withdraw thus undermining the experiment. To that end 150 μl/min was chosen adequate as experimentally this flow rate produced consistent results for infusion and withdraw without the loss of operating pressure.

Additional constraint appears when recirculation is used as MPs movement inertia occurs after the flow is stopped thus a pause step is required to allow for pressure to equalize. For this purpose, 30 seconds were chosen so that no visible flow movement was observed. Lastly minimum time for a single cycle for such as system is 5 minutes due to flow rate and pause constraints.

The sample volume of 150 μl was chosen as it is the smallest amount that can be reliably analysed using western blot to obtain a reliable signal. Furthermore, as per

Section 4.6.1 a 20 % intensity drop was observed for EVs over 5 h time frame, thus for this experiment EVs were kept at 4C and on an ice block when removed from the refrigerator thus potentially reducing EV degradation.

Post capture, a washing step is used to remove non-specifically bound EVs which can attach to MP surface with Van der Waals force. As this force is relatively weak and only affects parts of the protein at varying distance these bonds can be broken using even low Re number flow. As it was demonstrated previously (Figure 4.8.1.) MPs without CD9 protein (–) had < 0.5 % of captured EV signal intensity.

4.9.2. Automation and sample handling

After accounting for experimental constraints, an automated flow sequence was developed. This approach combined both mixing and magnetic capture into a single processing step by preloading the buffer solution, followed by an air gap, and then the sample, as shown in Figure 4.9.2.1.

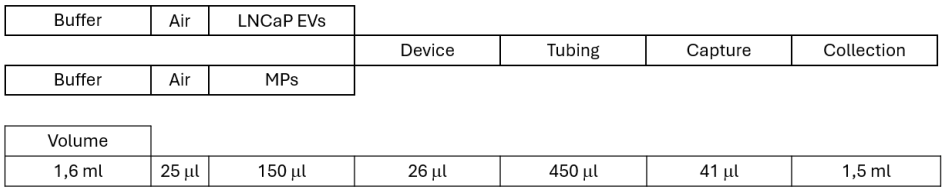

Fig 4.9.2.1. A schematic of the experimental setup.

The pre-loading allows for nearly a single step run, as parameters can be set, and device left to perform the preset program. To prevent sample diffusion into buffer solution as MPs move slower than the liquid itself due to inertial effects, a barrier was needed between sample and wash liquid. For this purpose, 50 µl air gap was used.

The recirculation of EVs and MPs was done in a 4-step process:

1. Infusion of 150 µl, at 150 µl/min;
2. 30 second pause;
3. Withdraw 150 µl, at 150 µl/min;
4. 30 second pause.

Post recirculation 450 µl tubing was removed and the mixing module was directly connected to the particle capture module. Subsequently particle capture and washing steps were performed by infusing 1.6 ml of buffer solution (PBS + 0.1 % BSA + 0.05 % Tween20) at double flow rate 300 µl/min. this step not only captures MPs but also washes them thus removing non-specifically bound EVs.

After the washing step, the capture magnet was removed and MPs with CD9 positive EVs were eluted using up to 1.5 ml of buffer solution and a flow rate of 150 µl/min. Afterwards MPs with CD9 positive EVs were centrifuged at 5000 g and supernatant was removed at a magnetic stand. Lastly, the sample was lyzed and frozen to be further analysed using Western blot.

4.9.3. Mixing and capture proof of principle experiment

To assess binding kinetics and demonstrate the performance of a proof-of-principle sample preparation unit, a complete system comprising an integrated mixing module and magnetic capture module was tested and compared to a standard lab assay in a semi-automatic operation setting.

The EV binding experiment was carried out using LNCaP EVs with CD9 conjugated MPs. The binding time was chosen from 5 to 50 minutes which corresponds to 1 to 10 cycles. The experiment was run against a control – a standard laboratory setup where a 1.5 ml container is filled with the same EV and MP sample, and rotated for 5–50 min, at room temperature (Figure 4.9.3.1.), as commonly utilised.

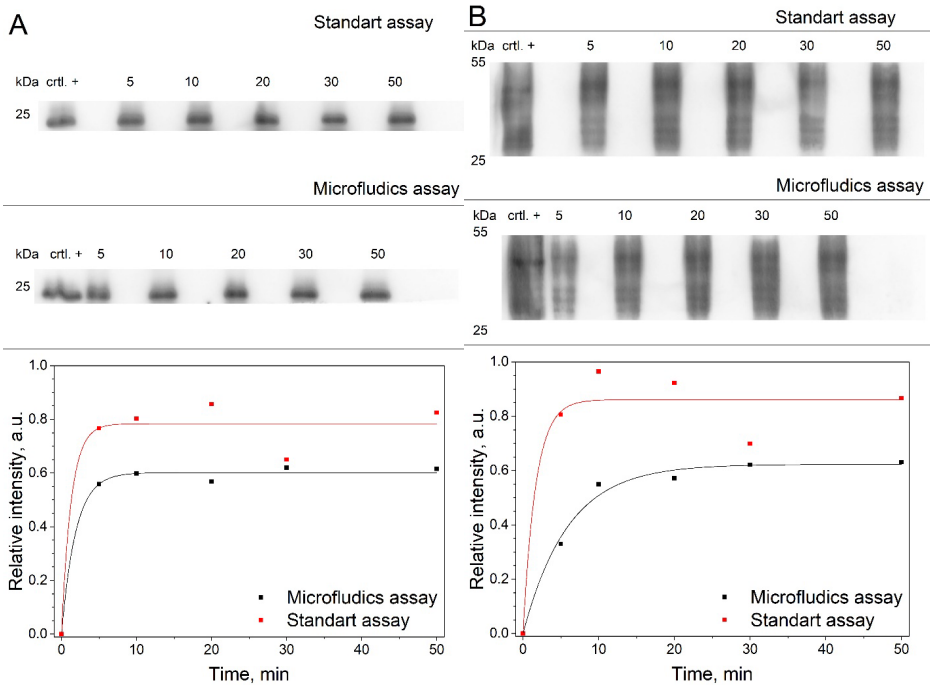

Figure 4.9.3.1. Western blot analysis showing the efficiency of EV capture. Anti-CD9 EV capture and CD9 detection (A) and WB results for anti-CD9 EV capture and CD63 detection (B) where the top Figure is WB image, and each data point is an integrated value relative to EV marker signal intensity.

To quantify the acquired Western blot data, band integration as indicated in Figure 4.9.3.1 was performed. To correct for self-luminescence of CD9 nano body (as they were used for both capture and detection) membrane was cut of below 20 kDa. Nevertheless, some background signal remained and was corrected using exponential decay function. This correction was used for all CD9 bands and same methodology was used across the whole data subsequently relative values could be accurately determined.

The Western blot signal in Figure 4.9.3.1A demonstrates that the maximum relative binding efficiency of EVs to MPs is $f_\infty = 0.60 \pm 0.01$, which is similar to the standard laboratory assay value of $f_\infty = 0.78 \pm 0.04$. Additionally, the CD63 analysis, using an anti-CD63 antibody as shown in Figure 4.9.3.1B, confirmed the successful capture of EVs or double-positive membrane fragments, rather than free-floating CD9 protein. The consistency of data from both markers supports that the majority of the signal originates from captured double-positive vesicles, with minimal to no contribution from free-floating CD9 protein.

To further evaluate the data, an exponential growth model $f = f_\infty(1 - exp(\sigma t))$ was fitted for the background corrected integrated WB values using the least square method where a similar model was employed by Petkovica et al. [136]. Here the f_∞ is the asymptotic value of the binding efficiency and s is the binding rate, with results summarized in Table 4.9.3.1.

Table 4.9.3.1. Asymptotic value of the binding efficiency and the binding rate of integrated WB signals.

	R^2	f_∞	**σ**
CD9 microfluidics	0,99	0,60	0.53
CD9 standard assay	0,94	0.78	0.77
CD63 microfluidics	0,99	0.62	0.17
CD63 standard assay	0.92	0.86	0.60

The data reveals that the majority of EV binding to MPs occurs rapidly, within the first 10 minutes of the reaction. This marks a considerable improvement compared to conventional laboratory assays, where MP binding to analytes typically requires one to 24 hours, as reported in multiple MP protocols [137], [138]. The faster binding in an on-chip system, combined with the possibility for automation, offers a notable advantage. By configuring initial flow control parameters, loading the sample, and removing the magnet, the process eliminates the complexity of conventional workflows that involve over 10 manual steps. This streamlined approach could be adapted for a simple laboratory instrument, enhancing efficiency and usability.

Finally, this thesis introduces new research into prostate cancer extracellular vesicle interaction with magnetic particles in microfluidics devices. The kinetics profile provides insight into small particle interactions with surface-modified particles, revealing logarithmic growth and rapid binding. To the best of the author's knowledge, no published research has explored the kinetics of prostate-specific EVs interacting with magnetic or other particles in microfluidic devices. The experimental setup demonstrated potential for automation, which could be further enhanced by solving engineering challenges such as magnet removal and multiple flow settings. These advancements could enable scaling into laboratory instruments, reducing reagent costs, improving sample preparation, and ultimately enhancing disease detection.

5. CONCLUSIONS

1. Reaction injection moulding of OSTE 322 and OSTE 220 enables fabrication of hermetically sealed OSTE-COC devices with channel geometry defined by a mould or UV mask, and bonding achieved through O_2 plasma treatment, UV light, and heat. Using 140 µm COC film as substrate enables fabrication of an 800 mm-long mixing module connected to a 4 mm-wide magnetic separation module.
2. A passive zig-zag OSTE-COC micro mixer can be used to achieve a relative mixing index of 0.92, that is comparable to the state of art performance [37]. Reducing channel size from 300 µm to 200 µm and increasing flow rate significantly enhances mixing performance, while varying the zig-zag angle from 14° to 22.5° does not significantly impact mixing index ($p = 0.278$).
3. 3D mixing effects, such as vortices, can be attributed to a combination of Dean vortices and the influence of channel sidewalls, as revealed through confocal microscopy for both zig-zag mixer and 1 mm curved channel.
4. The optimal magnetic configuration for capturing magnetic particles was 18 N45 magnets stacked in alternating polarity. Using this setup, with a 4 mm-wide channel, over 98 % of 70 µg magnetic particles can be captured while using only 26 % of the device's capacity. For higher capacity, the magnetic field strength could be increased by adopting a Halbach array configuration.
5. Extracellular vesicles retain their integrity when subjected to flow rates between 100 and 500 µl/min in the microfluidic magnetic particles capture chamber, as confirmed by qPCR analysis of miRNA375.
6. On-chip capture of LNCaP extracellular vesicles has more consistent western blot signal intensity across a range of flow rates (50–400 µl/min), suggesting that on-chip capture offers a more reliable separation method. However, Off-chip capture yielded higher western blot signal intensity, likely due to longer binding times compared to on-chip.
7. Using a microscopy slide size microfluidic device, CD9-conjugated magnetic particles can be successfully mixed with LNCaP extracellular vesicles, achieving mixing efficiency and binding kinetics comparable to a standard setup. In both configurations, the binding followed asymptotic kinetics described by $f = f_{\infty}[1 - exp(-\sigma t)]$, reaching saturation within 10 minutes, highlighting the device's suitability for rapid and automated EV capture.

REFERENCES

[1] R. Rimsa et al., "Lung on a chip development from off-stoichiometry thiol–ene polymer," *Micromachines (Basel)*, vol. 12, no. 5, 2021, doi: 10.3390/mi12050546.

[2] M. Priedols et al., "Bifurcated Asymmetric Field Flow Fractionation of Nanoparticles in PDMS-Free Microfluidic Devices for Applications in Label-Free Extracellular Vesicle Separation," *Polymers (Basel)*, vol. 15, no. 4, Feb. 2023, doi: 10.3390/polym15040789.

[3] D. Crosby et al., "Early detection of cancer," *Science (1979)*, vol. 375, no. 6586, Mar. 2022, doi: 10.1126/science.aay9040.

[4] J. S. Bonifacino, "Vesicular Transport Earns a Nobel," *Trends Cell Biol*, vol. 24, no. 1, p. 3, Jan. 2014, doi: 10.1016/J.TCB.2013.11.001.

[5] L. Y. Yeo, H. C. Chang, P. P. Y. Chan, and J. R. Friend, "Microfluidic Devices for Bioapplications," *Small*, vol. 7, no. 1, pp. 12–48, Jan. 2011, doi: 10.1002/SMLL.201000946.

[6] R. W. Ruddon, "Cancer biology," p. 544, 2023, Accessed: Sep. 03, 2024. [Online]. Available: https://books.google.com/books/about/Cancer_Biology.html?id=PymZ1ORk0TcC.

[7] "Cancer Today." Accessed: Jun. 19, 2024. [Online]. Available: https://gco.iarc.who.int/today/en/dataviz/bars?mode=cancer&key=total&group_populations=1&types=0_1&sexes=0&sort_by=value1&populations=900&multiple_populations=0&values_position=out&cancers_h=27&age_end=14.

[8] "Cancer." Accessed: Dec. 07, 2023. [Online]. Available: https://www.who.int/news-room/fact-sheets/detail/cancer.

[9] D. T. Debela et al., "New approaches and procedures for cancer treatment: Current perspectives," *SAGE Open Med*, vol. 9, 2021, doi: 10.1177/20503121211034366.

[10] N. Bargahi, S. Ghasemali, S. Jahandar-Lashaki, and A. Nazari, "Recent advances for cancer detection and treatment by microfluidic technology, review and update," *Biological Procedures Online 2022 24:1*, vol. 24, no. 1, pp. 1–20, Apr. 2022, doi: 10.1186/S12575-022-00166-Y.

[11] N. E. Papaioannou, O. V. Beniata, P. Vitsos, O. Tsitsilonis, and P. Samara, "Harnessing the immune system to improve cancer therapy," *Ann Transl Med*, vol. 4, no. 14, pp. 261–261, Jul. 2016, doi: 10.21037/ATM.2016.04.01.

[12] U. Anand et al., "Cancer chemotherapy and beyond: Current status, drug candidates, associated risks and progress in targeted therapeutics," *Genes Dis*, vol. 10, no. 4, p. 1367, Jul. 2023, doi: 10.1016/J.GENDIS.2022.02.007.

[13] C. L. Chaffer and R. A. Weinberg, "A perspective on cancer cell metastasis," *Science (1979)*, vol. 331, no. 6024, pp. 1559–1564, Mar. 2011, doi: 10.1126/SCIENCE.1203543.

[14] "Survival Rates for Prostate Cancer | American Cancer Society." Accessed: Dec. 07, 2023. [Online]. Available: https://www.cancer.org/cancer/types/prostate-cancer/detection-diagnosis-staging/survival-rates.html.

[15] W. J. Catalona et al., "Comparison of Digital Rectal Examination and Serum Prostate Specific Antigen in the Early Detection of Prostate Cancer: Results of a Multicenter Clinical Trial of 6,630 Men," *J Urol*, vol. 151, no. 5, pp. 1283–1290, May 1994, doi: 10.1016/S0022-5347(17)35233-3.

[16] E. P. Gelmann, "Complexities of Prostate-Cancer Risk," *New England Journal of Medicine*, vol. 358, no. 9, pp. 961–963, Feb. 2008, doi: 10.1056/NEJME0708703.

[17] P. Rawla, "Epidemiology of Prostate Cancer," *World J Oncol*, vol. 10, no. 2, p. 63, 2019, doi: 10.14740/WJON1191.

[18] "2020 new cases (incidence) and deaths (mortality) estimates Prostate cancer burden in EU-27", Accessed: Jun. 19, 2024. [Online]. Available: https://cancer-code-europe.iarc.fr.

[19] J. D. Schiffman, P. G. Fisher, and P. Gibbs, "Early Detection of Cancer: Past, Present, and Future," 2015.

[20] N. Pashayan and P. D. P. Pharoah, "The challenge of early detection in cancer," *Science (1979)*, vol. 368, no. 6491, pp. 589–590, May 2020, doi: 10.1126/SCIENCE.AAZ2078.

[21] V. A. Moyer, "Screening for prostate cancer: U.S. Preventive Services Task Force recommendation statement," *Ann Intern Med*, vol. 157, no. 2, pp. 120–134, 2012, doi: 10.7326/0003-4819-157-2-201207170-00459.

[22] G. T. Kennedy et al., "Targeted detection of cancer at the cellular level during biopsy by near-infrared confocal laser endomicroscopy," *Nature Communications 2022 13:1*, vol. 13, no. 1, pp. 1–9, May 2022, doi: 10.1038/s41467-022-30265-z.

[23] M. J. Ijzerman et al., "Towards Routine Implementation of Liquid Biopsies in Cancer Management: It Is Always Too Early, until Suddenly It Is Too Late," *Diagnostics 2021, Vol. 11, Page 103*, vol. 11, no. 1, p. 103, Jan. 2021, doi: 10.3390/DIAGNOSTICS11010103.

[24] M. Ramirez-Garrastacho et al., "Extracellular vesicles as a source of prostate cancer biomarkers in liquid biopsies: a decade of research," *British Journal of Cancer 2021 126:3*, vol. 126, no. 3, pp. 331–350, Nov. 2021, doi: 10.1038/s41416-021-01610-8.

[25] W. H. Chang, R. A. Cerione, and M. A. Antonyak, "Extracellular Vesicles and Their Roles in Cancer Progression," *Methods Mol Biol*, vol. 2174, p. 143, 2021, doi: 10.1007/978-1-0716-0759-6_10.

[26] R. Kalluri and V. S. LeBleu, "The biology, function, and biomedical applications of exosomes," *Science (1979)*, vol. 367, no. 6478, Feb. 2020, doi: 10.1126/SCIENCE.AAU6977.

[27] "The Cost of Sequencing a Human Genome." Accessed: Jun. 20, 2024. [Online]. Available: https://www.genome.gov/about-genomics/fact-sheets/Sequencing-Human-Genome-cost.

[28] F. Cheng, L. Su, and C. Qian, "Circulating tumor DNA: a promising biomarker in the liquid biopsy of cancer," vol. 7, no. 30, Accessed: Jun. 20, 2024. [Online]. Available: www.impactjournals.com/oncotarget

[29] F. Diehl et al., "Circulating mutant DNA to assess tumor dynamics," *Nature Medicine 2008 14:9*, vol. 14, no. 9, pp. 985–990, Jul. 2008, doi: 10.1038/nm.1789.

[30] H. Shao, H. Im, C. M. Castro, X. Breakefield, R. Weissleder, and H. Lee, "New Technologies for Analysis of Extracellular Vesicles," *Chem Rev*, vol. 118, no. 4, pp. 1917–1950, Feb. 2018, doi: 10.1021/acs.chemrev.7b00534.

[31] M. A. Livshts et al., "Isolation of exosomes by differential centrifugation: Theoretical analysis of a commonly used protocol," *Sci Rep*, vol. 5, Nov. 2015, doi: 10.1038/srep17319.

[32] F. Momen-Heravi, "Isolation of Extracellular Vesicles by Ultracentrifugation," *Methods Mol Biol*, vol. 1660, pp. 25–32, 2017, doi: 10.1007/978-1-4939-7253-1_3.

[33] D. W. Greening and R. J. Simpson, "Understanding extracellular vesicle diversity – current status," *Expert Rev Proteomics*, vol. 15, no. 11, pp. 887–910, Nov. 2018, doi: 10.1080/14789450.2018.1537788.

[34] K. Rekker et al., "Comparison of serum exosome isolation methods for microRNA profiling," *Clin Biochem*, vol. 47, no. 1–2, pp. 135–138, Jan. 2014, doi: 10.1016/J.CLINBIOCHEM.2013.10.020.

[35] M. L. Alvarez, M. Khosroheidari, R. Kanchi Ravi, and J. K. Distefano, "Comparison of protein, microRNA, and mRNA yields using different methods of urinary exosome isolation for the discovery of kidney disease biomarkers," *Kidney Int*, vol. 82, no. 9, pp. 1024–1032, Nov. 2012, doi: 10.1038/KI.2012.256.

[36] E. Reátegui et al., "Engineered nanointerfaces for microfluidic isolation and molecular profiling of tumor-specific extracellular vesicles", doi: 10.1038/s41467-017-02261-1.

[37] C. Y. Lee, W. T. Wang, C. C. Liu, and L. M. Fu, "Passive mixers in microfluidic systems: A review," Mar. 15, 2016, *Elsevier*. doi: 10.1016/j.cej.2015.10.122.

[38] M. T. Guo, A. Rotem, J. A. Heyman, and D. A. Weitz, "Droplet microfluidics for high-throughput biological assays," *Lab Chip*, vol. 12, no. 12, pp. 2146–2155, May 2012, doi: 10.1039/C2LC21147E.

[39] J. Shuga et al., "Single molecule quantitation and sequencing of rare translocations using microfluidic nested digital PCR", doi: 10.1093/nar/gkt613.

[40] Y. Wang et al., "Microfluidic Raman biochip detection of exosomes: A promising tool for prostate cancer diagnosis," *Lab Chip*, vol. 20, no. 24, pp. 4632–4637, Dec. 2020, doi: 10.1039/d0lc00677g.

[41] D. R. Deans, "A new technique for heart cutting in gas chromatography [1]," *Chromatographia*, vol. 1, no. 1–2, pp. 18–22, Jan. 1968, doi: 10.1007/BF02259005.

[42] W. Menz and A. Guber, "Microstructure technologies and their potential in medical applications," *Minimally Invasive Neurosurgery*, vol. 37, no. 1, pp. 21–27, Jan. 1994, doi: 10.1055/s-2008-1053444.

[43] L. A. Low, C. Mummery, B. R. Berridge, C. P. Austin, and D. A. Tagle, "Organs-on-chips: into the next decade," *Nature Reviews Drug Discovery 2020 20:5*, vol. 20, no. 5, pp. 345–361, Sep. 2020, doi: 10.1038/s41573-020-0079-3.

[44] T. Moragues et al., "Droplet-based microfluidics," *Nature Reviews Methods Primers 2023 3 : 1*, vol. 3, no. 1, pp. 1–22, Apr. 2023, doi: 10.1038/s43586-023-00212-3.

[45] P. Neužil, S. Giselbrecht, K. Länge, T. J. Huang, and A. Manz, "Revisiting lab-on-a-chip technology for drug discovery," *Nature Reviews Drug Discovery 2012 11 : 8*, vol. 11, no. 8, pp. 620–632, Aug. 2012, doi: 10.1038/nrd3799.

[46] J. Zhuang, J. Yin, S. Lv, B. Wang, and Y. Mu, "Advanced 'lab-on-a-chip' to detect viruses – Current challenges and future perspectives," *Biosens Bioelectron*, vol. 163, p. 112291, Sep. 2020, doi: 10.1016/J.BIOS.2020.112291.

[47] T. E. Gildner, G. N. Eick, A. L. Schneider, F. C. Madimenos, and J. J. Snodgrass, "After Theranos: Using point-of-care testing to advance measures of health biomarkers in human biology research," *American Journal of Human Biology*, vol. 34, no. 11, p. e23689, Nov. 2022, doi: 10.1002/AJHB.23689.

[48] A. Jennings, "Theranos: Case Study and Examination of the Fraud Triangle Theranos: Case Study and Examination of the Fraud Triangle Human Resources Management Commons, Labor Relations Commons, Legal Ethics and Professional Responsibility Commons, and the Securities Law Commons", Accessed: Feb. 04, 2025. [Online]. Available: https://scholarworks.uark.edu/finnuht/72

[49] Y. Chen, K. Wang, Z. Liu, R. Sun, D. Cui, and J. He, "Rapid detection and quantification of tumor marker carbohydrate antigen 72-4 (CA72-4) using a superparamagnetic immunochromatographic strip," *Anal Bioanal Chem*, vol. 408, no. 9, pp. 2319–2327, Mar. 2016, doi: 10.1007/S00216-016-9328-Z.

[50] W. Lu et al., "Dual Immunomagnetic Nanobeads-Based Lateral Flow Test Strip for Simultaneous Quantitative Detection of Carcinoembryonic Antigen and Neuron Specific Enolase," *Scientific Reports 2017 7:1*, vol. 7, no. 1, pp. 1–10, Feb. 2017, doi: 10.1038/srep42414.

[51] D. C. Duffy, J. C. McDonald, O. J. A. Schueller, and G. M. Whitesides, "Rapid prototyping of microfluidic systems in poly(dimethylsiloxane)," *Anal Chem*, vol. 70, no. 23, pp. 4974–4984, Dec. 1998, doi: 10.1021/ac980656z.

[52] D. B. Weibel, W. R. DiLuzio, and G. M. Whitesides, "Microfabrication meets microbiology," *Nature Reviews Microbiology 2007 5:3*, vol. 5, no. 3, pp. 209–218, Mar. 2007, doi: 10.1038/nrmicro1616.

[53] D. Huh, B. D. Matthews, A. Mammoto, M. Montoya-Zavala, H. Yuan Hsin, and D. E. Ingber, "Reconstituting organ-level lung functions on a chip," *Science (1979)*, vol. 328, no. 5986, pp. 1662–1668, Jun. 2010, doi: 10.1126/SCIENCE.1188302.

[54] A. M. Kemas et al., "Compound Absorption in Polymer Devices Impairs the Translatability of Preclinical Safety Assessments," *Adv Healthc Mater*, 2023, doi: 10.1002/adhm.202303561.

[55] S. Aralekallu, R. Boddula, and V. Singh, "Development of glass-based microfluidic devices: A review on its fabrication and biologic applications," *Mater Des*, vol. 225, p. 111517, Jan. 2023, doi: 10.1016/J.MATDES.2022.111517.

[56] J. Hwang, Y. H. Cho, M. S. Park, and B. H. Kim, "Microchannel Fabrication on Glass Materials for Microfluidic Devices," *International Journal of Precision Engineering and Manufacturing*, vol. 20, no. 3, pp. 479–495, Mar. 2019, doi: 10.1007/S12541-019-00103-2.

[57] N. Keller et al., "Tacky cyclic olefin copolymer: a biocompatible bonding technique for the fabrication of microfluidic channels in COC," *Lab Chip*, vol. 16, no. 9, pp. 1561–1564, Apr. 2016, doi: 10.1039/C5LC01498K.

[58] C. F. Carlborg, T. Haraldsson, K. Öberg, M. Malkoch, and W. Van Der Wijngaart, "Beyond PDMS: off-stoichiometry thiol–ene (OSTE) based soft lithography for rapid prototyping of microfluidic devices," *Lab Chip*, vol. 11, no. 18, pp. 3136–3147, Sep. 2011, doi: 10.1039/C1LC20388F.

[59] A. Agha et al., "A Review of Cyclic Olefin Copolymer Applications in Microfluidics and Microdevices," *Macromol Mater Eng*, vol. 307, no. 8, Aug. 2022, doi: 10.1002/mame.202200053.

[60] D. J. Guckenberger, T. E. De Groot, A. M. D. Wan, D. J. Beebe, and E. W. K. Young, "Micromilling: A method for ultra-rapid prototyping of plastic microfluidic devices," *Lab Chip*, vol. 15, no. 11, pp. 2364–2378, Jun. 2015, doi: 10.1039/c5lc00234f.

[61] H. Sun, Y. Jia, H. Dong, D. Dong, and J. Zheng, "Combining additive manufacturing with microfluidics: an emerging method for developing novel organs-on-chips," *Curr Opin Chem Eng*, vol. 28, pp. 1–9, Jun. 2020, doi: 10.1016/J.COCHE.2019.10.006.

[62] "Elegoo Mars 5 Ultra – Best Beginner's Dream Resin 3D Printer – ELEGOO EU." Accessed: Nov. 07, 2024. [Online]. Available: https://eu.elegoo.com/products/mars-5-ultra-9k-7inch-monochrome-lcd-resin-3d-printer

[63] A. V. Nielsen, M. J. Beauchamp, G. P. Nordin, and A. T. Woolley, "3D Printed Microfluidics," *Annual Review of Analytical Chemistry*, vol. 13, no. Volume 13, 2020, pp. 45–65, Jun. 2020, doi: 10.1146/annurev-anchem-091619-102649.

[64] P. G. Huray, *Maxwell's Equations*. John Wiley and Sons, 2011. doi: 10.1002/9780470549919.

[65] E. Richard. Cohen, D. R. . Lide, and G. L. . Trigg, "Physics desk reference," p. 888, 2003, Accessed: Sep. 09, 2024. [Online]. Available: https://search.worldcat.org/title/1014869378

[66] Q. Cao, X. Han, and L. Li, "Configurations and control of magnetic fields for manipulating magnetic particles in microfluidic applications: Magnet systems and manipulation mechanisms," Aug. 07, 2014, *Royal Society of Chemistry*. doi: 10.1039/c4lc00367e.

[67] J. M. D. Coey, *Magnetism and Magnetic Materials*. Cambridge University Press, 2001. doi: 10.1017/CBO9780511845000.

[68] D. J. Pike, N. Kapur, P. A. Millner, and D. I. Stewart, "Flow Cell Design for Effective Biosensing," *Sensors 2013, Vol. 13, Pages 58-70*, vol. 13, no. 1, pp. 58–70, Dec. 2012, doi: 10.3390/S130100058.

[69] "Halbach Arrays | K&J Magnetics Blog." Accessed: Aug. 28, 2024. [Online]. Available: https://www.kjmagnetics.com/blog.asp?p=halbach-arrays

[70] K. Halbach, "Design of permanent multipole magnets with oriented rare earth cobalt material," *Nuclear Instruments and Methods*, vol. 169, no. 1, pp. 1–10, Feb. 1980, doi: 10.1016/0029-554X(80)90094-4.

[71] O. Reynolds, "An Experimental Investigation of the Circumstances Which Determine Whether the Motion of Water Shall Be Direct or Sinuous, and of the Law of Resistance in Parallel Channels," *Source: Philosophical Transactions of the Royal Society of London*, vol. 174, pp. 935–982, 1883.

[72] "Reynolds Number." Accessed: Aug. 19, 2024. [Online]. Available: https://www.engineeringtoolbox.com/reynolds-number-d_237.html

[73] B. E. Rapp, "Analytical Solutions to Poiseuille Flow Problems in Different Geometries," *Microfluidics: Modelling, Mechanics and Mathematics*, pp. 323–349, Jan. 2017, doi: 10.1016/B978-1-4557-3141-1.50016-2.

[74] O. Ostroverkhova, "Handbook of Organic Materials for Electronic and Photonic Devices, Second Edition," *Handbook of Organic Materials for Electronic and Photonic Devices, Second Edition*, pp. 1–891, Jan. 2018, doi: 10.1016/C2016-0-05254-3.

[75] Dill Ken A. and Bromberg Sarina, "Molecular Driving Forces: Statistical Thermodynamics in Chemistry and Biology." Accessed: Aug. 07, 2024. [Online]. Available: https://books.google.lv/books?id=hdeODhjp1bUC&pg=PA327&redir_esc=y#v=onepage&q&f=false.

[76] Einstein Albert, "On the movement of small particles suspended in a stationary liquid demanded by the molecular-kinetic theory of heat," *Ann Phys*, pp. 549–560, 1905.

[77] C. T. Culbertson, S. C. Jacobson, and J. Michael Ramsey, "Diffusion coefficient measurements in microfluidic devices," *Talanta*, vol. 56, no. 2, pp. 365–373, Feb. 2002, doi: 10.1016/S0039-9140(01)00602-6.

[78] C.-Y. Lee, C.-L. Chang, Y.-N. Wang, and L.-M. Fu, "Microfluidic Mixing: A Review," *International Journal of Molecular Sciences 2011, Vol. 12, Pages 3263-3287*, vol. 12, no. 5, pp. 3263–3287, May 2011, doi: 10.3390/IJMS12053263.

[79] Z. Yang, S. Matsumoto, H. Goto, M. Matsumoto, and R. Maeda, "Ultrasonic micromixer for microfluidic systems," *Sens Actuators A Phys*, vol. 93, no. 3, pp. 266–272, Oct. 2001, doi: 10.1016/S0924-4247(01)00654-9.

[80] T. R. Tsao, R. M. Moroney, B. A. Martin, and R. M. White, "Electrochemical detection of localized mixing produced by ultrasonic flexural waves," *Proc IEEE Ultrason Symp*, pp. 937–940, 1991, doi: 10.1109/ULTSYM.1991.234251.

[81] J. C. Rife, M. I. Bell, J. S. Horwitz, M. N. Kabler, R. C. Y. Auyeung, and W. J. Kim, "Miniature valveless ultrasonic pumps and mixers," *Sens Actuators A Phys*, vol. 86, no. 1–2, pp. 135–140, Oct. 2000, doi: 10.1016/S0924-4247(00)00433-7.

[82] C. Y. Lee, G. Bin Lee, L. M. Fu, K. H. Lee, and R. J. Yang, "Electrokinetically driven active micro-mixers utilizing zeta potential variation induced by field effect," *Journal of Micromechanics and Microengineering*, vol. 14, no. 10, p. 1390, Jul. 2004, doi: 10.1088/0960-1317/14/10/014.

[83] Z. Wu and D. Li, "Micromixing using induced-charge electrokinetic flow," *Electrochim Acta*, vol. 53, no. 19, pp. 5827–5835, Aug. 2008, doi: 10.1016/J.ELECTACTA.2008.03.039.

[84] C. Huang and C. Tsou, "The implementation of a thermal bubble actuated microfluidic chip with microvalve, micropump and micromixer," *Sens Actuators A Phys*, vol. 210, pp. 147–156, Apr. 2014, doi: 10.1016/J.SNA.2014.02.015.

[85] C. Huang and C. Tsou, "The implementation of a thermal bubble actuated microfluidic chip with microvalve, micropump and micromixer," *Sens Actuators A Phys*, vol. 210, pp. 147–156, Apr. 2014, doi: 10.1016/J.SNA.2014.02.015.

[86] Y. Wang, J. Zhe, B. T. F. Chung, and P. Dutta, "A rapid magnetic particle driven micromixer," *Microfluid Nanofluidics*, vol. 4, no. 5, pp. 375–389, May 2008, doi: 10.1007/S10404-007-0188-X.

[87] Q. Xiong et al., "Magnetic nanochain integrated microfluidic biochips," *Nature Communications 2018 9:1*, vol. 9, no. 1, pp. 1–11, May 2018, doi: 10.1038/s41467-018-04172-1.

[88] X. Niu and Y. K. Lee, "Efficient spatial-temporal chaotic mixing in microchannels," *Journal of Micromechanics and Microengineering*, vol. 13, no. 3, p. 454, Apr. 2003, doi: 10.1088/0960-1317/13/3/316.

[89] T. Tofteberg, M. Skolimowski, E. Andreassen, and O. Geschke, "A novel passive micromixer: Lamination in a planar channel system," *Microfluid Nanofluidics*, vol. 8, no. 2, pp. 209–215, Feb. 2010, doi: 10.1007/S10404-009-0456-Z.

[90] M. Roudgar, E. Brunazzi, C. Galletti, and R. Mauri, "Numerical Study of Split T-Micromixers," *Chem Eng Technol*, vol. 35, no. 7, pp. 1291–1299, Jul. 2012, doi: 10.1002/CEAT.201100611.

[91] N. Ait Mouheb, D. Malsch, A. Montillet, C. Solliec, and T. Henkel, "Numerical and experimental investigations of mixing in T-shaped and cross-shaped micromixers," *Chem Eng Sci*, vol. 68, no. 1, pp. 278–289, Jan. 2012, doi: 10.1016/J.CES.2011.09.036.

[92] J. Li, G. Xia, and Y. Li, "Numerical and experimental analyses of planar asymmetric split-and-recombine micromixer with dislocation sub-channels," *Journal of Chemical Technology & Biotechnology*, vol. 88, no. 9, pp. 1757–1765, Sep. 2013, doi: 10.1002/JCTB.4044.

[93] M. A. Ansari and K. Y. Kim, "Mixing performance of unbalanced split and recombine micomixers with circular and rhombic sub-channels," *Chemical Engineering Journal*, vol. 162, no. 2, pp. 760–767, Aug. 2010, doi: 10.1016/J.CEJ.2010.05.068.

[94] A. Afzal and K. Y. Kim, "Passive split and recombination micromixer with convergent–divergent walls," *Chemical Engineering Journal*, vol. 203, pp. 182–192, Sep. 2012, doi: 10.1016/J.CEJ.2012.06.111.

[95] M. Khosravi Parsa, F. Hormozi, and D. Jafari, "Mixing enhancement in a passive micromixer with convergent-divergent sinusoidal microchannels and different ratio of amplitude to wave length," *Comput Fluids*, vol. 105, pp. 82–90, Dec. 2014, doi: 10.1016/j.compfluid.2014.09.024.

[96] Y. Lin, X. Yu, Z. Wang, S. T. Tu, and Z. Wang, "Design and evaluation of an easily fabricated micromixer with three-dimensional periodic perturbation," *Chemical Engineering Journal*, vol. 171, no. 1, pp. 291–300, Jun. 2011, doi: 10.1016/J.CEJ.2011.04.003.

[97] J. Yang, L. Qi, Y. Chen, and H. Ma, "Design and Fabrication of a Three Dimensional Spiral Micromixer," *Chin J Chem*, vol. 31, no. 2, pp. 209–214, Feb. 2013, doi: 10.1002/CJOC.201200922.

[98] Y. Du, Z. Zhang, C. H. Yim, M. Lin, and X. Cao, "Evaluation of Floor-grooved Micromixers using Concentration-channel Length Profiles," *Micromachines 2010, Vol. 1, Pages 19-33*, vol. 1, no. 1, pp. 19–33, May 2010, doi: 10.3390/MI1010019.

[99] C. A. Cortes-Quiroz, A. Azarbadegan, M. Zangeneh, and A. Goto, "Analysis and multi-criteria design optimization of geometric characteristics of grooved micromixer," *Chemical Engineering Journal*, vol. 160, no. 3, pp. 852–864, Jun. 2010, doi: 10.1016/J.CEJ.2010.02.029.

[100] J. Cha et al., "A highly efficient 3D micromixer using soft PDMS bonding," *Journal of Micromechanics and Microengineering*, vol. 16, no. 9, pp. 1778–1782, Sep. 2006, doi: 10.1088/0960-1317/16/9/004.

[101] O. Jännig and N. T. Nguyen, "A polymeric high-throughput pressure-driven micromixer using a nanoporous membrane," *Microfluid Nanofluidics*, vol. 10, no. 3, pp. 513–519, Mar. 2011, doi: 10.1007/s10404-010-0685-1.

[102] S. Sivashankar, S. Agambayev, Y. Mashraei, E. Q. Li, S. T. Thoroddsen, and K. N. Salama, "A 'twisted' microfluidic mixer suitable for a wide range of flow rate applications," *Biomicrofluidics*, vol. 10, no. 3, May 2016, doi: 10.1063/1.4954812.

[103] S. Arockiam, Y. H. Cheng, P. M. Armenante, and S. Basuray, "Experimental determination and computational prediction of the mixing efficiency of a simple, continuous,

serpentine-channel microdevice," *Chemical Engineering Research and Design*, vol. 167, pp. 303–317, Mar. 2021, doi: 10.1016/j.cherd.2021.01.022.

[104] R. H. Liu et al., "Passive mixing in a three-dimensional serpentine microchannel," *Journal of Microelectromechanical Systems*, vol. 9, no. 2, pp. 190–197, Jun. 2000, doi: 10.1109/84.846699.

[105] A. Hashmi and J. Xu, "On the quantification of mixing in microfluidics," *J Lab Autom*, vol. 19, no. 5, pp. 488–491, Oct. 2014, doi: 10.1177/2211068214540156.

[106] B. Stoeber, D. Liepmann, and S. J. Muller, "Strategy for active mixing in microdevices," *Phys Rev E*, vol. 75, no. 6, p. 066314, Jun. 2007, doi: 10.1103/PhysRevE.75.066314.

[107] S. Wang, X. Huang, and C. Yang, "Mixing enhancement for high viscous fluids in a microfluidic chamber," *Lab Chip*, vol. 11, no. 12, pp. 2081–2087, Jun. 2011, doi: 10.1039/C0LC00695E.

[108] H. M. Xia, Z. P. Wang, W. Wang, W. Fan, A. Wijaya, and Z. F. Wang, "Aeroelasticity-based fluid agitation for lab-on-chips," *Lab Chip*, vol. 13, no. 8, pp. 1619–1625, Mar. 2013, doi: 10.1039/C3LC41346B.

[109] D. Sinton, "Microscale flow visualization," Nov. 2004. doi: 10.1007/s10404-004-0009-4.

[110] A. K. Tieu, M. R. Mackenzie, and E. B. Li, "Measurements in microscopic flow with a solid-state LDA," *Exp Fluids*, vol. 19, no. 4, pp. 293–294, Aug. 1995, doi: 10.1007/BF00196478.

[111] M. H. Oddy, J. G. Santiago, and J. C. Mikkelsen, "Electrokinetic Instability Micromixing," *Anal Chem*, vol. 73, no. 24, pp. 5822–5832, Dec. 2001, doi: 10.1021/AC0155411.

[112] R. D. Keane, R. J. Adrian, and Y. Zhang, "Super-resolution particle imaging velocimetry," *Meas Sci Technol*, vol. 6, no. 6, p. 754, Jun. 1995, doi: 10.1088/0957-0233/6/6/013.

[113] C. D. Meinhart, S. T. Wereley, and J. G. Santiago, "Micron-Resolution Velocimetry Techniques," *Laser Techniques Applied to Fluid Mechanics*, pp. 57–70, 2000, doi: 10.1007/978-3-642-56963-0_4.

[114] E. Biddiss, D. Erickson, and D. Li, "Heterogeneous Surface Charge Enhanced Micromixing for Electrokinetic Flows," *Anal Chem*, vol. 76, no. 11, pp. 3208–3213, Jul. 2004, doi: 10.1021/AC035451R.

[115] S. C. Jacobson, C. T. Culbertson, J. E. Daler, and J. M. Ramsey, "Microchip Structures for Submillisecond Electrophoresis," *Anal Chem*, vol. 70, no. 16, pp. 3476–3480, Aug. 1998, doi: 10.1021/AC980349T.

[116] B. Mosier, J. Molho, and J. Santiago, "Photobleached-fluorescence imaging of microflows," *Exp Fluids*, vol. 33, no. 4, pp. 545–554, 2002, doi: 10.1007/S00348-002-0486-8.

[117] R. E. Falco, C. C. Chu, R. E. Falco, and C. C. Chu, "Measurement of two-dimensional fluid dynamic quantities using a photochromic grid tracing technique," *SPIE*, vol. 814, pp. 706–710, 1988, Accessed: Aug. 14, 2024. [Online]. Available: https://ui.adsabs.harvard.edu/abs/1988SPIE..814..706F/abstract

[118] D. Maynes and A. R. Webb, "Velocity profile characterization in sub-millimeter diameter tubes using molecular tagging velocimetry," *Exp Fluids*, vol. 32, no. 1, pp. 3–15, Jan. 2002, doi: 10.1007/S003480200001.

[119] T. J. Mitchison, K. E. Sawin, J. A. Theriot, K. Gee, and A. Mallavarapu, "[4] Caged fluorescent probes," *Methods Enzymol*, vol. 291, pp. 63–78, Jan. 1998, doi: 10.1016/S0076-6879(98)91007-2.

[120] J. Chung, Y. Shin, K. Petigrew, P. Chapman, C. P. Grigoropoulos, and R. Greif, "Infrared thermal velocimetry for nonintrusive flow measurement in silicon microfluidic devices," *Review of Scientific Instruments*, vol. 74, no. 5, pp. 2911–2917, May 2003, doi: 10.1063/1.1569397.

[121] R. Lindken, J. Westerweel, and B. Wieneke, "Stereoscopic micro particle image velocimetry," *Exp Fluids*, vol. 41, no. 2, pp. 161–171, Aug. 2006, doi: 10.1007/S00348-006-0154-5.

[122] C. J. Kähler et al., "Main results of the 4th International PIV Challenge," *Exp Fluids*, vol. 57, no. 6, pp. 1–71, Jun. 2016, doi: 10.1007/S00348-016-2173-1.

[123] C. Cierpka, M. Rossi, R. Segura, and C. J. Kähler, "On the calibration of astigmatism particle tracking velocimetry for microflows," *Meas Sci Technol*, vol. 22, no. 1, 2011, doi: 10.1088/0957-0233/22/1/015401.

[124] A. P. Sudarsan and V. M. Ugaz, "Multivortex micromixing," 2006. [Online]. Available: www.pnas.orgcgidoi10.1073pnas.0507976103

[125] W. Rösing, T. Schildhauer, J. König, and C. Cierpka, "Passive control of the concentration boundary layer in microfluidic fuel cells using Dean vortices," *Microfluid Nanofluidics*, vol. 23, no. 9, Sep. 2019, doi: 10.1007/s10404-019-2274-2.

[126] Ito H., Willson C.G., and Frechet J.H.J., "New UV Resists with Negative or Positive Tone," Oiso, 1982. Accessed: Aug. 19, 2024. [Online]. Available: https://ieeexplore.ieee.org/document/4480589

[127] H. Towbin, "Western Blotting," *Encyclopedia of Immunology*, pp. 2503–2507, Jan. 1998, doi: 10.1006/RWEI.1999.0633.

[128] G. Adams, "A beginner's guide to RT-PCR, qPCR and RT-qPCR," *Biochem (Lond)*, vol. 42, no. 3, pp. 48–53, Jun. 2020, doi: 10.1042/BIO20200034.

[129] W. Rösing, T. Schildhauer, J. König, and C. Cierpka, "Passive control of the concentration boundary layer in microfluidic fuel cells using Dean vortices," *Microfluid Nanofluidics*, vol. 23, no. 9, Sep. 2019, doi: 10.1007/s10404-019-2274-2.

[130] A. Cosentino, H. Madadi, P. Vergara, R. Vecchione, F. Causa, and P. A. Netti, "An efficient planar accordion-shaped micromixer: from biochemical mixing to biological application," *Scientific Reports 2015 5:1*, vol. 5, no. 1, pp. 1–10, Dec. 2015, doi: 10.1038/srep17876.

[131] D. F. Swinehart, "The Beer-Lambert Law," *J Chem Educ*, vol. 39, no. 7, pp. 333–335, 1962, doi: 10.1021/ED039P333.

[132] S. H. Wong, P. Bryant, M. Ward, and C. Wharton, "Investigation of mixing in a cross-shaped micromixer with static mixing elements for reaction kinetics studies," *Sens Actuators B Chem*, vol. 95, no. 1–3, pp. 414–424, Oct. 2003, doi: 10.1016/S0925-4005(03)00447-7.

[133] J. Cipa et al., "OSTE DEVICE FOR MAGNETIC PARTICLE CAPTURE," *MicroTAS 2022 – 26th International Conference on Miniaturized Systems for Chemistry and Life Sciences*, pp. 919–920, Jan. 2022.

[134] "Magnet Grades | K&J Magnetics Blog." Accessed: Sep. 02, 2024. [Online]. Available: https://www.kjmagnetics.com/blog.asp?p=magnet-grade

[135] J. Cipa et al., "Elucidating Extracellular Vesicle Isolation Kinetics via an Integrated Off-Stoichiometry Thiol-Ene and Cyclic Olefin Copolymer Microfluidic Device," 2024, doi: 10.3390/polym16243579.

[136] S. Stael, L. P. Miller, Á. D. Fernández-Fernández, and F. Van Breusegem, "Detection of Damage-Activated Metacaspase Activity by Western Blot in Plants," *Methods in Molecular Biology*, vol. 2447, pp. 127–137, 2022, doi: 10.1007/978-1-0716-2079-3_11.

[137] Caltag, "Exosome-Human CD63 Isolation/Detection (from cell culture media) Protocol for use in Flow Cytometry Product Description", Accessed: Nov. 09, 2023. [Online]. Available: www.lifetechnologies.com/support.

[138] L. Technologies, "Exosome-Human CD9 Isolation (from cell culture) Pre-enriched exosome sample input," 2014. [Online]. Available: www.lifetechnologies.com/support.

ACKNOWLEDGEMENTS

The author wishes to express sincere gratitude to the Latvian Biomedical Research and Study Centre, particularly to **Edgars Endzelins** and the **Aija Line** group, for their invaluable contributions in producing extracellular vesicles (EVs) and magnetic particle (MP) conjugate nanobodies. Their assistance in conducting experiments, including iron content analysis, Western blot, and qPCR measurements, as well as performing the standard assay control experiments, was instrumental to this research.

The author is also thankful to colleagues at **Cellbox Labs** and the Institute of **Solid State Physics** for their insightful discussions and guidance regarding the fabrication and testing processes of the microfluidic devices, most notably **Roberts Rimsa** for the PhD mentorship.

Additionally, the author acknowledges the University of Latvia for providing the opportunity to conduct PhD research within the "Natural Sciences (Physics, Astronomy and Mechanics) Academic Doctor" program.

Finally, the author expresses appreciation to the founding agency for their support throughout this research project: Project was funded by European Regional Development Fund (ERDF), Measure 1.1.1.1 "Support for applied research" No 1.1.1.1/20/A/045, "Development of a novel microfluidic device for label-free quantification of prostate cancer-derived extracellular vesicles and analysis of their RNA content (PROCEX)" The financial support of Latvian Council of Science project VPP-EM-FOTONIKA-2022/1-0001 "Smart Materials, Photonics, Technologies, and Engineering Ecosystems is apricated

USE OF LARGE LANGUAGE MODELS

In the writing process of this dissertation large language models were used as text editing and improvement tools. Specifically, MS word, word suggestion was used. Additionally chat GPT 3, GPT 4 and GPT 4o were used exclusively for improving the text flow. Importantly no text was generated without prewritten text made by author and all statements made in the dissertation are solely authors responsibility.

Most used prompt was: "I will provide you with a text and you will improve it, keeping it neutral and in a scientific publication style. you will not use word significant, and keep the over promising to a minim as its in scientific publications"

APPENDIX

OSTE DEVICE FOR MAGNETIC PARTICLE CAPTURE

Janis Cipa[1,2], Edgars Endzelins[3], Roberts Rimsa[2], Artis Galvanovskis[3], Arturs Abols [2,3], Aija Line[3] and Gatis Mozolevskis[2]

[1]University of Latvia, Faculty of Physics, Mathematics and Optometry, Jelgavas street 3, Riga, Latvia
[2]Cellboxlab Ltd., Kengaraga street 8, LV-1063, Riga, Latvia
[3]Latvian Biomedical research and study centre, Ratsupites Str. 1 k-1,Riga, LV-106, Latvia

ABSTRACT

Extracellular vesicles (EVs) are a valuable source of cancer-derived biomarkers in liquid biopsies, however their use is hampered by low concentration of cancer derived EVs in biofluids. Development of technologies that allow the EV analysis directly in a sample of biofluid without a prior EV isolation would significantly advance their clinical application. Herein, we present a highly efficient off-stoichiometry thiol-ene (OSTE) polymer microfluidic device module that can be used for capture of EVs bound to antibody-conjugated magnetic particles.

KEYWORDS: Off-Stoichiometry Thiol-ene, Microfluidics, Magnetic Particles, Extracellular Vesicles

INTRODUCTION

Early detection and diagnostics is the key towards increased prostate cancer survival [1]. EVs are a promising source of cancer-derived biomarkers for liquid biopsies [2], however, only a few EV-based tests have reached clinics. One of the main challenges is the lack of efficient, robust and reproducible method for the isolation of cancer-derived EVs. To address this issue, we set out to develop a microfluidics-based device for capturing and analysis of cancer-derived EVs directly from a sample of biofluid such as blood or urine. Well known materials such as polydimethylsiloxane (PDMS) cannot be used due to their small, hydrophobic molecule absorption [3]. Thus, we propose use of OSTE polymers to fabricate microfluidic devices owing to its superior properties. These devices can significantly improve EV isolation and capture by magnetic beads compared to PDMS in terms of reducing background noise coming from small molecular absorption and leakage [4]. In this report, we demonstrate EV capture using functionalized magnetic nanoparticles (MP) in a OSTE microfluidics device.

EXPERIMENTAL

OSTE-COC (cyclo-olefin copolymer) devices were fabricated using casting method, that involves 3D printed mold, PDMS negative, and casted layer of OSTE in PDMS mold (see Fig. 1A, for device cross-section), using this method hermetic channel fabrication yield was approximately 50%. After preliminary experiments, alternative fabrication method was developed for COC-OSTE-Glass device (Fig. 1B) which was fabricated in 3 steps: firstly 3D printed molds with the desired design (Fig. 1C) were printed using UV curable resin. Secondly, SORTA-Clear 18 silicone molds were created by pouring material in printed molds and followed by curing at 60°C for 12h. Thirdly, SORTA-Clear 18 molds were sealed against the glass slide and filled with OSTE 322 (supplied by Mercene Labs) as seen in Fig. 1B. After which, COC slide with mini-luer ports was aligned and placed on top of the OSTE layer, thus capping the device. Finally, device was cured overnight under 20N pressure. By using this method it was possible to create multiple devices with channel yield of 97.5% with channel dimensions of 18 x 0.4-8 x 0.2mm. MP capture was realized with two experimental setups: 15, 8x5x5mm N45 magnet or single N52 magnet. Commercially available 1µm MPs (Dynabeads™ MyOne™ Carboxylic Acid, ThermoFisher) were conjugated with anti-CD63 antibodies and incubated with EVs produced by prostate cancer cell lines PC3 and LNCaP. MP capture was tested based on channel aspect ratio (AR) and magnet configuration and EV structural integrity was evaluated with respect to flow rate. Post-capture EVs-containing MPs were treated with QIAzol lysis solution spiked with UniSp6, followed by RNA extraction (miRNeasy Micro kit, Qiagen) and cDNA synthesis (miRCURY LNA RT Kit, Qiagen). Relative quantities of miR-375 and UniSp6 RNA in each sample were determined by quantitative polymerase chain reaction (qPCR). MiR-375 levels were first normalized against UniSp6, then against the total amount of captured MPs (quantified by iron content).

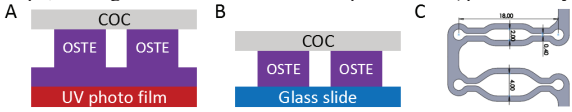

Figure 1: OSTE-COC device 2d schematic (A) COC-OSTE-Glass device 2d schematic (B), sequential design example (C).

RESULTS AND DISCUSSION

For OSTE-COC device it was observed that by increasing channel AR it is possible to increase MP capture rate, which could be attributed to increase of surface volume and decrease of local flow rate (Fig. 2A.) Further described results were measured using COC-OSTE-Glass device as its fabrication yield was 97.5%. By testing different magnet setups, it was observed that a single magnet under the channel captured less than 50% MP at 200 µl/min. Alternately N52 magnets were placed on top and bottom of the channel but a significant difference was not observed (Fig. 2B). While using multiple small magnets under channels in a N/S configuration (magnets stacked laterally with opposite polarities) or in Halbach array showed improved performance exceeding 95% MP capture rate even in smallest AR channel. (see Fig. 2B).

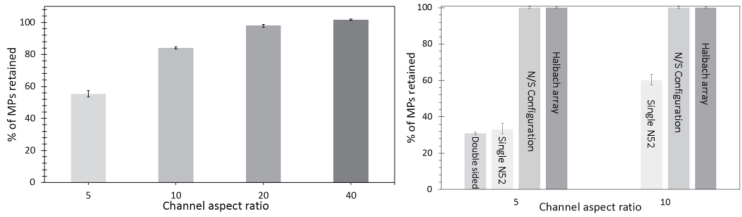

Figure 2: OSTE-COC device, magnetic particle capture efficiency at 100 µl/min and different channel AR (A), COC-OSTE-Glass device MP capture efficiency based on magnet configuration at 200 µl/min (B).

qPCR results revealed that by storing EVs at 7±1 C with a 10 RPM continuous rotation for 5h miR-375 levels decreased by 20% suggesting slight decrease in MP-bound intact EVs either due to loss of membrane integrity or dissociation (see Fig. 3A). Due to this decrease, linear approximation was introduced to mathematically normalize initial EV count over the experiment time, which was 5h. In EV evaluation experiments, all flow rates and both channel designs indicated between 67 – 100 % intact EV recovery in post-capture samples. (see Fig. 3B).

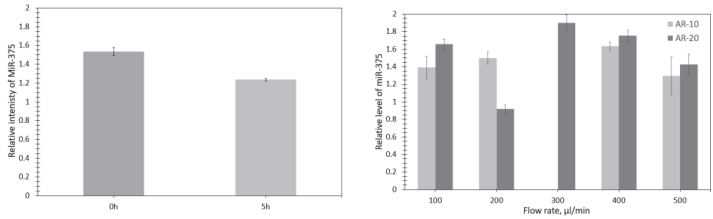

Figure 3: Relative levels of MP-bound EV miR-375 content at the start of experiment and at the end (A), and miR-375 levels after subjecting the same sample to magnetic capture at various flow rates. Light bars (AR – 10) and dark (AR - 20) (B).

CONCLUSION

By using herein-described design it was possible to achieve higher fabrication yields than via simple OSTE casting. These devices showed 95% MP capture rate when used in N/S magnetic or Halbach array setup. Based on intact EV recovery, no significant loss of EV intrinsic content was observed over the range of flow rates tested.

ACKNOWLEDGEMENTS

Project was funded by European Regional Development Fund (ERDF), Measure 1.1.1.1 “Support for applied research” No 1.1.1.1/20/A/045, “Development of a novel microfluidic device for label-free quantification of prostate cancer-derived extracellular vesicles and analysis of their RNA content (PROCEX)”

REFERENCES

[1] Vaidyanathan, R et al., *Lab Chip* 2018, *19* (1), 11–34.
[2] Nawaz, M. et al., *Nat. Rev. Urol. 2014 1112* 2014, *11* (12) 688-701
[3] van Meer, B. J. et. al., *Biochem. Biophys. Res. Commun.* 2017, *482* (2), 323–328
[4] R.Rimsa, et. al., *Micromachines* **2021**, *12*(5), 546;

CONTACT

* Janis Cipa; janis.cipa@cellboxlabs.com

polymers

MDPI

Article

Elucidating Extracellular Vesicle Isolation Kinetics via an Integrated Off-Stoichiometry Thiol-Ene and Cyclic Olefin Copolymer Microfluidic Device

Janis Cipa [1,2], Edgars Endzelins [3], Arturs Abols [2,3], Nadezda Romanchikova [3], Aija Line [3], Guido W. Jenster [4], Gatis Mozolevskis [1,2] and Roberts Rimsa [1,2,*]

[1] Institute of Solid State Physics, University of Latvia, 8 Kengaraga Str., LV-1063 Riga, Latvia; janis.cipa@cfi.lu.lv (J.C.); gatis.mozolevskis@cfi.lu.lv (G.M.)
[2] Cellbox Labs LLC, 8 Kengaraga Str., LV-1063 Riga, Latvia; arturs.abols@biomed.lu.lv
[3] Latvian Biomedical Research and Study Centre, Ratsupites Str. 1, LV-1067 Riga, Latvia; edgars.endzelins@biomed.lu.lv (E.E.); nadezda.romanchikova@biomed.lu.lv (N.R.); aija@biomed.lu.lv (A.L.)
[4] Department of Urology, University Medical Center Rotterdam, Dr. Molewaterplein 40, 3015 GD Rotterdam, The Netherlands; g.jenster@erasmusmc.nl
* Correspondence: roberts.rimsa@cfi.lu.lv

Abstract: Extracellular vesicles (EVs) are promising biomarkers for diagnosing complex diseases such as cancer and neurodegenerative disorders. Yet, their clinical application is hindered by challenges in isolating cancer-derived EVs efficiently due to their broad size distribution in biological samples. This study introduces a microfluidic device fabricated using off-stoichiometry thiol-ene and cyclic olefin copolymer, addressing the absorption limitations of polydimethylsiloxane (PDMS). The device streamlines a standard laboratory assay into a semi-automated microfluidic chip, integrating sample mixing and magnetic particle separation. Using the microfluidic device, the binding kinetics between EVs and anti-CD9 nanobodies were measured for the first time. Based on the binding kinetics, already after 10 min the EV capture was saturated and comparable to standard laboratory assays, offering a faster alternative to antibody-based immunomagnetic protocols. Furthermore, this study reveals the binding kinetics of EVs to anti-CD9 nanobodies for the first time. Our findings demonstrate the potential of the microfluidic device to enhance clinical diagnostics by offering speed and reducing manual labor without compromising accuracy.

Keywords: PDMS-free; microfluidics; extracellular vesicles; binding kinetics; immunomagnetic separation

Citation: Cipa, J.; Endzelins, E.; Abols, A.; Romanchikova, N.; Line, A.; Jenster, G.W.; Mozolevskis, G.; Rimsa, R. Elucidating Extracellular Vesicle Isolation Kinetics via an Integrated Off-Stoichiometry Thiol-Ene and Cyclic Olefin Copolymer Microfluidic Device. *Polymers* **2024**, *16*, 3579. https://doi.org/10.3390/polym16243579

Academic Editors: Yen-Wen Lu, Li-Hsien Yeh, Yi-Je Juang and Yan-Cheng Lin

Received: 29 November 2024
Revised: 15 December 2024
Accepted: 19 December 2024
Published: 21 December 2024

1. Introduction

Over the past decade, extracellular vesicles (EVs) have been of key interest as a biomarker for the detection of complex diseases such as cancer and neurodegenerative and cardiovascular diseases [1]. EVs are heterogeneous, plasma membrane-bound vesicles secreted by virtually all cell types that contain various cargo messenger molecules and can trigger a variety of cellular responses. Their diagnostic potential, particularly in liquid biopsy applications, has garnered increasing attention for clinical application [2,3]. EV-based analysis offers the potential for rapid disease detection, the monitoring of disease progression, and assessing drug effectiveness, ultimately improving patient care [4–6]. However, the implementation of EV-based diagnostics in clinical settings has been considerably impeded, primarily attributed to the lack of robust, efficient, and reproducible methodologies for the isolation of specific EV subpopulations. This issue is further amplified by their broad size distribution, spanning from 30 nm to 2000 nm, which poses substantial challenges for their analysis using standard laboratory assays [1].

Various methods exist for separating and analyzing EVs, such as ultracentrifugation [7], size exclusion chromatography [8], precipitation [9], and others [10]. However, the ongoing

challenge lies in obtaining specific EV subpopulations that are separated from cell debris and nonspecific EVs, and are enriched to perform quantitative downstream analysis. As such, immunomagnetic isolation represents the gold standard method due to efficient, fast, scalable, and specific extractions of EVs [11–17]. Furthermore, immunomagnetic isolation has been used for different purposes such as bacteria capture and DNA extraction [18], metabolite capture [19], EV separation [7], and others [20].

Building on existing methods, microfluidic devices represent a notable advancement in EV separation as they have shown promise with better enrichment compared to traditional methods like ultracentrifugation [7], along with higher throughput [21], reduced sample volume [22], and reduced labor intensity. Notably, Wang et al. demonstrated a microfluidic device's efficiency in single-chip analysis using magnetic particles and Raman spectroscopy, distinguishing between cancer patients and healthy individuals within an hour, where the EV capture efficiency was 72.5% [23]. A potential limitation of the current presented EV separation devices is the slow flow rate of 0.3 µL/min, which for a typical clinical sample size of at least 100 µL and a gold standard limit of detection of 12–15 IU/mL would take 5.5 h [24].

Given the prevalent surface markers on the surface of EVs, antibody capture mechanisms have been heavily utilized in the presented microfluidic and macroscale systems [25]. Recently, however, single-domain antibodies, typically derived from animals, have surged as an alternative to existing antibody-based capture [26]. Ref. [27] Nanobodies offer increased stability and better permeability due to smaller sizes retaining the same capture mechanisms as the antibodies; thus, nanobodies have emerged as a potential alternative in the diagnostics sector [27].

Despite several promising advantages of microfluidic devices, the applicability of microfluidics in EV diagnostics has been severely hindered due to materials typically used in device fabrication. Microfluidic devices typically use polydimethylsiloxane (PDMS) as their primary material; while PDMS is excellent for prototyping, it presents limitations for widespread adoption in EV analysis due to challenges in scaling for mass production and its tendency to absorb lipophilic molecules [28,29]. Moreover, in applications involving biological samples, the imperative for sterility necessitates the use of single-use devices, rendering PDMS economically impractical due to high costs.

In response to these constraints, alternative materials are being actively explored, with a focus on thermoplastics and other moldable substrates. Among the promising candidates are cyclic olefin copolymer (COC) and off-stoichiometry thiol-ene polymer (OSTE), where both materials show promise in reducing hydrophobic molecule absorption and offering structural versatility [29–32]. COC has been widely used as a biocompatible and transparent thermoplastic in different microfluidics applications [33], whereas OSTE materials have been incorporated or used separately for applications such as synthetic paper for enrofloxacin detection [34], spider silk fabrication [35], and as a channel for photonic biosensors [36], among others. Yet, to the best of our knowledge, OSTE-COC devices have only been fabricated for organs on chips [37] and EV separation based on flow field–flow fractionation [38] rather than a microfluidic EV sample preparation tool.

To advance EV extraction techniques and further integrate microfluidic biosensing applications, this study encompasses a comprehensive approach, covering the entire workflow from device fabrication to biological application. By introducing a proof-of-principle EV extraction device that integrates mixing and magnetic particle separation functions on a PDMS-free chip, we demonstrate advancements in assay turnaround time and process readiness for the fabrication of derivative designs. This novel approach not only improves the scalability of EV extraction but also offers a practical and versatile platform for testing with liquid biopsy samples containing EVs, paving the way for potential clinical applications.

2. Materials and Methods

2.1. Device Fabrication

OSTE-COC microfluidic device computer-aided design models were created for the photomask and 3D-printed mold in SolidWorks. The photomask was fabricated using standard lithography with positive AZ1518 resist (MicroChemicals, Ulm, Germany), and a direct laser writer (375 nm, Heidelberg μPG, Mittelgewannweg, Germany) was used for a 25 × 76 × 1 mm^3 patterned glass slide. After development, a 50 nm Al_2O_3 layer was deposited via atomic layer deposition (ALD Savannah) to protect the mask and ensure the repeatability of the mask.

A double-negative mold was 3D-printed (Zortrax, Olsztyn, Poland, basic white/ivory) using a resin 3D printer (Zortrax inkspire), where the layer thickness was 50 μm and pixel size was 50 × 50 μm^2. A post-printing mold was exposed with UV light for 810 s (12 J/cm^2) and cured for at least 48 h at 60 °C. A post-curing negative mold was made from soft, 2-component silicone, Qsill 216 (CHT smart chemistry, Tübingen, Germany).

The device substrate (140 μm, TOPAS, microfluidic chip shop) was O_2 plasma-treated (O_2 700 sccm, 700 W, 5 min, 2.45 GHz, PVA TePla gigabatch 360M, Wettenberg, Germany) with a COC sheet used to cap the Qsill mold. Microfluidic devices were fabricated using reaction injection molding of OSTE 220 (Mercene Labs, Ostemer, Stockholm, Sweden) using Al jig. Post-compression OSTE 220 was injected into the Qsill mold cavity at 800 mBar (Elveflow OB1 flow controller, Paris, France). After OSTE 200 injection, the device was exposed using ND33 and I-line filter (Mask aligner Suss MA6, Garching, Germany) to decrease exposure intensity to 6 mJ/(cm^2s), with a final dose of 108 mJ/cm^2.

After exposure, the device was developed in acetone in an ultrasonic bath (80 kHz, 50%, Elmasonic P, Singen, Germany) for 75 s, where the reaction was subsequently stopped by isopropanol and N_2 blow-dried. A post-development bake was performed at 60 °C for 3 min to reduce mechanical stress and allow for better layer bonding. Before bonding the top part of the device, the COC slide was treated with O_2 plasma (700 sccm O_2, 700 W, 3 min).

Finally, both layers were aligned, pressed together, and exposed to a 4000 mJ/cm^2 dose. Subsequently, the device was cooled down for a few minutes, resulting in a hermetically sealed device, with a burst point exceeding 400 μL/min.

2.2. Flow Controls

Microfluidic flow was controlled using 5 mL syringes and syringe pump (ISPLab02 DKinfusetek, Hvidovre, Denmark). The connection between different device modules was ensured using 800 μm diameter polytetrafluoroethylene (PTFE) tubing, 800 μm diameter Masterflex C-Flex tubing (Darwin microfluidics, Paris, France), and polypropylene Luer ports (ChipShop, Jena, Germany).

2.3. Hollow-Fiber Bioreactor Culture of LNCaP Cells

A C2011 high-flux PS hollow-fiber cartridge (Fibercell, New Market, MD, USA) was pre-coated with 0.5 mg human fibronectin and inoculated with 2.76 × 10^8 LNCaP cells. During the colonization phase, 125 mL LNCaP flask culture medium (RPMI + 2 mM sodium pyruvate + 2 mM L-glutamine + 10% FBS), supplemented with additional glucose up to 4 g/L, was recirculated through the cartridge. Circulating media was exchanged based on daily glucose consumption readings, the volume was gradually increased, and the composition gradually switched to DMEM/F12 with the same supplements. Once reaching 1000 mg daily glucose consumption, FBS was substituted by 10% CDM-HD serum replacement (Fibercell) and daily conditioned media harvesting from the extracapillary space (ECS) was commenced. The conditioned media was pre-processed by sequential centrifugation (5 min at 300× *g*, 30 min at 3000× *g*) and stored at +4 °C until isolation of EVs.

2.4. Isolation of EVs

EVs were isolated from the conditioned cell culture media by size exclusion chromatography (SEC) using qEV10 35 nm SEC columns (Izon, Bellarie, TX, USA) according to the manufacturer's guidelines. Prior to loading onto columns, the pre-processed media samples from up to 4 sequential day harvests were pooled together, filtered through 0.2 μm syringe filters, and concentrated down to 10 mL using Amicon-15 100 kDa ultrafiltration tubes (Merck KGaA, Darmstadt, Germany). The particles in each 5 mL SEC fraction were analyzed with Zetasizer Nano (Malvern), and the EV-containing ones (usually 4 fractions) were pooled together and concentrated using Amicon 3 kDa ultrafiltration tubes (Merck KGaA, Darmstadt, Germany). EV preparations were aliquoted and stored at –80 °C.

2.5. EV Concentration Measurements

The size distribution and concentration of EVs were assessed using nanoparticle tracking analysis (NTA) with the NanoSight NS300 instrument (Malvern, Malvern, UK). Briefly, EV samples were diluted 500–2000-fold in PBS to achieve a concentration range of 1×10^8 to 1×10^9 particles/mL and introduced into the flow cell using a 1 mL syringe. Five 60 s videos were recorded at camera level 14, with the sample manually advanced between recordings. Particle tracking was conducted at a detection threshold of 4–5. Protein concentration was determined by Pierce BCA protein assay (Thermo Fisher, Waltham, MA, USA).

2.6. Transmission Electron Microscopy

First, 10 μL of EV suspension was applied onto a 300-mesh carbon-coated copper EM grid and incubated for 5 min. The grid was negatively stained with 1% uranyl formate solution for 60 s. After air-drying, examination was carried out using a JEM-1230 microscope (JEOL, Peabody, MA, USA).

2.7. Anti-CD9 Nanobody Production

DNA sequence encoding nanobody recognizing CD9 was generously provided by Prof. Guido Jenster. The sequence was further engineered to contain C-terminal His_6 and HA affinity tags, and adapted for cloning into pET-26b(+) periplasmic expression plasmid. The gene synthesis and cloning into the plasmid were outsourced to BioCat GmbH, Heidelberg, Germany.

BL21 (DE3) *E. coli* cells were subjected to transformation with the Nb-encoding plasmid. After confirming the periplasmic presence in WB with an antibody against His_6 tag (MA1-21315, Thermo Fisher; in 1:3000 dilution), anti-CD9 Nb was purified from 540 mL of transformed culture. In brief, induced cells were pelleted at 6500× *g* for 15 min, +4 °C. The pellet was resuspended into 240 mL 30 mM Tris-HCl pH 8.0 + 20% sucrose and brought to 1 mM EDTA, then slowly stirred for 10 min at RT. The cells were pelleted again by centrifugation at 6500× *g*, 15 min, +4 °C, resuspended into 240 mL ice-cold 5 mM $MgSO_4$, and slowly stirred for 10 min while maintaining +4 °C. Next, the shocked cells were pelleted at 6500× *g*, 15 min, +4 °C, and the supernatant was collected. The supernatant (periplasmic lysate) was brought to 150 mM NaCl, 2 mM $MgCl_2$, 20 mM imidazole, pH 7.5 and filtered through 0.2 μm before loading onto 5 mL HisTrap™ Fast Flow columns (GE17-5255-01, GE Healthcare, Chicago, IL, USA) for purification using ÄKTAprime plus (Cytiva) chromatography system. In short, each column was equilibrated with 5–10 volumes of 1× Binding Buffer (150 mM NaCl, 2 mM $MgCl_2$, 20 mM imidazole, pH 7.5), followed by application of the sample. The column was washed first with 1× high-salt buffer (20 mM HEPES, pH 7.5; 500 mM NaCl; 20 mM imidazole), and then with 1× NH7.5 buffer (2 mM HEPES, pH 7.5; 100 mM NaCl) + 20 mM imidazole until the absorbance reached the baseline. The purified Nb was eluted in 1× NH7.5 buffer (2 mM HEPES, pH 7.5; 100 mM NaCl) + 400 mM imidazole. Approximately 7 mL of the elute was collected and subjected to buffer replacement and concentration on Amicon-15 3 kDa spin columns (5000× *g*, +4 °C). Nanobody samples were aliquoted for storage at −20 °C into protein

low-bind tubes (Eppendorf). Nb concentration was determined by Pierce BCA protein assay (Thermo Fisher).

2.8. EV Capture ELISA

Anti-CD9 nanobody affinity towards native CD9 on EV samples from multiple cell lines was assessed in exosome ELISA using PS Capture™ Exosome ELISA Kit (297-79201, FUJIFILM Wako, Tokyo, Japan) according to the manufacturer's protocol. All EVs were used in amounts of 2×10^8 pts per ELISA well. The nanobody was tested in increasing concentrations from 2 to 20 μg/mL and secondary anti-His6-HRP (MA1-21315-HRP, ThermoFisher) was used at a 2 μg/mL concentration.

2.9. Anti-CD9 Magnetic Particles

Anti-CD9 magnetic particles (MPs) were prepared by loading each 1 mg of Pierce anti-HA magnetic beads (Thermo Fisher) with 20 μg anti-CD9 nanobody featuring a C-terminal HA affinity tag. The loading was performed for 30 min at room temperature on a tube rotary mixer (15 RPM), and afterwards any excess nanobody was removed from the reaction by washing 4× with PBS + 0.1% BSA + 0.05% Tween-20.

2.10. EV Capture to Anti-CD9 Magnetic Particles

Anti-CD9 bead performance was initially characterized by setting up test tube EV capture reactions between 0.6 mg magnetic particles and 6×10^9 LNCaP EV pts in 0.6 mL PBS + 0.1% BSA, which were rotated (10 RPM) either for 1 h at room temperature or for 3 h at +4 °C. Afterwards, any unbound EVs were removed by washing the MPs 3× with 1 mL PBS + 0.1% BSA + 0.05% Tween-20 and once with 1 mL PBS. Afterwards, all the supernatant was removed and the MPs were heated for 5 min at 95 °C in 20 μL of non-reducing Laemmli buffer. The supernatant containing lysated EVs was then collected and directly analyzed by Western blot (10 μL per each lane) with HRP-conjugated antibody against CD63 (Novus Biologicals, Centennial, CO, USA, NBP2-34779H, 1:2000 dilution) and the novel nanobody against CD9 in conjunction with secondary anti-His_6—HRP (Thermo Fisher, MA1-21315-HRP, 1:1000 dilution).

2.11. Sample Flow Control and Washing

EV sample and surface-modified magnetic particles were loaded in separate syringes or tubing, where a 25 μL air gap was used to separate samples from the wash buffer, which was sequentially used after sample inflow. ON-Chip washing was conducted by flushing the device with 3 mL of PBS + 0.1% BSA + 0.05% Tween-20 solution. In case cycling was used, the withdrawal flow rate was reduced to 100 μL/min to prevent air creep in the system. To extract the sample, the magnet array was removed and the MPs containing bound EVs were eluted. For comparison, a standard benchtop EV capture protocol was performed by reacting the same samples in a 2 mL test tube on a rotary mixer (15 RPM) for 50 min, and washing 4× with 1 mL of PBS + 0.1% BSA + 0.05% Tween-20.

2.12. Western Blot

For Western blot (WB) analysis, 10 μL of lysate in either reducing or non-reducing (for anti-tetraspanin antibodies) Laemmli was loaded per each lane of a 10% SDS-PAGE gel. Following the separation at 150 V, the proteins were transferred onto 0.45 μm nitrocellulose membranes, which were subsequently blocked using 10% (w/v) fat-free milk for 1 h at room temperature. The membranes were then incubated with primary antibody (Table S1) overnight at +4 °C and 60 RPM, and washed 4 times with TBS + Tween-20 (0.05%, 0.1%, 0.1%, 0.05%). The incubation with secondary antibody (Table S1) was conducted for 1 h at room temperature 60 RPM, followed by washing as previously described. Detection of immunoreactive bands was carried out using the Amersham™ ECL Select™ Western Blotting Detection Reagent kit (GE HealthCare) and pictures were taken using a Nikon d610 dSLR body (Nikon, Tokyo, Japan) with Sigma 35 mm f/1.4 DG HSM Art lens (Sigma,

Kawasaki, Japan). To acquire numerical band integrated density values, ImageJ software (version 1.54g) was used. To account for differences in compared WB membranes, total EV quantity was used to normalize the signal intensity and is indicated on the graphs as total EV quantity or ctrl. +. When necessary, the membrane was stripped in a buffer containing 1.5% glycine, 0.1% SDS, 1% Tween-20, pH 2.2, blocked again, and re-probed with a different set of antibodies as previously described.

3. Results and Discussion

3.1. Microfluidic Device

To facilitate the mass production of a sterile device, a passive zigzag mixing design was chosen [39]. Its modularity allows for adjustable length based on mixing needs, while its 2D structure supports efficient manufacturing via injection molding further in the project, but also CNC milling, and laser ablation that allows for rapid design prototyping. Additionally, the lack of active components simplifies assembly, thus enhancing scalability and cost-effectiveness. Device geometry (Figure S1) was optimized based on our results of mixing index testing, following methodology described by Hashmi [40] (Table S2), where flow rate was tested from 50 µL to 200 µL and points to a strong correlation between increasing flow rate and increases in mixing ($p = 2.57 \times 10^{8}$). Secondly, decreasing channel size from 300 µm to 200 µm showed a statistically significant increase in relative mixing index ($p = 9 \times 10^{-5}$). Thirdly, no significant effect of varied bend angle in the range of 75 to 81 degrees ($p = 0.278$) can be seen, with analysis performed at the 95% confidence interval, where similar results were reported by Cosentino et al. for multiple bends in a passive micromixer [41]. As such, a device with 200 × 200 µm channels and 764 mm length was fabricated using OSTE 220 material (Figure 1). The resolution of the smallest corner radius was 20 µm, and a burst point exceeded 400 µL/min as tested by operating devices using DI water. Furthermore, the finished device consisted of an OSTE layer compressed between two COC layers; thus, the device had excellent optical properties due to COC visible light transparency [42]. A similar device fabrication process has been previously reported by Sandström N. [43], but in our case, a COC sheet and COC slide with luer connections were used, which allows for simple connections and the potential for design scalability. Furthermore, the fabrication protocol builds on our previous work [31] by decreasing the feature size down to 20 µm and improving the fabrication speed, as this fabrication method allows us to remove thermal treatment; thus, the ready device can be made in under 1 h.

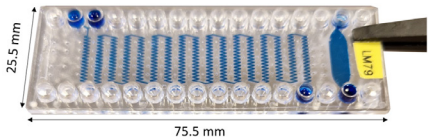

Figure 1. Fabricated OSTE-COC device, macro-image.

To test magnetic particle and EV interactions in fabricated microfluidic devices, an experimental setup was created using a fused deposition modeling (FDM) 3D printer, as seen in Figure 2. This setup includes two identical OSTE-COC microfluidic devices with a volume of 27 µL and 510 bends (see Figure 2c for mixing and magnetic separation chamber), with surface area of 55 mm^2, as shown in Figure 2d. MP separation was conducted based on our previous publication using a 4 mm wide magnetic separation chamber (Figure S2) [44]. Four magnetic configurations were tested: a single N52 magnet under the channel Figure S3a; two N52 magnets, both under and above the channel Figure S3b; 18 ($8 \times 5 \times 5$ mm^3) N45 magnets stacked in alternating polarity (Figure S3c and in Halbach array Figure S3d). The optimal configuration was determined to be alternating polarity, as it was a stable configuration with a retention of over 95% of the magnetic particles at a 200 µL/min flow rate [44]. The magnet array was placed in a 3D-printed jig to fix the device and decrease the air gap between the device and magnet array (Figure 2d).

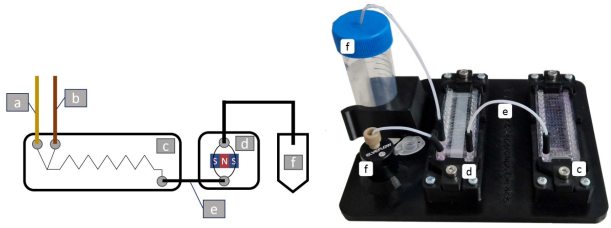

Figure 2. Schematic of the microfluidic device incorporating MP injection tubing (a), sample injection tubing (b), mixing device (c), MP separation module (d), tubing for cycling or shorter tubing for connection to a sample collection container (e), sample collection container (f) on the left and macro-image on the right.

3.2. *Hollow-Fiber Bioreactor Production of Extracellular Vesicle Standards*

For testing EV capture in the microfluidic device, a sufficient amount of standardized EV preparation was necessary. For this purpose, a C2011 high-flux PS hollow-fiber cartridge (Fibercell) with 2.76 × 10^8 LNCaP cells was inoculated and harvested daily from the extra-capillary space (ECS) as soon as optimal colonization was achieved. EVs from combined 3- or 4-day harvests were purified by size-exclusion chromatography (SEC) and measured by nanoparticle tracking analysis (NTA) (Figure 3b) and the BCA protein assay. In summary, this bioreactor culture yielded 3.92 × 10^{12} EV particles (6.9 mg EV proteins) during a 71 day timeframe (Figure 3a). Select EV batches were also characterized by transmission electron microscopy (TEM), which indicated a polydisperse mixture of predominantly sub-100 nm particles (Figure 3c). Western blot (WB) analysis on select EV batches, compared to cell lysates obtained from the same bioreactor culture, and ECS-secreted proteins, were consistent with highly pure EV preparations, revealing enrichment in EV-characteristic markers (ALIX, CD63, and TSG101), and no presence of endoplasmic reticulum marker Calnexin, which was used as a negative control (Figure 3d).

a

EV batch #	EV proteins, µg (BCA)	EV pts, x 10^9 (NTA)
1	1479.5	338.3
2	729	171
3	261	328.5
4	147.5	130
5	250	320
6	190	85.6
7	304	426.1
8	362.3	219.2
9	557.5	232.5
10	346.5	475.8
11	264	129.8
12	155	60.3
13	298	208
14	181.5	52.7
15	333	190.8
16	22.5	13.5
17	203.5	50.3
18	170	158.5
19	211.3	129.4
20	196	118
21	197.5	81

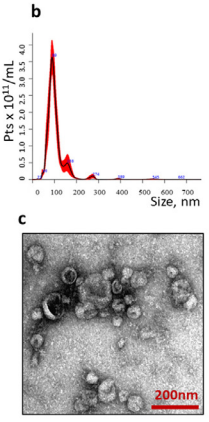

Figure 3. Extracellular vesicle (EV) production from LNCaP hollow-fiber bioreactor culture. EV protein amounts and particle counts in all batches purified during 71-day timeframe (**a**). Representative EV particle size distribution by nanoparticle tracking analysis (**b**). Representative transmission electron microscopy image (**c**). Characterization of EV markers by Western blot (**d**).

3.3. Magnetic EV Capture Particles Featuring Novel Anti-CD9 Nanobody

The DNA sequence for the nanobody (Nb) recognizing CD9, and abundant EV surface markers, were kindly provided by Prof. Guido Jenster. Here, we further modified the sequence to encode C-terminal His_6 and HA affinity tags to facilitate downstream purification, detection, and surface immobilization workflows, expressed it in BL21 (DE3) *E. coli* strain, and purified it from its periplasmic lysate by IMAC chromatography. Ultimately, 540 mL of induced BL21 (DE3) culture (OD_{540} = 6.8) yielded 18.1 mg of purified product (BCA protein assay). The product was then confirmed in WB with anti-His_6 antibody (Ab) to be consistent with the expected 16 kDa molecular weight of the anti-CD9 Nb (Figure 4a) and further assayed for purity by Coomassie staining, which indicated no other molecular weights present (Figure 4b). PS Capture™ Exosome ELISA indicated a strong affinity towards EVs obtained from multiple cell lines (LNCaP, PC3, and SW620) starting from 2 µg/mL anti-CD9 Nb concentration. The signal intensity was comparable to the control antibody (against CD63) of the ELISA kit at the Nb concentration of 20 µg/mL when tested against EVs from CD9-positive lines (LNCaP and SW620) and, as expected, there was a decreased reactivity against EVs obtained from the CD9-low PC3 line (Figure 4c). Finally, we loaded Pierce anti-HA magnetic particles (Dynabeads™) with 20 µg of anti-CD9 Nb per each 1 mg of MPs and tested their ability to capture LNCaP EVs at 1 mg/mL bead concentration under different reaction conditions. WB analysis against CD63 and CD9 EV markers in the lysates from the capture MPs after the reaction, both when reacted for 1 h at room temperature and for 3 h at +4 °C indicated nearly complete EV capture compared to the same amount of EVs in the positive control (Figure 4d). Additionally, no captured EVs were detected if the capture MPs were prepared without Nb, indicating high capture specificity (Figure 4d).

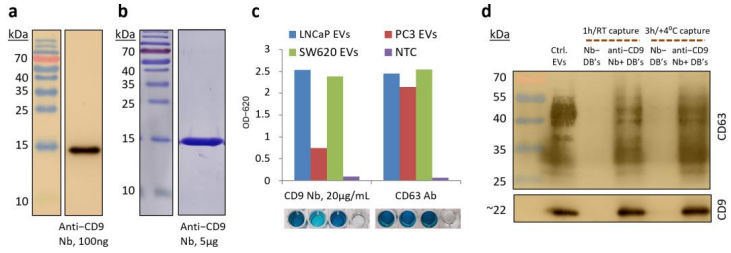

Figure 4. Anti-CD9 nanobody (Nb) quality control and performance assessment. Western blot detection of His_6-tagged anti-CD9 Nb in purified Nb preparation (**a**). Coomassie staining of total proteins in purified Nb preparation (**b**). PS Capture™ Exosome ELISA analysis indicating an exceptional extracellular vesicle (EV) capture by anti-CD9 Nb at 20 µg/mL as compared to the anti-CD63 control (**c**). WB demonstrating LNCaP EV capture performance of anti-CD9 nanobody-coated Dynabeads™ under various capture conditions (**d**).

3.4. Flow Rate Sweep for Anti-CD9 Magnetic Particles

To evaluate the efficiency of the MP separation in the microfluidic device compared to traditional lab assays, a flow rate sweep was conducted under conditions relevant to sample viscosity. LNCaP EVs were utilized in the microfluidic device, employing 1 µm diameter magnetite core MPs conjugated with anti-CD9 nanobody for EV capture. Following EV capture by MPs, EV-containing MPs were separated from the sample, either ON-Chip or in a tube, with subsequent washing performed either ON-Chip or OFF-Chip (in tube). For ON-Chip separation, MPs were washed with PBS buffer solution (PBS + 0.1% BSA + 0.05% Tween-20) at 200 µL/min and then collected in a new container. OFF-Chip separation followed a standard procedure where EV-containing MPs were retained using a benchtop magnet, followed by triple washing on the magnet. EV-containing MPs were heated in 1× Laemmli sample buffer for 5 min at 95 °C, followed by MP removal with a benchtop

magnet, and loading the supernatant on SDS-PAGE gel for Western blot analysis. Figure 5 illustrates the relative intensity of the CD63 bands, reflecting the EV capture efficiency across both ON-Chip and OFF-Chip workflows.

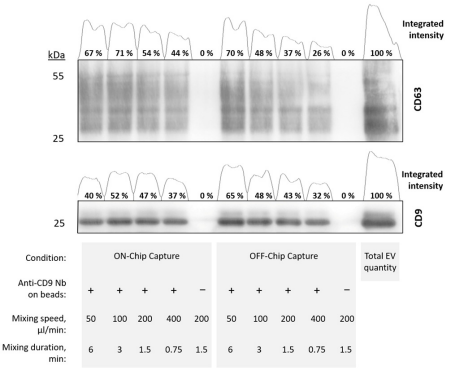

Figure 5. EV and anti-CD9 nanobody-conjugated MP mixing in OSTE-COC device. MP retention was conducted either ON-Chip or OFF-Chip at different flow rates. Numerical values are normalized relative to the total initial quantity of extracellular vesicles used in each capture reaction (as indicated in the last Western blot column). Anti-CD9 specificity of MPs was tested by including MPs not containing nanobody (denoted by −) in reaction with EVs.

The Western blot results from Figure 5 reveal that at 50 µL/min using OFF-Chip MP retention, the intensity accounts for 70% and 65% of the total EV count, which surpasses that of the ON-Chip MP retention at 67% and 40% for CD63 and CD9, respectively. This discrepancy could be attributed to differences in setup configurations. In the ON-Chip setup, MP retention occurs on the chip, ensuring that all non-captured EVs pass through magnetically bound MPs and are subsequently discarded. In contrast, OFF-Chip retention allows for post-mixing interactions within the container, potentially extending incubation time and subsequently enhancing signal intensity. This implies that although the ON-Chip setup provides a more accurate representation of the actual interaction time, it yields a diminished signal due to effectively reduced incubation time.

Moreover, linear regression analysis indicates that the decrease in CD63 intensity is marginally significant for both systems ($p = 0.058$ for ON-Chip and $p = 0.10$ for OFF-Chip). For ON-Chip CD9 retention, a flow-independent result is observed ($p = 0.49$), while for OFF-Chip, a marginally significant intensity decrease is noted ($p = 0.091$). This suggests that ON-Chip capture produces more consistent results than OFF-Chip capture (Figure S4). To enhance binding efficiency and elucidate the binding process, multiple cycles through the mixer were introduced, thereby increasing interaction within the mixing module.

3.5. Proof-of-Principle EV Sample Preparation Unit

To assess binding kinetics and demonstrate the performance of a proof-of-principle sample preparation unit, a complete system comprising an integrated mixing module and magnetic separation module was tested and compared to a standard lab assay in a semi-automatic operation setting.

Analysis of EV binding kinetics was conducted using LNCaP EVs mixed with 1 µm MPs conjugated with anti-CD9 nanobodies, with a total sample volume of 300 µL and a flow rate of 150 µL/min. The EV sample and MPs were cycled 1 to 10 times to enhance EV binding. Moreover, the process was semi-automated by preloading the sample and buffer solution for post MP retention washing in the syringe pumps. Following the mixing of LNCaP EVs with anti-CD9 MPs in a microfluidic device, magnetic separation was used

to separate post-EV capture MPs from reaction mix. ON-Chip washing was performed subsequently using a flow rate of 150 µL/min. Post-washing, the MP captured EVs were subjected to heat treatment in 1× Laemmli sample buffer for EV lysis and the supernatant was loaded directly onto SDS-PAGE gel for subsequent Western blot analysis. Simultaneously, a standard benchtop EV capture reaction with the same MPs were performed for comparative purposes (Figure 6).

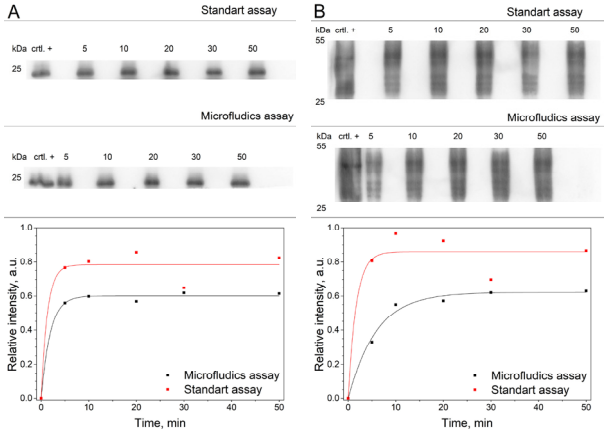

Figure 6. Western blot analysis showing the efficiency of EV capture. Anti-CD9 EV capture and CD9 detection (**A**) and WB results for anti-CD9 EV capture and CD63 detection (**B**) where the top figure is WB image, and each data point is an integrated value relative to EV marker signal intensity.

Western blot signal indicates that the maximum relative binding efficiency of EVs to the MPs was f_∞ = 0.60 ± 0.01 and is comparable to the standard laboratory assay f_∞ = 0.78 ± 0.04 as seen in Figure 6A. The CD63 analysis, performed using an antibody against CD63 as shown in Figure 6B, confirmed the successful capture of extracellular vesicles (EVs) or double-positive membrane fragments, rather than free-floating CD9 protein. The comparable data from both markers confirms most of the signal comes from captured double positive vesicles with little, if any, influence from free floating CD9 protein

To further evaluate the data, an exponential growth model $f = f_\infty[1 - exp(-st)]$ was fitted for the background corrected integrated WB values using the least square method where a similar model was employed by Petkovica et al. [45]. Here the f_∞ is the asymptotic value of the binding efficiency and σ is the binding rate, with results summarized in Table 1.

Table 1. Asymptotic value of the binding efficiency and the binding rate of integrated WB signals.

	R^2	f_∞	σ
CD9 microfluidics	0.99	0.60	0.53
CD9 Standard assay	0.94	0.78	0.77
CD63 microfluidics	0.99	0.62	0.17
CD63 Standard assay	0.92	0.86	0.60

The data indicate that the majority of EV binding to MPs occur rapidly, within the first 10 min of the reaction. This represents a considerable improvement over to typical laboratory assays, where the binding time of MPs to analytes is expected to be in the range of 1 h to 24 h, as noted by multiple MP protocols [46,47]. Enhanced binding speed in an ON-Chip system compared to traditional antibodies, coupled with the potential for automation, is a key advantage. The entire process can be simplified by setting initial

parameters in the flow control system, loading the sample, and removing the magnet, eliminating the need for complex workflows that involve more than 10 manual steps in conventional lab settings. This approach also has the potential to be scaled for use in a simple laboratory instrument, improving efficiency and ease of use. To further improve the microfluidic assay, the overall lengths of the interconnections could be shortened, and the elution buffer could be stored ON-Chip, thereby reducing any elution losses related to passing small volumes of liquid through the tubing. This would improve the particular assay performance but would consequently limit the system flexibility to run other assays.

4. Conclusions

In conclusion, a novel microfluidic device, fabricated from cyclic olefin copolymer and off-stoichiometry thiol-ene, has been developed to effectively address common challenges, such as the absorption of lipophilic molecules found in polydimethylsiloxane-based systems. For the analysis of prostate cancer EVs, bioreactor-produced LNCaP-derived EVs were employed. The device enhanced immunomagnetic extracellular vesicle capture, leveraging anti-CD9 nanobodies.

Compared to standard assays, the microfluidic device showed increased EV capture efficiency at flow rates of 100–400 µL/min and incubation times from 1.5 to 3 min. Binding kinetics revealed that anti-CD9 nanobodies facilitate rapid EV capture, and binding saturation is reached in 10 min. The binding efficiency f_∞ = 0.6 and 0.62 for the microfluidic device is comparable to f_∞ = 0.78 and 0.86 for a lab assay, as indicated by CD9 and CD63 EV biomarker levels in post-capture MP sample. The anit-CD63 antibody analysis confirmed the successful capture of EVs or double-positive membrane fragments, rather than free-floating CD9 protein.

Comparable binding efficiency, paired with reduced manual labor and rapid processing capabilities, demonstrates the potential of the device as a useful tool in clinical diagnostics.

Supplementary Materials: The following supporting information can be downloaded at: https://www.mdpi.com/article/10.3390/polym16243579/s1, Table S1: Antibodies used in Western Blot. Table S2: Correlation matrix of relative mixing index for mixing devices, calculated using Pearson correlation coefficient. The top right cells represent the *p*-value of the correlation coefficient. Figure S1: OSTE-COC passive micromixer design utilized for mixing index testing. Figure S2: Magnetic separation module dimensions in mm. Figure S3: Experimentally tested magnetic configurations using magnetic particles (Dynabeads™). Tests were carried out and results were reported by Cipa et al. Figure S4: Liner regression analysis of integrated intensity for Figure 5, where doted lines represent OFF-Chip MP retention and solid line ON-Chip MP retention. Figure S5: Original uncropped western blot gel images for Figure 3d, Figure S6: Original uncropped western blot gel images for Figure 4a. Figure S7: Original uncropped western blot gel images for Figure 4b. Figure S8: Original uncropped western blot gel images for Figure 4d. Figure S9: Original uncropped western blot gel images for Figure 5. Using CD9 capture and CD63 detection nanobodies. Figure S10: Original uncropped western blot gel images for Figure 5. Using CD9 capture and CD9 detection nanobodies. Figure S11: Original uncropped western blot gel images for Figure 6B. Using CD9 capture and CD63 detection nanobodies. standard assay on the left and microfluidics assay on the right. Figure S12: Original uncropped western blot gel images for Figure 6A. Using CD9 capture and CD9 detection nanobodies. standard assay on the left and microfluidics assay on the right.

Author Contributions: J.C.: Investigation (equal); methodology (equal); writing—original draft (lead); writing—review and editing (equal); formal analysis (equal). E.E.: Investigation (equal); methodology (equal); writing—review and editing (equal); formal analysis (equal). A.A.: Supervision (supporting); writing—review and editing (equal). N.R.: Methodology (supporting); writing—review and editing (supporting). A.L.: Conceptualization (equal); project administration (lead), writing—review and editing (equal). G.W.J.: Methodology (supporting), conceptualization (equal); writing—review and editing (equal). G.M.: Conceptualization (equal); writing—review and editing (equal). R.R.: Conceptualization (equal); methodology (supporting); writing—original draft (supporting); writing—review and editing (equal). All authors have read and agreed to the published version of the manuscript.

Funding: Project was funded by European Regional Development Fund (ERDF), Measure 1.1.1.1 "Support for applied research" No 1.1.1.1/20/A/045, "Development of a novel microfluidic device for label-free quantification of prostate cancer-derived extracellular vesicles and analysis of their RNA content (PROCEX)". Institute of Solid-State Physics, University of Latvia as the Center of Excellence has received funding from the European Union's Horizon 2020 Framework Programme H2020-WIDESPREAD-01-2016-2017-TeamingPhase2 under grant agreement No. 739508, project CAMART2. RR acknowledges the support of Latvian Council of Science project VPP-EM-FOTONIKA-2022/1-0001 "Smart Materials, Photonics, Technologies, and Engineering Ecosystems".

Data Availability Statement: The raw data supporting the conclusions of this article will be made available by the authors on request.

Conflicts of Interest: Janis Cipa was employee of Cellbox Labs. Arturs Abols, Gatis Mozolevskis and Roberts Rimsa are founders and hold equity in Cellbox Labs. Guido Jenster is, as inventor, in the process of submitting a patent application on the sequence and uses of the anti-CD9 nanobody (H6). The remaining authors declare that the research was conducted in the absence of any commercial or financial relationships that could be construed as a potential conflict of interest.

References

1. Shao, H.; Im, H.; Castro, C.M.; Breakefield, X.; Weissleder, R.; Lee, H. New Technologies for Analysis of Extracellular Vesicles. *Chem. Rev.* **2018**, *118*, 1917–1950. [CrossRef] [PubMed]
2. Nawaz, M.; Camussi, G.; Valadi, H.; Nazarenko, I.; Ekström, K.; Wang, X.; Principe, S.; Shah, N.; Ashraf, N.M.; Fatima, F.; et al. The Emerging Role of Extracellular Vesicles as Biomarkers for Urogenital Cancers. *Nat. Rev. Urol.* **2014**, *11*, 688–701. [CrossRef]
3. Liu, C.; Zhao, J.; Tian, F.; Cai, L.; Zhang, W.; Feng, Q.; Chang, J.; Wan, F.; Yang, Y.; Dai, B.; et al. Low-Cost Thermophoretic Profiling of Extracellular-Vesicle Surface Proteins for the Early Detection and Classification of Cancers. *Nat. Biomed. Eng.* **2019**, *3*, 183–193. [CrossRef] [PubMed]
4. Pandey, C.M.; Augustine, S.; Kumar, S.; Kumar, S.; Nara, S.; Srivastava, S.; Malhotra, B.D. Microfluidics Based Point-of-Care Diagnostics. *Biotechnol. J.* **2018**, *13*, 1700047. [CrossRef] [PubMed]
5. Li, G.; Tang, W.; Yang, F. Cancer Liquid Biopsy Using Integrated Microfluidic Exosome Analysis Platforms. *Biotechnol. J.* **2020**, *15*, 1900225. [CrossRef]
6. Marrugo-Ramírez, J.; Mir, M.; Samitier, J. Blood-Based Cancer Biomarkers in Liquid Biopsy: A Promising Non-Invasive Alternative to Tissue Biopsy. *Int. J. Mol. Sci.* **2018**, *19*, 2877. [CrossRef] [PubMed]
7. Reátegui, E.; Van Der Vos, K.E.; Lai, C.P.; Zeinali, M.; Atai, N.A.; Aldikacti, B.; Floydjr, F.P.; Khankhel, A.H.; Thapar, V.; Hochberg, F.H.; et al. Engineered Nanointerfaces for Microfluidic Isolation and Molecular Profiling of Tumor-Specific Extracellular Vesicles. *Nat. Commun.* **2018**, *9*, 175. [CrossRef]
8. Grant, R.; Ansa-Addo, E.; Stratton, D.; Antwi-Baffour, S.; Jorfi, S.; Kholia, S.; Krige, L.; Lange, S.; Inal, J. A Filtration-Based Protocol to Isolate Human Plasma Membrane-Derived Vesicles and Exosomes from Blood Plasma. *J. Immunol. Methods* **2011**, *371*, 143–151. [CrossRef] [PubMed]
9. Ludwig, A.K.; De Miroschedji, K.; Doeppner, T.R.; Börger, V.; Ruesing, J.; Rebmann, V.; Durst, S.; Jansen, S.; Bremer, M.; Behrmann, E.; et al. Precipitation with Polyethylene Glycol Followed by Washing and Pelleting by Ultracentrifugation Enriches Extracellular Vesicles from Tissue Culture Supernatants in Small and Large Scales. *J. Extracell. Vesicles* **2018**, *7*, 1528109. [CrossRef] [PubMed]
10. Cheng, S.; Li, Y.; Yan, H.; Wen, Y.; Zhou, X.; Friedman, L.; Zeng, Y. Advances in Microfluidic Extracellular Vesicle Analysis for Cancer Diagnostics. *Lab Chip* **2021**, *21*, 3219–3243. [CrossRef]
11. Wan, Y.; Cheng, G.; Liu, X.; Hao, S.J.; Nisic, M.; Zhu, C.D.; Xia, Y.Q.; Li, W.Q.; Wang, Z.G.; Zhang, W.L.; et al. Rapid Magnetic Isolation of Extracellular Vesicles via Lipid-Based Nanoprobes. *Nat. Biomed. Eng.* **2017**, *1*, 0058. [CrossRef] [PubMed]
12. Chen, W.; Li, H.; Su, W.; Qin, J. Microfluidic Device for On-Chip Isolation and Detection of Circulating Exosomes in Blood of Breast Cancer Patients. *Biomicrofluidics* **2019**, *13*, 054113. [CrossRef]
13. Zhao, Z.; Yang, Y.; Zeng, Y.; He, M. A Microfluidic ExoSearch Chip for Multiplexed Exosome Detection towards Blood-Based Ovarian Cancer Diagnosis. *Lab Chip* **2016**, *16*, 489–496. [CrossRef] [PubMed]
14. Clayton, A.; Court, J.; Navabi, H.; Adams, M.; Mason, M.D.; Hobot, J.A.; Newman, G.R.; Jasani, B. Analysis of Antigen Presenting Cell Derived Exosomes, Based on Immuno-Magnetic Isolation and Flow Cytometry. *J. Immunol. Methods* **2001**, *247*, 163–174. [CrossRef] [PubMed]
15. Chen, J.; Xu, Y.; Lu, Y.; Xing, W. Isolation and Visible Detection of Tumor-Derived Exosomes from Plasma. *Anal. Chem.* **2018**, *90*, 14207–14215. [CrossRef]
16. Shao, H.; Chung, J.; Lee, K.; Balaj, L.; Min, C.; Carter, B.S.; Hochberg, F.H.; Breakefield, X.O.; Lee, H.; Weissleder, R. Chip-Based Analysis of Exosomal MRNA Mediating Drug Resistance in Glioblastoma. *Nat. Commun.* **2015**, *6*, 6999. [CrossRef] [PubMed]
17. Jeong, S.; Park, J.; Pathania, D.; Castro, C.M.; Weissleder, R.; Lee, H. Integrated Magneto–Electrochemical Sensor for Exosome Analysis. *ACS Nano* **2016**, *10*, 1802–1809. [CrossRef] [PubMed]
18. Ben Aissa, A.; Araújo, B.; Julián, E.; Zanoni, M.V.B.; Pividori, M.I. Immunomagnetic Separation Improves the Detection of Mycobacteria by Paper-Based Lateral and Vertical Flow Immunochromatographic Assays. *Sensors* **2021**, *21*, 5992. [CrossRef]

19. Yan, L.; Dou, L.; Bu, T.; Huang, Q.; Wang, R.; Yang, Q.; Huang, L.; Wang, J.; Zhang, D. Highly Sensitive Furazolidone Monitoring in Milk by a Signal Amplified Lateral Flow Assay Based on Magnetite Nanoparticles Labeled Dual-Probe. *Food Chem.* **2018**, *261*, 131–138. [CrossRef] [PubMed]
20. Moyano, A.; Serrano-Pertierra, E.; Salvador, M.; Carlos Martínez-García, J.; Rivas, M.; Carmen Blanco-López, M. Diagnostics Magnetic Lateral Flow Immunoassays. *Diagnostics* **2020**, *10*, 288. [CrossRef] [PubMed]
21. Guo, M.T.; Rotem, A.; Heyman, J.A.; Weitz, D.A. Droplet Microfluidics for High-Throughput Biological Assays. *Lab Chip* **2012**, *12*, 2146–2155. [CrossRef] [PubMed]
22. Le, M.C.N.; Fan, Z.H. Exosome Isolation Using Nanostructures and Microfluidic Devices. *Biomed. Mater.* **2021**, *16*, 022005. [CrossRef]
23. Wang, Y.; Li, Q.; Shi, H.; Tang, K.; Qiao, L.; Yu, G.; Ding, C.; Yu, S. Microfluidic Raman Biochip Detection of Exosomes: A Promising Tool for Prostate Cancer Diagnosis. *Lab Chip* **2020**, *20*, 4632–4637. [CrossRef]
24. Freiman, J.M.; Wang, J.; Easterbrook, P.J.; Horsburgh, C.R.; Marinucci, F.; White, L.F.; Kamkamidze, G.; Krajden, M.; Loarec, A.; Njouom, R.; et al. Deriving the Optimal Limit of Detection for an HCV Point-of-Care Test for Viraemic Infection: Analysis of a Global Dataset. *J. Hepatol.* **2019**, *71*, 62–70. [CrossRef] [PubMed]
25. Mitchell, M.I.; Ben-Dov, I.Z.; Liu, C.; Ye, K.; Chow, K.; Kramer, Y.; Gangadharan, A.; Park, S.; Fitzgerald, S.; Ramnauth, A.; et al. Extracellular Vesicle Capture by AnTibody of CHoice and Enzymatic Release (EV-CATCHER): A Customizable Purification Assay Designed for Small-RNA Biomarker Identification and Evaluation of Circulating Small-EVs. *J. Extracell. Vesicles* **2021**, *10*, e12110. [CrossRef]
26. Filipović, L.; Spasojević, M.; Prodanović, R.; Korać, A.; Matijaševic, S.; Brajušković, G.; de Marco, A.; Popović, M. Affinity-Based Isolation of Extracellular Vesicles by Means of Single-Domain Antibodies Bound to Macroporous Methacrylate-Based Copolymer. *New Biotechnol.* **2022**, *69*, 36–48. [CrossRef] [PubMed]
27. Jin, B.; Odongo, S.; Radwanska, M.; Magez, S. NANOBODIES®: A Review of Diagnostic and Therapeutic Applications. *Int. J. Mol. Sci.* **2023**, *24*, 5994. [CrossRef]
28. van Meer, B.J.; de Vries, H.; Firth, K.S.A.; van Weerd, J.; Tertoolen, L.G.J.; Karperien, H.B.J.; Jonkheijm, P.; Denning, C.; IJzerman, A.P.; Mummery, C.L. Small Molecule Absorption by PDMS in the Context of Drug Response Bioassays. *Biochem. Biophys. Res. Commun.* **2017**, *482*, 323–328. [CrossRef]
29. Kemas, A.M.; Zandi Shafagh, R.; Taebnia, N.; Michel, M.; Preiss, L.; Hofmann, U.; Lauschke, V.M. Compound Absorption in Polymer Devices Impairs the Translatability of Preclinical Safety Assessments. *Adv. Healthc. Mater.* **2023**, *13*, e2303561. [CrossRef]
30. Attia, U.M.; Marson, S.; Alcock, J.R. Micro-Injection Moulding of Polymer Microfluidic Devices. *Microfluid. Nanofluid.* **2009**, *7*, 1–28. [CrossRef]
31. Bajo-Santos, C.; Priedols, M.; Kaukis, P.; Paidere, G.; Gerulis-Bergmanis, R.; Mozolevskis, G.; Abols, A.; Rimsa, R. Extracellular Vesicles Isolation from Large Volume Samples Using a Polydimethylsiloxane-Free Microfluidic Device. *Int. J. Mol. Sci.* **2023**, *24*, 7971. [CrossRef] [PubMed]
32. Nunes, P.S.; Ohlsson, P.D.; Ordeig, O.; Kutter, J.P. Cyclic Olefin Polymers: Emerging Materials for Lab-on-a-Chip Applications. *Microfluid. Nanofluidics* **2010**, *9*, 145–161. [CrossRef]
33. Agha, A.; Waheed, W.; Alamoodi, N.; Mathew, B.; Alnaimat, F.; Abu-Nada, E.; Abderrahmane, A.; Alazzam, A. A Review of Cyclic Olefin Copolymer Applications in Microfluidics and Microdevices. *Macromol. Mater. Eng.* **2022**, *307*, 2200053. [CrossRef]
34. Guo, W.; Vilaplana, L.; Hansson, J.; Marco, M.-P.; Van Der Wijngaart, W. Immunoassays on Thiol-Ene Synthetic Paper Generate a Superior Fluorescence Signal. *Biosens. Bioelectron.* **2020**, *163*, 112279. [CrossRef]
35. Gustafsson, L.; Tasiopoulos, C.P.; Jansson, R.; Kvick, M.; Duursma, T.; Gasser, T.C.; van der Wijngaart, W.; Hedhammar, M. Recombinant Spider Silk Forms Tough and Elastic Nanomembranes That Are Protein-Permeable and Support Cell Attachment and Growth. *Adv. Funct. Mater.* **2020**, *30*, 2002982. [CrossRef]
36. Errando-Herranz, C.; Saharil, F.; Mola Romero, A.; Sandström, N.; Zandi Shafagh, R.; van der Wijngaart, W.; Haraldsson, T.; Gylfason, K.B.; Sun, Y.S.; Landry, J.P.; et al. Integration of Microfluidics with Grating Coupled Silicon Photonic Sensors by One-Step Combined Photopatterning and Molding of OSTE. *Opt. Express* **2013**, *21*, 21293–21298. [CrossRef] [PubMed]
37. Rimsa, R.; Galvanovskis, A.; Plume, J.; Rumnieks, F.; Grindulis, K.; Paidere, G.; Erentraute, S.; Mozolevskis, G.; Abols, A. Lung on a Chip Development from Off-Stoichiometry Thiol–Ene Polymer. *Micromachines* **2021**, *12*, 546. [CrossRef] [PubMed]
38. Priedols, M.; Paidere, G.; Santos, C.B.; Miscenko, A.; Bergmanis, R.G.; Spule, A.; Bekere, B.; Mozolevskis, G.; Abols, A.; Rimsa, R. Bifurcated Asymmetric Field Flow Fractionation of Nanoparticles in PDMS-Free Microfluidic Devices for Applications in Label-Free Extracellular Vesicle Separation. *Polymers* **2023**, *15*, 789. [CrossRef]
39. Sackmann, E.K.; Fulton, A.L.; Beebe, D.J. The Present and Future Role of Microfluidics in Biomedical Research. *Nature* **2014**, *507*, 181–189. [CrossRef]
40. Hashmi, A.; Xu, J. On the quantification of mixing in microfluidics. *J. Lab. Autom.* **2014**, *19*, 488–491. [CrossRef]
41. Cosentino, A.; Madadi, H.; Vergara, P.; Vecchione, R.; Causa, F.; Netti, P.A. An Efficient Planar Accordion-Shaped Micromixer: From Biochemical Mixing to Biological Application. *Sci. Rep.* **2015**, *5*, 17876. [CrossRef] [PubMed]
42. Khanarian, G. Optical Properties of Cyclic Olefin Copolymers. *Opt. Eng.* **2001**, *40*, 1024–1029. [CrossRef]
43. Sandström, N.; Shafagh, R.Z.; Vastesson, A.; Carlborg, C.F.; Van Der Wijngaart, W.; Haraldsson, T. Reaction Injection Molding and Direct Covalent Bonding of OSTE+ Polymer Microfluidic Devices. *J. Micromech. Microeng.* **2015**, *25*, 075002. [CrossRef]

44. Cipa, J.; Endzelins, E.; Rimsa, R.; Galvanovskis, A.; Abols, A.; Line, A.; Mozolevskis, G. OSTE Device for Magnetic Particle Capture. In Proceedings of the MicroTAS 2022—26th International Conference on Miniaturized Systems for Chemistry and Life Sciences, Hangzhou, China, 23–27 October 2022; pp. 919–920.
45. Petkovic, K.; Metcalfe, G.; Chen, H.; Gao, Y.; Best, M.; Lester, D.; Zhu, Y. Rapid Detection of Hendra Virus Antibodies: An Integrated Device with Nanoparticle Assay and Chaotic Micromixing. *Lab Chip* **2017**, *17*, 169–177. [CrossRef] [PubMed]
46. Life Technologies. *Exosome-Human CD63 Isolation/Detection (from Cell Culture Media) Protocol for Use in Flow Cytometry Product Description*; Life Technologies: Oslo, Norway, 2013.
47. Life Technologies. *Exosome-Human CD9 Isolation (from Cell Culture) Pre-Enriched Exosome Sample Input*; Life Technologies: Carlsbad, CA, USA, 2014.

The University of Latvia Press
Aspazijas bulv. 5–132, Riga, LV-1050
www.apgads.lu.lv
Online bookstore: gramatas.lu.lv

Printed: SIA "Drukātava"